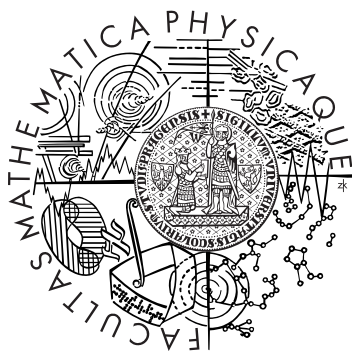Charles University in Prague

Faculty of Mathematics and Physics

Doctoral Thesis

Hynek Němec

**Time-resolved terahertz spectroscopy applied
to the investigation of magnetic materials
and photonic structures**

Supervisors: Petr Kužel, and Lionel Duvillaret

Prague, 2006

Acknowledgment

Contents

Summary (English, French, Czech)

Time-resolved terahertz spectroscopy applied to investigation of magnetic materials and photonic structures

Summary: Two distinct branches of optics are combined in this work: Time-domain terahertz spectroscopy, and photonic structures. The work at first provides a survey of tools utilized for exploration of the terahertz region, and it enriches them by a method for simultaneous determination of dielectric and magnetic response of materials and metamaterials. Photonic structures operating in the terahertz range form the subject of the rest of this thesis. A periodically modulated dielectric waveguide is studied theoretically using a modal method: The band structure of guided and leaky modes is calculated and resonant modes are described. One-dimensional photonic crystals with a defect are then investigated in detail. Formation of defect modes is analyzed theoretically in a photonic crystal with a twinning defect. The analysis makes it possible to formulate requirements on a design of a structure with defect modes tunable by external parameters. Following these guidelines, we have successfully designed, fabricated and characterized photonic crystals with thermally tunable defect modes with relative tunability reaching 60 %.

Keywords: photonic crystals, dielectric properties, magnetic properties, time-domain terahertz spectroscopy, dielectric diffraction gratings, tunable filters

---

Spectroscopie térahertz dans le domaine temporel appliquée aux matériaux magnétiques et aux structures photoniques

Résumé : Deux domaines différents de l'optique sont associés dans ce travail : spectroscopie térahertz dans le domaine temporel, et structures photoniques. Tout d'abord, un état de l'art des méthodes et techniques utilisées pour l'exploration de la région térahertz est dressé, et une nouvelle méthode de détermination simultanée des réponses diélectrique et magnétique des matériaux et métamatériaux est ensuite présentée. Les structures photoniques opérant dans la région térahertz sont traitées dans la seconde partie de cette thèse. Les guides d'ondes présentant une modulation périodique sont étudiés théoriquement par la méthode modale : la structure de bandes des modes guidés et des modes à perte est calculée et les modes résonants sont décrits. Les cristaux photoniques avec un défaut sont ensuite examinés en détail. La formation des modes de défaut est analysée théoriquement dans les cristaux photoniques avec un défaut gémellaire. Cette analyse permet de définir les paramètres de la structure qui autorisent une accordabilité des modes de défaut au moyen de paramètres physiques extérieurs. À partir de ces outils de conception, nous avons proposé, fabriqué et caractérisé des cristaux photoniques avec des modes de défaut accordable par la température et obtenu une accordabilité relative de 60 %.

Mots clés: cristaux photoniques, propriétés diélectriques, propriétés magnétiques, spectroscopie térahertz dans le domaine temporel, réseaux de diffraction diélectriques, filtres accordables

Terahertzová spektroskopie v časovém oboru aplikovaná na studium magnetických materiálů a fotonických struktur

Shrnutí: V této práci jsou kombinovány dvě různé oblasti optiky: terahertzová spektroskopie v časovém oboru, a fotonické struktury. Tato práce nejprve podává přehled technik používaných pro zkoumání terahertzového oboru, a obohacuje je o metodu pro současné určování dielektrické a magnetické odezvy látek a metamateriálů. Náplní zbývajících částí jsou fotonické struktury pro terahertzovou oblast. Periodicky modulovaný dielektrický vlnovod je studován teoreticky modální metodou: je vypočtena pásová struktura vedených a tlumených módů a jsou popsány resonantní módy. Poté se detailně zabýváme jednorozměrnými fotonickými krystaly s defektem. Vznik defektních módů je teoreticky analyzován pro případ jednorozměrného fotonického krystalu s dvojčatěním. Tato analýza umožňuje zformulovat požadavky na návrh struktury s defektními módy laditelnými vnějšími parametry. Na základě těchto poznatků jsme úspěšně navrhli, vyrobili a charakterizovali fotonické krystaly s teplotně laditelnými defektními módy, jejichž laditelnost dosahuje 60 %.

Klíčová slova: fotonické krystaly, dielektrické vlastnosti, magnetické vlastnosti, terahertzová spektroskopie v časovém oboru, dielektrické difrakční mřížky, laditelné filtry

Résumé étendu (français)

La gamme spectrale térahertz est devenu facilement accessible et largement explorée depuis les années 80 grâce au développement de la spectroscopie térahertz dans le domaine temporel. Cette technique est basée sur la génération et détection cohérente d'impulsions térahertz large bande : les deux processus d'émission et de réception sont commandés et synchronisés par des impulsions lasers ultrabrèves. La spectroscopie térahertz dans le domaine temporel est actuellement utilisée dans des applications diverses, comme la caractérisation de la réponse diélectrique complexe de matériaux, l'étude de la dynamique de phénomènes transitoire en matière condensée, et l'imagerie dans les domaines de la médecine ou de la sécurité.

Au cours de cette même période, les scientifiques se sont aperçus des propriétés spectaculaires des cristaux photoniques. Les cristaux photoniques possèdent une périodicité à l'échelle macroscopique et, si les paramètres qui les définissent sont bien choisis, ils peuvent présenter une bande interdite (à transmission nulle) dans un intervalle de fréquences. L'une de leurs propriétés remarquables est la possibilité de localiser fortement la lumière dans une partie minuscule du cristal (au voisinage d'un défaut de structure). Les dispositifs tirant parti des propriétés des cristaux photoniques trouvent des applications en optoélectronique tout en offrant la possibilité de miniaturisation des composants ; ils peuvent également faciliter l'intégration monolithique en optique et microélectronique. La plupart de l'effort dans la recherche sur les cristaux photoniques est orienté sur la conception et la fabrication de structures opérationnelles dans les domaines optique et micro-onde, lesquels présentent un intérêt particulier en vue d'applications dans les télécommunications. L'évolution continue vers des appareils fonctionnant à des fréquences de plus en plus élevées exige aussi l'exploration du domaine térahertz.

Une classe spécifique de structures photoniques est constituée par les métamatériaux à indice de réfraction négatif. Ces métamatériaux se révèlent importants pour la construction de lentilles parfaites par exemple : il est prédit que de telles lentilles peuvent être utilisées pour l'imagerie avec une résolution spatiale supérieure à celle imposée par les lois de la diffraction.

Les deux domaines de recherche introduits—la spectroscopie térahertz et les structures photoniques—sont exploités et développés dans ce travail, dont l'un des objectifs principaux est l'étude et la construction d'un cristal photonique fonctionnel dans la gamme térahertz et accordable par un paramètre physique externe. Les résultats les plus importants de cette thèse sont décrits dans les paragraphes suivants.

1. La spectroscopie térahertz dans le domaine temporel est couramment utilisée pour effectuer la mesure de la permittivité complexe de matériaux en phase solide et liquide. Cependant, une réponse magnétique peut être simultanément trouvée dans quelques matériaux, comme dans les métamatériaux à indice de réfraction négatif où l'existence d'une perméabilité négative est essentielle. La nécessité de disposer

de méthodes spectroscopiques pour la détermination simultanée de la permittivité et de la perméabilité est donc fondamentale pour caractériser de tels matériaux. Dans ce manuscrit nous proposons de telles méthodes pour une détermination simultanée des réponses diélectrique et magnétique d'échantillons optiquement épais par spectroscopie térahertz. Afin de déterminer simultanément les permittivité et perméabilité complexes, on a besoin de mesurer deux quantités spectroscopiques complexes indépendantes. Nous les obtenons par transformée de Fourier appliquée après un fenêtrage temporel aux signaux mesurés dans le domaine temporel pour des arrangements en transmission et/ou en réflexion. Suivant le choix des spectres de départ, nous avons décrit et analysé en détail trois approches et nous avons effectué leur validation expérimentale. L'application de ces méthodes à la caractérisation des métamatériaux est alors démontrée par simulations numériques.

2. Les guides d'ondes diélectriques périodiquement modulés (réseaux de diffraction) présentent un intérêt particulier en raison de la possibilité d'une optimisation de l'accord de phase pour la génération de second harmonique. Cependant, la structure de bandes des modes guidés des réseaux de diffraction n'était généralement pas étudiée d'une façon rigoureuse. C'est la raison pour laquelle nous avons effectué une étude théorique de ce type de guide d'ondes au moyen d'une méthode rigoureuse de couplage des modes. Ceci nous a permis de calculer la structure de bandes des modes guidés et d'évaluer leurs pertes à cause du rayonnement vers l'extérieur. Par ailleurs, nous avons identifié des modes résonants dont la nature est proche des modes de l'interféromètre de Fabry–Pérot. De plus, nous présentons une modélisation numérique des spectres de transmission, ce qui nous permet de comparer la théorie et l'expérience.

3. L'exploration systématique des structures photoniques est en grande partie dépendante de l'existence et du développement des méthodes numériques capables de prédire leurs propriétés, notamment leurs spectres de transmission et de réflexion et leurs structure de bandes. Une partie de ce manuscrit est dévolue à une description détaillée de la méthode des matrices de transfert applicable à des structures périodiques en une, deux ou trois dimensions. Un code de programme numérique à été écrit dans le cadre de ce travail. Il a été appliqué à la simulation des spectres d'un métamatériau décrit dans le paragraphe 1. Ce programme nous a également servi à la modélisation des spectres de transmission et réflexion de réseaux de diffraction décrits dans le paragraphe 2.

4. Des cristaux photoniques commandables trouvent leurs applications en optoélectronique comme filtres, guides d'ondes et démultiplexeurs. Dans ce travail, nous nous concentrons sur l'accordabilité des modes de défaut des cristaux photoniques par un paramètre externe : un tel cristal pourrait servir comme filtre spectral accordable. La

compréhension du rapport entre les paramètres structuraux d'un cristal photonique et ses propriétés optiques est cruciale pour le design des structures optimisées.

Nous avons étudié en détail les propriétés du cristal photonique unidimensionnel contenant un défaut de périodicité. Nous avons analysé le rapport entre les fréquences des niveaux de défauts et les paramètres du cristal photonique, notamment en vue d'une optimisation de son accordabilité. En particulier, nous avons discuté l'influence de l'indice de réfraction, de l'impédance et de l'épaisseur de la couche du défaut sur la fréquence de ce mode de défaut. Nous avons trouvé un ensemble de critères que les matériaux doivent satisfaire pour obtenir un cristal photonique opérationnel comme filtre spectral accordable. Nous nous sommes focalisés sur les ferroélectriques naissants ($SrTiO_3$, $KTaO_3$). Ces composés présentent un mode mou ferroélectrique alors qu'ils restent dans la phase paraélectrique jusqu'aux très basses températures. L'amollissement du mode mou permet ensuite de commander la permittivité dans le domaine térahertz par la variation de la température ou du champ électrique appliqué, ce qui est essentiel pour achever l'accordabilité du mode de défaut. En revanche, les pertes diélectriques restent raisonnablement faibles, ce qui est important en vue d'une faible atténuation en bande passante. Nous avons proposé, fabriqué et testé expérimentalement un cristal photonique compact dans lequel l'accordabilité du mode de défaut a atteint 60 %.

Preface

The terahertz (THz) region has become easily accessible and widely explored since the eighties thanks to the development of lasers providing ultrashort pulses and subsequent development of time-domain THz spectroscopy (TDTS) [1]. TDTS is all the more important method as it is based on coherent generation and detection of electromagnetic THz pulses, where both processes are synchronously controlled by ultrashort laser pulses. TDTS is presently used in diverse applications, including measurement of complex dielectric response, investigation of transient far-infrared dynamics in the condensed-matter research, or imaging in medicine and security.

Just about the same period, the spectacular optical properties of photonic crystals (PCs) have been recognized [2]. For example, the light can be strongly localized in a small part of a PC. PC-based devices can thus provide basic functions using smaller place than their classical counterparts, and they can also facilitate monolithic integration of optics and microelectronics. Most of the actual work in PCs is focused on design and fabrication of PCs operating in optical or microwave regions, which are of particular interest due to existing or rapidly developing communication applications. However, the unceasing progress towards faster devices demands the exploration of the THz region as well.

THz region is also important for verification of numerical models of PCs. The typical size of components of THz PCs lies in the hundred-microns range, allowing to employ common methods for their fabrication. The submission of PCs to the scaling laws makes it possible to transfer the results obtained in the THz region into the optical region where fabrication of PCs still remains a challenge due to sub-micron dimensions of the components. It should be noted that the phase sensitivity of TDTS, which can be used for characterization of PCs, brings a valuable additional information about properties of PCs as compared to optical measurements.

Development of PCs for the THz region is related to availability of materials with suitable far-infrared optical properties. As the dielectric response in the THz region is mainly related to a strong interaction of THz radiation with free carriers and to soft lattice vibrations, a detailed understanding of underlaying physical processes is essential for selection of appropriate materials. In turn, not only the knowledge of optics, but also the material research plays an important role for designing PCs with desired properties.

For all the interest the PCs attract, development of more complicated metamaterials has become a hot topic during the very last years. Considerable effort concentrates on design of an isotropic metamaterial with negative refractive index, or equivalently, with simultaneously negative permittivity and permeability [3]. Up to now, a natural material with such properties has not been found. However, the desired magnetic and dielectric response can be achieved by proper arrangement of metallic sub-wavelength size components on a dielectric substrate [4]. At the same time, the construction of such a metamaterial calls for development of methods capable of independent determination of dielectric and magnetic response: Appropriate methods are currently available solely at low frequencies

up to the microwave region.

The thesis is focused on investigation of PCs operating in the THz region. It is divided into two major parts. The first part is devoted to the survey of the THz region, and in particular, to the description and applications of TDTS. The first chapter brings a general overview of methods used for generation and detection of THz radiation. In Chap. 2, we provide a brief summary of methods employed in TDTS and their applications. The last chapter of this first part (Chap. 3) presents an original work devoted to independent determination of dielectric and magnetic response in the THz region.

The second part of the thesis treats some particular aspects of the enormous field of photonic structures. The problematic of PCs and photonic structures is introduced in Chap. 4. An important part of the research in PCs consists in numerical simulation of their properties. The methods used in this work are thus discussed in Chap. 5. The remaining two chapters present original results obtained in the framework of this thesis. Both chapters deal with photonic structures operating in the THz region. In Chap. 6, we investigate theoretically guided modes of a dielectric periodically modulated waveguide. The last chapter (Chap. 7) is devoted to the design, construction and characterization of PCs with tunable defect modes.

Acronyms

1D, 2D, 3D	One-, two- and three-dimensional
BWO	Backward wave oscillator
FP	Fabry–Pérot
LHM	Left-handed medium/media
OPTP	Optical pump–terahertz probe
PC	Photonic crystal
RHM	Right-handed medium/media
TDTS	Time-domain terahertz spectroscopy
TDTRS	Time-domain terahertz reflection spectroscopy
TDTTS	Time-domain terahertz transmission spectroscopy
TMM	Transfer matrix method
THz	Terahertz

Part I

Time-domain terahertz spectroscopy

Chapter 1

Terahertz radiation

1.1 Introduction

Terahertz (THz) region—also often called as THz gap—is usually associated with a range of frequencies between $\sim 100\,\text{GHz}$ and $\sim 3\,\text{THz}$ (Fig. 1.1). In fact, the access to this region has been until recently particularly difficult. It is not possible to reach this region by increasing the frequency of electronic synthesizers [5, 6], and conversely, it is tricky to attain this region using optical sources of radiation as their brightness rapidly decreases towards longer wavelengths, according to the Planck's law.

Despite these problems, investigation of the THz region has begun already at the end of the 19$^{\text{th}}$ century, soon after the pioneering works of Heinrich Rudolf Hertz on electromagnetic waves (Ref. [7] provides an excellent historical review). Nevertheless, the boom of exploration of the THz region started only some 20 years ago thanks to the invention of time-domain THz spectroscopy (TDTS) [1, 8, 9] which allowed to dramatically increase the sensitivity and the rapidity of measurements.

TDTS is a phase-sensitive method. This is a very important attribute for the material research as it allows determination of *complex* optical constants without model assumptions and without application of Kramers-Kronig's relations [10]. The phase-sensitivity also seems very helpful for development of THz tomographic imaging techniques [11, 12].
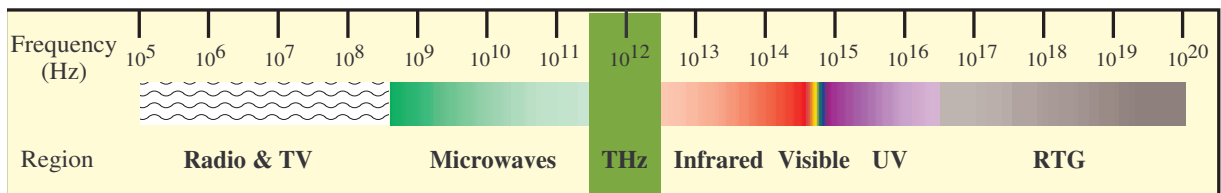
Figure 1.1: Spectrum of electromagnetic radiation. The THz gap is marked by a green rectangle.

Finally, the generation and detection in TDTS is synchronized by ultrashort laser pulses, making TDTS a unique technique for transient dynamics investigations [13].

The kernel of the setup for TDTS consists of a laser delivering a train of ultrashort pulses (Fig. 1.2). One part of the laser beam is used to generate the THz radiation in an emitter: The optical pulses are rectified via suitable nonlinear interaction in the emitter. The generated THz pulses are typically nearly single-cycle pulses of electromagnetic field, and consequently, they contain a broad spectrum of frequencies. The THz pulses then propagate through the investigated sample to a detector. The detection is accomplished by a sampling technique triggered by gating pulses (split from the original laser beam), i.e. the resulting signal depends on the instantaneous THz field at the moment the gating pulse arrives. By changing the time of the arrival of the gating pulse, the field of the entire THz pulse (THz waveform) can be scanned. The basic means of generation and detection of THz pulses are described in Secs. 1.2 and 1.3. The setup can be simply extended for transient measurements (dashed line in Fig. 1.2). The transient dynamics in the sample is initiated by another laser beam (the pump beam) split from the original one. The response of the photoexcited sample is subsequently probed by a delayed THz pulse in a synchronous manner, making the measurements nearly jitter-free.

The spectral range covered by TDTS depends on the properties of the emitter and the sensor as well as on the length of the laser pulses. Traditional setups cover the THz gap from $\sim 100\,\mathrm{GHz}$ to $\sim 3\,\mathrm{THz}$ (Fig. 1.1) Appropriate spectrometers make typically use of lasers delivering pulses with duration of about $100\,\mathrm{fs}$ in conjunction with numerous techniques for generation and detection of THz pulses, which will be discussed in detail in following sections. Nevertheless, the key idea of TDTS has been reused to cover other spectral regions as well. In particular, coherent microwave transient spectroscopy [14] was
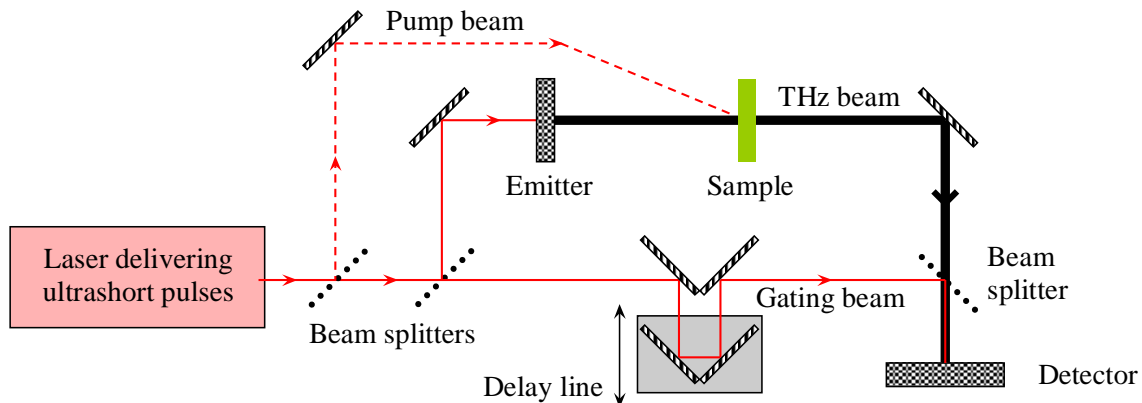
Figure 1.2: Block scheme of the setup for TDTS. The optical beam is marked by red color while the THz beam is indicated by a thick black line. The pump-branch (dashed) serves only for transient dynamics investigations.

developed in order to investigate the 10–125 GHz band. It uses coplanar-transmission-lines based antennae in conjunction with laser pulses of 2.5 ps duration. Conversely, frequencies as high as 70 THz were accessed utilizing 12 fs laser pulses in conjunction with optical rectification generation and electro-optic detection of THz pulses in thin ZnTe crystals [15]. However, it should be emphasized that both these regions can be much more efficiently accessed using other techniques like vector network analyzers or infrared Fourier-transform spectroscopy, respectively [10]. Indeed, the synchronicity of TDTS brings a valuable information about transient dynamics even in these parts of spectral regions [16].

From the point of view of high spectral resolution, TDTS it not the best method. The spectral resolution Δf is related to the temporal scan length T via the uncertainty relation

$$\Delta f \cdot T \gtrsim 1, \tag{1.1}$$

thus long temporal scans are required for high spectral resolution. In practice, resolution better than units of GHz can be hardly achieved due to problems with precise alignment of the optical system. Nevertheless, such a resolution is fairly sufficient for most of the applications in condensed-matter physics.

There are two basic processes serving for conversion of ultrashort laser pulses into THz pulses and for their detection: Photoconduction in ultrafast semiconductors (described in Sec. 1.2), and optical non-linear phenomena (discussed in Sec. 1.3). TDTS is not the only tool which allows an efficient exploration of the THz region, as it was already anticipated in the very beginning of this chapter. Therefore Sec. 1.4 is thus devoted to a short description of some of the other methods.

1.2   Generation and detection using photoconduction

Photoconductive antennae (also called photoconductive switches) were introduced for generation and detection of THz pulses by Auston et al. [1]. In this work, an incoming laser pulse with a photon energy above the band gap generates free carriers in the conduction band of a semiconductor. These free carriers are immediately accelerated by an applied electric field, and finally they are trapped or they recombine. These processes result in a rapid variation of the current density, giving rise to a pulse of THz radiation emitted into the substrate. Similar antenna (a sensor) is used on the opposite side of the substrate for detecting the THz pulse. A delayed gating pulse is used to generate free carriers. The free carriers are accelerated by the electric field of the THz pulse, creating a charge transfer. The electric current is measured by an amperemeter connected to electrodes deposited on the sensor. By changing the gating pulse delay, the shape of the electric field of the THz pulse can be scanned.

The size of the active area of the Auston's emitter [1] was small compared to the wavelengths of the emitted THz radiation. Such a source thus behaves like a point dipole, which is characterized by poor directionality. Consequently, the emitter and the sensor

must be as close as possible to each other (in fact, they were separated just by a common substrate in [1]). However, for majority of applications it is desirable to deal with THz pulses propagating in a free space [17]. For this purpose van Exter et al. proposed to attach sapphire or silicon lenses to antennae in order to collimate the THz beam [18, 19]. The directionality can be also improved by using so called large-aperture emitters [20, 21], where the distance between electrodes is larger or comparable to the wavelength of the THz radiation. At the same time, also the emitted power can be increased: The area of large-aperture emitters can be scaled up to accept the entire optical radiation without the problems of damage and saturation which arise for higher optical fluences [21–24].

Concerning the material for the emitter, semiconductors with ultrashort carrier lifetime and high mobility are preferable. In fact, the shorter is the carrier lifetime and the higher is the mobility, the stronger are the current-density changes, and also the intensity of radiated THz pulses becomes stronger. In addition, short carrier lifetime enhances the intensity of short-wavelength spectrum of the emitted radiation. The material should also exhibit large dark resistivity in order to limit the heating of the emitter. These requirements are met in semiconductors like low-temperature-grown GaAs, Be-doped low-temperature-grown GaAs or Cr-doped GaAs [25–27]. All these materials are commonly employed for construction of biased photoconductive antennae.

Up to now, we considered that the photo-generated carriers are accelerated in an external bias field. However, also the surface depletion field in semiconductors can serve for carrier acceleration, avoiding the necessity of using an external voltage source [28, 29]. The surface depletion field is normal to the surface of the emitter, so the emitted THz power vanishes for the normal incidence of the laser beam. Arrangements based on oblique incidence of the optical excitation beam thus must be employed. Unbiased photoconductive emitters are usually based on InAs crystals [30, 31] or semi-insulating GaAs crystals [29]. They are also often placed into a magnetic field in order to enhance the emitted THz power. It has been found that there are several mechanisms responsible for the enhancement depending on the excitation intensity [32, 33].

Different factors like finite bandwidth and spectral dependence of the sensitivity of the detector limit its detection capabilities, resulting in reshaping of the signal [25, 34]. Besides the dispersion of dielectric properties of the photoconductive material, the detector response is in most cases determined by the gating pulse width and free carrier lifetime. While the response is nearly flat for frequencies lower than gating pulse bandwidth, the higher frequencies are completely suppressed. Longer free-carrier lifetimes favor the lower frequencies too, but the higher frequencies components still remain measurable [35, 36]. In practice, short carrier lifetimes are required to balance the response to low- and high-frequency components. Sensors made of low-temperature-grown GaAs [37] or radiation-damaged silicon-on-sapphire (RD-SOS) [1] are the most frequently employed. However, the low-temperature-grown GaAs is usually preferred due to its higher carrier mobility, which leads to a stronger signal. Properties of other photoconductive materials applicable in TDTS are resumed e.g. in [38].

It should be noticed that the geometrical structure of the photoconductive antenna (mainly the structure of its metallic electrodes) modifies the distribution of the electromagnetic field in its vicinity. Nevertheless, for antennae much smaller than the shortest wavelength, the field distribution remains practically homogenous and the corresponding response function is thus flat. The detector sensitivity can be substantially increased by attachment of sapphire or silicon lenses which focus the THz power to the active area [18,19]. On the other hand, this setup limits longer wavelengths [34].

1.3   Generation and detection using nonlinear crystals

THz pulses are often generated and detected by means of non-linear phenomena. The second order non-linearity of dielectric function is the most important one due to its strength. The THz emission then originates from optical rectification effect [39]: As ultrashort optical pulses are used for photo-excitation, a broad spectrum is involved in the non-linear interaction, causing the generated difference-frequencies spectrum to overlap the THz region.

There are several groups of non-linear materials suitable for efficient THz radiation generation:

- The optical transition can be non-resonant, i.e. only bonded carriers are anharmonically displaced. The corresponding non-linear susceptibility is thus weak, and efficient THz radiation generation can occur only if the non-linear interaction takes place over a long distance. The maximum interaction length is equal to the coherence length defined as [40]

$$L_{\mathrm{coh}} = \frac{\lambda}{2} \cdot \frac{1}{|N_{\mathrm{g}} - n_{\mathrm{THz}}(\lambda)|}, \tag{1.2}$$

  where N_{g} is the group refractive index of the optical pulse and n_{THz} is the refractive index of the THz component with wavelength λ. Materials with N_{g} close to $n_{\mathrm{THz}}(\lambda)$ are thus required.

  The most popular THz emitter belonging to this group is a ZnTe crystal excited by 800 nm optical pulses. It exhibits coherence length greater than 2 mm for frequencies below 2 THz [40]. THz radiation can be generated via non-resonant excitation also in GaSe and LiNbO$_3$ crystals [41, 42].

- A different situation occurs when the photon energy is sufficient to cause resonant optical transitions. The excitation beam is absorbed within typically few microns, and the notion of coherence length L_{coh} becomes meaningless. However, the appropriate non-linear coefficient may be sufficiently large (owing to the resonant character of the transition) to produce intense THz pulses. This is the case of e.g. GaAs or InP crystals irradiated by 800 nm optical pulses [43–45].

- There are also promising organic crystals like dimethyl amino 4-N-methylstilbazolium (DAST) or 2-methyl-4-nitroaniline (MNA) [46, 47]. These crystals are composed of molecules with very high electronic polarizabilities, implying high nonlinear coefficients as compared to anorganic crystals. Therefore intense THz radiation can be generated even if the coherence length is short.

- Another mechanism of THz radiation generation in non-linear media involves production of a polarization shock-wave, referred as the Čerenkov-like radiation in the literature. This phenomenon can be found e.g. in LiTaO$_3$ crystals, where $n_{\mathrm{THz}}(f) > N_{\mathrm{g}}$, i.e., the phase velocity of the THz radiation is smaller than the group velocity of the incident optical pulse [48].

The detection process—called electro-optic sampling—is based on the electro-optic Pockels' effect [49]. The birefringence is induced by the electric field of the THz pulse, and it is instantaneously probed by the gating pulse. Majority of detecting systems employ the electro-optic sensors in transmission geometry. Consequently, the gating beam should not cause resonant transitions in the sensor in order to avoid its strong attenuation. Crystals including ZnTe, GaP, DAST, LiTaO$_3$ and LiNbO$_3$ crystals are often used for electro-optic detection [50–53].

There are two basic configurations of the detecting system. In the first one, the THz-field induced birefringence is deduced from the ellipticity of a circularly polarized gating beam, which can be simply measured as a difference signal from a pair of balanced photodiodes (Fig. 1.3a). Advantages of this configuration are a linear relation between the measured signal and the instantaneous THz field, and an excellent stability with respect
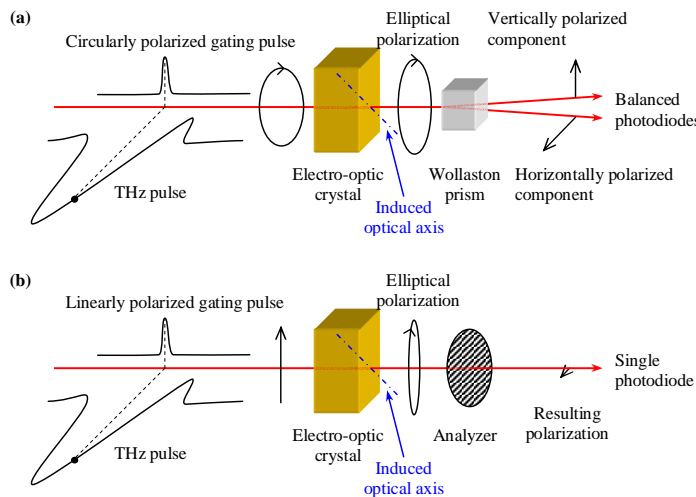
Figure 1.3: Basic schemes of electro-optic sampling systems. (a) Configuration employing a pair of balanced photodiodes. (b) Configuration operating near the zero-transmission point.

to fluctuations of the gating beam polarization. In the other configuration the ellipticity is measured near the zero-transmission point (Fig. 1.3b) [54]. Consequently, the relation between the detected signal and instantaneous THz field becomes non-linear. Nevertheless, this scheme is important when a single photodetector is required, like in certain imaging applications [55] or in single-shot measurements [56].

Finally, let's briefly mention other non-linear phenomena used for generation and detection of THz pulses respectively. Four-wave mixing involving a surface depletion field was shown to generate THz radiation in $\langle 100 \rangle$ and $\langle 111 \rangle$ oriented InP crystal [57]. Analogically to electro-optic sampling, magneto-optic sampling can be used for detection of the magnetic-field of THz radiation. Such a technique is based on Faraday rotation effect, induced by transient magnetic THz field. Sensors made of Bi-substituted yttrium-iron-garnet film and SF-59 amorphous glasses were constructed [58, 59].

Very recently, optical rectification at metal surfaces has been demonstrated to generate THz radiation [60–62]. Despite the low cost of such emitters, the emitted intensity is comparable with conventional emitters.

1.4 Other means of generation and detection

The infrared Fourier transform spectroscopy is nowadays a classical tool described in many articles and reviews (e.g. Chapter 5 in [10]). Though it is primarily applied to investigations of infrared region, it allows measurements down to the THz range (0.5 THz in the Bruker IFS113v spectrometer, for example). The accuracy drops down towards lower frequencies owing to the rapid decrease of the brightness of the radiation source. Deeper comparison of infrared Fourier-transform spectroscopy and TDTS in the THz gap can be found e.g. in [63, 64].

Another tool developed already in the 1960ˢ makes use of backward-wave oscillators (BWOs). The BWOs deliver intense, coherent monochromatic THz radiation. However, due to the electronic nature of the device, the highest frequency is limited to about 1.2 THz. As this method was employed for some of the measurements presented in this thesis, a separate paragraph is devoted to its description (page 26).

For about ten years a vector network analyzer operating up to 1 THz is commercially available [65, 66]. It involves frequency multiplication in Schottky harmonic generators as sources, and frequency downconversion in Schottky harmonic mixers as detectors. Either field-effect transistors or Gunn's diodes serve as primary oscillators. The stability of the outgoing THz radiation is controlled by the stability of these local oscillators. It was anticipated that the stability of this device can reach the Hz range in conjunction with high-quality cavities at very low temperatures [67].

Indeed, especially in the past decade there have been a great progress towards construction of a cheap, compact solid-state THz source, utilizable in desk applications [68, 69]. Presently, the most promising devices are photomixers and quantum cascade lasers.

The principle of the THz radiation generation via photomixing is extraordinarily simple. Two laser beams with close wavelengths are focused to a highly non-linear medium, typically to low-temperature-grown GaAs [70]. A coherent THz radiation then appears as a result of the difference frequency generation in that material. The relative monochromacity of the outgoing THz beam is degraded by a factor of about 100 with respect to the relative monochromacity of the pumping lasers, nevertheless it is still in the order of 10^{-6}. Also the tunability of this source can be very wide, as slight tuning of one of the pumping lasers causes a substantial tuning of the THz radiation. However, the problem is the low THz power, which further drops down above certain cut-off frequency [71]. Despite that, several interesting spectroscopic studies have been performed using this system [72–74]. In perspective, the whole THz source of such a type could be incorporated into a single laser diode [75].

Quantum cascade lasers are based on electrically-pumped semiconductor heterostructures. The charge carriers cascade through a series of quantum wells while emitting multiple photons. Population inversion is achieved through careful control of the lifetimes of the upper and lower states. Quantum cascade laser operating at 71 THz has been constructed in 1994 by Faist et al. [76]. Further development allowed to reach the classical THz range few years ago [77], providing highly monochromatic beams with powers in the mW range. However, the main drawback of existing quantum cascade lasers is the lack of tunability, making it cumbersome to perform spectroscopic studies: The source needs to be changed for each measured frequency [78]. It would be also desirable to increase the operating temperature, which still remains in the tens-Kelvin range.

The detectors commonly used in conjunction with the sources of THz radiation described in this section are conventional devices [10]. The best sensitivity is offered by bolometers operating at liquid-helium temperatures. However, the sensitivity is paid by the necessity of a cooling system and by slow response. In order to operate at room temperature, acousto-optical Golay cells or pyroelectric detectors are used. Anyway, all these detectors are capable of measurement of a THz power only, averaged over many periods of the THz electromagnetic field.

Coherent source submillimeter wave spectroscopy

This method is closely related to the existence of tunable monochromatic coherent sources of electromagnetic radiation—so called backward-wave oscillators (BWOs). BWOs essentially resemble to vacuum triodes (Fig. 1.4): an electron beam emitted from the cathode is accelerated by high electric field towards the anode. The electron beam collimated by an external magnetic field flies over a comb-like fine-structure electrode, intended to transfer the kinetic energy of the electrons to the electromagnetic field. Owing to the movement in this variable potential, the electrons are grouped periodically giving rise to an electromagnetic wave moving in an opposite direction. This radiation is coupled outwards through an oversized waveguide [10].
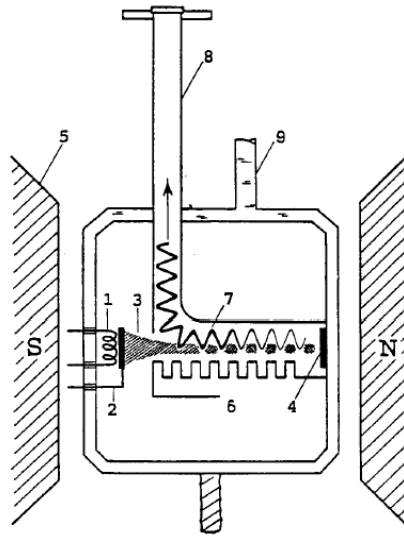
Figure 1.4: Schematic diagram of a BWO: 1 – heater, 2 – cathode, 3 – electron beam, 4 – anode (collector), 5 – permanent magnet, 6 – comb-like electrode, 7 – electromagnetic wave, 8 – waveguide, 9 – cooling water. (After Ref. [10].)

BWO spectroscopy is ideally suited for applications where good spectral resolution is required in a narrow spectral range. The monochromacity of BWO and frequency reproducibility under high-voltage tuning conditions can be maintained at the level of $\Delta f \approx 10^{-5} f$. However, the tunability of BWOs is somewhat limited ($< 30\%$), hence several BWO sources are needed to cover a wide spectral range (Fig. 1.5). Typical region accessible via BWO spreads between $\sim 30\,\mathrm{GHz}$ and $1.2\,\mathrm{THz}$, and the emitted power decreases towards shorter wavelengths. While the upper limit has remained fixed since the development of BWO due to conflicting requirements on its construction (small dimensions, high temperature, high vacuum, high electric field), the lower-frequency BWOs are being continuously replaced by cheaper sources like avalanche or Gunn diodes. It should be also noted that the frequency dependence of the output power is very complicated (Fig. 1.5), but it is perfectly reproducible.

By means of BWO spectroscopy, it is possible to directly measure power transmittance or reflectance of the sample. The measurement of the transmittance phase can be accomplished too, using a Mach-Zender interferometer with the sample placed in one of its arms. In the other arm, a moving mirror is placed: Its position is controlled by a feedback system in order to remain in an interference minimum upon a change of frequency. The phase of the transmittance is then related to the position of the mirror [10]. Unfortunately, there is a certain temporal separation between the amplitude and phase measurements, which may be disadvantageous in certain situations like measurement of samples exhibiting hysteresis.
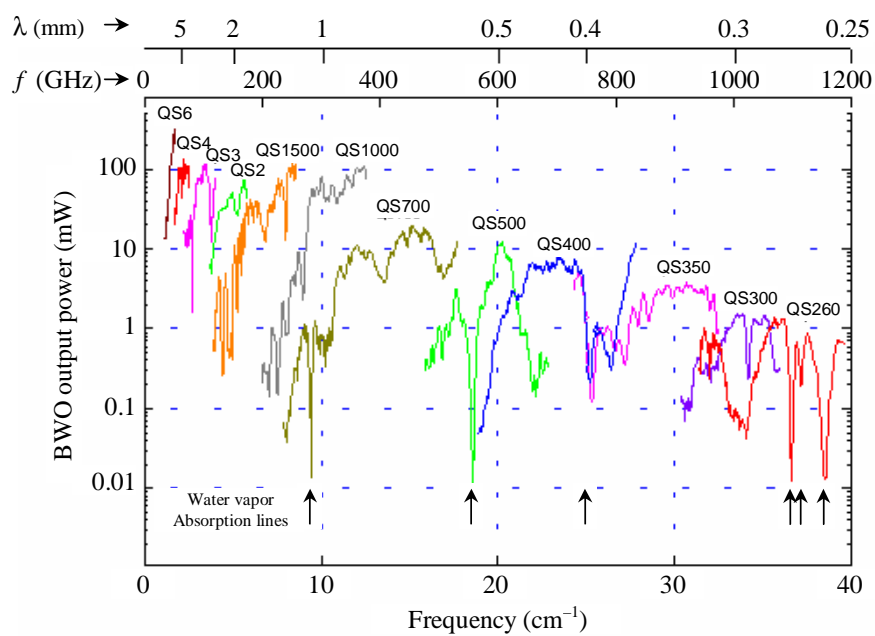
Figure 1.5: Power spectra of several BWO lamps (labelled as QS_i) which continuously cover the frequency range from 1 to $40\,\mathrm{cm}^{-1}$. (After [79].)

Chapter 2

Time-domain terahertz spectroscopy: Methods and applications

We can identify three principle domains of applications, where time-domain THz spectroscopy (TDTS) proves to be an efficient method:

- Conventional steady-state spectroscopy, serving for measurement of dielectric properties. It can be operated in two basic configurations: In transmission and in reflection geometry. As they are extensively used in the thesis, separate sections 2.1 and 2.2 are devoted to their description and to their applications.

  We have developed two novel methods which are based on these configurations. They comprise independent determination of dielectric and magnetic properties of a homogeneous sample, treated in Chap. 3, and characterization of layered structures, described in Sec. 7.2

- Transient dynamics investigations. The commonly used methods include optical pump–THz probe (OPTP) experiments and THz emission spectroscopy, which are briefly discussed in subsequent paragraphs.

- Terahertz-ray ("T-ray") imaging. Besides standard 2D far field imaging, THz tomography and near-field microscopy is also investigated. These techniques are in brief described in page 31.

Optical pump–terahertz probe spectroscopy

In OPTP spectroscopy, the carrier dynamics photo-initiated by a pump pulse is probed by a delayed THz pulse [13]. From the pump-induced change of the probing THz pulse it is possible to extract time-dependent transient conductivity of the sample. Owing to the low energy of THz photons, OPTP spectroscopy constitutes an excellent non-destructive non-contact electrical probe of various transport processes. The data analysis is particularly

simple when only slow processes are investigated. However, careful processing of measured data is required when the system changes on a time-scale comparable to the length of the THz pulse in order to avoid artifacts [80–82].

THz radiation interacts particularly strongly with free carriers. This makes the OPTP spectroscopy an ideal tool for investigating the evolution of free-carrier concentration along with a time-dependent mobility in semiconductors [83–89]. Transient photoconductivity measurements are also of fundamental interest in organic semiconductors, where they allow identification of charge-transport mechanisms [90,91]. Finally, recombination of free quasiparticles created by pump-induced dissociation of Cooper's pairs in superconductors can be efficiently followed by OPTP spectroscopy [92,93].

OPTP studies are not limited to investigation of free carrier dynamics. In particular, dynamics of many-body interactions, formation of coupled phonon-plasmon modes or exciton dynamics have been studied in semiconductors [16,94–96]. Using a time-of-flight-like configuration of OPTP, also optical two-photon absorption in GaAs was measured [97].

Studies of molecular systems remain one of the most challenging applications of OPTP spectroscopy, as the transient THz signal is very weak as a rule [98–101].

Terahertz emission spectroscopy

In the THz emission spectroscopy, THz pulses are not used to probe the sample. Instead, the THz pulses emitted by the sample are analyzed to uncover the underlying photo-initiated carrier dynamics in the sample. Far from the emitter the radiated THz field is proportional to the time-derivative of the transient current flowing through the emitter. It is thus possible to examine evolution of carrier density and/or time-dependent carrier velocity. The temporal resolution of THz emission spectroscopy is defined by the length of optical excitation pulses and detector response rather than by the THz pulse length. Studies with sub-picosecond temporal resolution are thus feasible.

Most of THz emission studies focus on dynamics in semiconductors or semiconductor heterostructures. In conjunction with ~ 100 fs-laser pulses, they allow namely determination of free-carrier lifetimes and mobilities in bulk samples [102]. A richer information can be obtained when shorter laser pulses ($\lesssim 20$ fs) are used. In particular, different regimes of transport, starting from initial ballistic regime over velocity overshoot to steady state drift current, have been resolved in THz emission spectra from p-i-n diodes [103–106]. An exhaustive list of numerous phenomena responsible for THz emission from semiconductor heterostructures is summarized in Ref. [13]; here we mention only interference of light-hole and heavy-hole excitons in a single quantum well [107] and Bloch's oscillations in superlattices [108].

Concerning other materials, THz emission due to the charge transfer has been studied e.g. in superconductors [109,110], charge-ordered manganites [111] and metals [61,62]. A weak THz emission was also observed in betaine-30 dissolved in chloroform [112] and attributed to intramolecular charge transfer.

Terahertz-ray imaging

The terahertz-ray imaging is nowadays widely investigated with regard to potential security applications [12, 113, 114] and medical diagnostics [115–117]. This technique is promising namely due to the high signal-to-noise ratio and sensitivity of TDTS, allowing rapid data acquisition.

The far-field 2D-imaging can be accomplished either by the movement of the sample through the focal point of the THz beam [118, 119], or the entire image can be acquired *en bloc* [120, 121]. 2D THz imaging proves useful e.g. for chemical content mapping, package inspection or moisture analysis [119].

The 3D (tomographic) imaging often relies on the phase sensitivity of TDTS, i.e. it is based on the measurement of the time-of-flight of the THz pulse in layered structures [11, 119]. There are also attempts to study more complex objects by employment of computer-assisted techniques [122, 123]. The depth-resolution was also accomplished by use of a binary lens [121].

The spatial resolution of conventional imaging methods is limited by the radiation wavelength owing to the diffraction, i.e. the spatial resolution is of the order of tenths of millimeters for THz frequencies. Due to the importance of the THz region, there are several attempts to overcome the diffraction limit and construct THz near-field microscopes. The most straightforward approach is to limit the detector area by an aperture. However, such an approach causes strong attenuation of long-wavelength components owing to wave-guiding phenomena in the aperture [124]. Other approaches take advantage of local distortion of the electric field created by a microscopic metallic tip [125]. For example, in a setup by Chen et al. spatial resolution as high as $\sim \lambda/1000$ was achieved [126]. Recently, a method employing a near-field antenna was demonstrated, achieving a resolution $\sim \lambda/200$ [127].

2.1   Transmission spectroscopy

Principle

Time-domain THz transmission spectroscopy (TDTTS) requires two measurements to be performed. In the first one, a THz waveform $E_{\mathrm{sam}}(t)$ transmitted through the investigated sample is measured. In the second measurement, a reference waveform $E_{\mathrm{ref}}(t)$ transmitted through a sample with known properties is acquired. The complex transmittance of the sample $T(f)$ is then calculated as the ratio of Fourier transformations of these waveforms:

$$T(f) = \frac{E_{\mathrm{sam}}(f)}{E_{\mathrm{ref}}(f)}. \tag{2.1}$$

In this way, the instrumental functions including spectral dependence of the incident THz power and detector response functions cancel out, allowing straightforward determination

of the refractive index $n(f)$ of the sample. According to the common practice we assume that the investigated sample is a planparallel slab of homogeneous material irradiated under normal incidence, and that the reference sample is an air layer of equal thickness (i.e., the sample is simply removed). A part of the transmitted THz beam passes directly through the sample while another part exits the sample after a series of internal reflections on the faces of the sample (see Fig. 2.1). The total transmittance of the sample can be expressed as a sum of all these contributions [128]:

$$T(f) = \sum_{k=0}^{\infty} T_k(f) = \frac{4z}{(z+1)^2} \cdot \frac{\exp(2\pi\mathrm{i}fd(n-1)/c)}{1 - \left(\dfrac{z-1}{z+1} \cdot \exp(2\pi\mathrm{i}fdn/c)\right)^2}, \tag{2.2}$$

where the individual contributions read

$$T_k(f) = \frac{4z}{(z+1)^2} \cdot \exp(2\pi\mathrm{i}fd(n-1)/c) \left(\frac{z-1}{z+1} \cdot \exp(2\pi\mathrm{i}fdn/c)\right)^{2k}. \tag{2.3}$$

Here d is the thickness of the sample and z its relative wave-impedance, and c is the velocity of light in vacuum. For non-magnetic samples ($\mu = 1$), the relative wave-impedance z is simply a reciprocal value of the refractive index n. (These expressions are reused in Chap. 3 where both dielectric and magnetic properties of the sample are investigated. Therefore quantities n and $1/z$ are systematically distinguished in Eqs. (2.2)–(2.6) though such a treatment is not required for samples exhibiting purely dielectric behavior.)
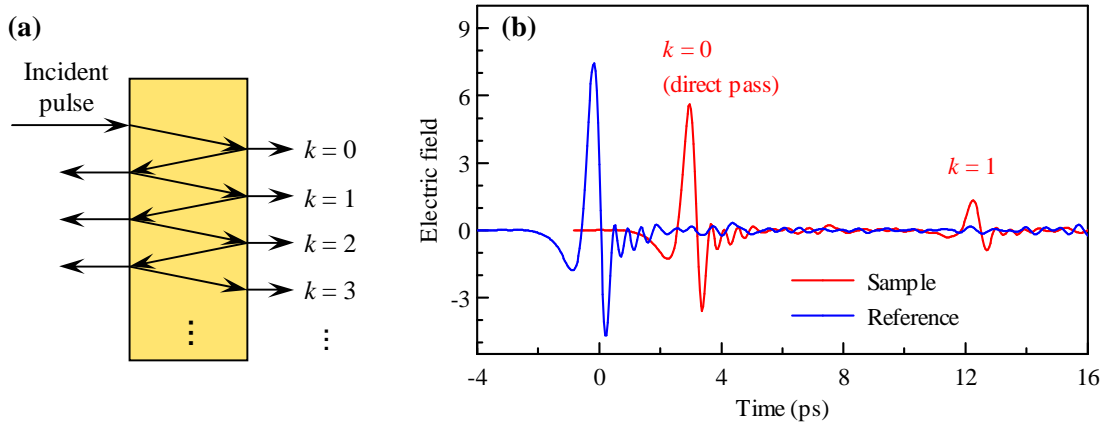
Figure 2.1: (a) Illustration of internal reflections in the sample. The directly passing beam has index $k = 0$. (b) Example of measured waveforms in the presence and absence of a thick sample (red and blue lines, respectively). In this case, the internal reflections are clearly separated in time.

If the sample is optically thick, the individual internal reflections—appearing as a series of echoes in the measured waveform—can be temporally resolved (Fig. 2.1). In this case, single echoes can be time-windowed, making it possible to evaluate the individual contributions $T_k(f)$ [128]. The temporal windowing constitutes an advantage for the evaluation of the refractive index, as the transformation $T_k \to n$ is much simpler than $T \to n$ and it is also less sensitive to errors in measurement.

There are some common peculiarities in both Eqs. (2.2) and (2.3). First of all, these equations cannot be solved analytically, and employment of numerical methods is thus unavoidable. This property itself does not form a major problem. A fast reliable method of the numerical solution has been described e.g. in Ref. [129]. A 2π-periodicity of the complex exponential in these equations anticipates existence of multiple mathematical solutions. The selection of physically correct branch is often evident, but problems may arise especially in spectral ranges with negligible transmittance and for samples exhibiting sharp resonances. In such cases, unique selection of the correct branch relies on measurement of two samples with different thicknesses or on employment of Kramers-Kronig relations [130, 131].

Applications

TDTTS allows accurate determination of optical constants in the far-infrared range. Early experiments focused on precise characterization of materials transparent in the THz region (e.g. crystalline quartz or semi-insulating GaAs) for further use as windows or substrates for THz spectroscopy [9, 132].

THz radiation is a particularly sensitive probe of free-carriers in doped semiconductors [19]: The Drude's conductivity response extends up to the THz range for carrier densities of $10^{14}\,\mathrm{cm}^{-3}$ and higher. The carrier concentration and the momentum relaxation time can be easily deduced from frequency-dependent conductivity using the Drude's model. The high accuracy of TDTTS allows a detailed examination of deviations from Drude's formula, and thus alternative theories of conduction can be verified [133]. The accuracy of TDTTS is nicely illustrated in Ref. [134], where the authors determined the real part of refractive index of silicon with precision exceeding 5 digits (owing to the use of thick samples), and discovered a signature of a weak growth-induced defect.

Many insulators exhibit polar optical phonons in the THz range. Using TDTTS, it is possible to plot the phonon-polariton dispersion [135]. The far-infrared range often contains useful information on soft polar modes and relaxational mechanisms which are frequently responsible for structural (namely ferroelectric) transitions [136]. Knowledge of far-infrared spectra is of particular interest in high-permittivity ceramics as a feedback for elaboration technology [64, 130, 131, 137]. Residual free-carrier concentrations can be also detected.

In polar liquids, the absorption arises due to strong interaction with permanent dipole moments of the individual molecules and subsequent collision-induced relaxation of the

oriented dipoles [138]. Conversely, the interaction used to be weak in non-polar liquids due to the absence of permanent dipole moment and free charge carriers. The observed absorption usually originates from interaction with transient dipole moments induced by collisions [139–141].

TDTTS also brings a valuable information on superconductors. For example, it allowed to uniquely identify the superconducting gap in niobium [142]. In high-temperature super-conductors, TDTTS makes it possible to evaluate the carrier scattering rate, which greatly helps to uncover the underlaying scattering phenomena [143]. Studies of superconductors in magnetic fields were also conducted using TDTTS [144].

Finally, let us mention the applications of TDTTS in chemistry and biology. TDTTS can often detect the presence or even measure absolute concentrations of chemicals [114, 117]. Due to the coherent detection employed in TDTS, the thermal background is sup-pressed and comprehensive studies even of flames could be performed [145]. TDTTS is also a promising technique for label-free characterization of genetic material due to the strong dependence of the complex refractive index on the binding state of deoxyribonucleic acid (DNA) molecules [146].

Experimental setups

The transmission measurements performed within the frame of this thesis have been con-ducted in two laboratories equipped with different THz setups. For our purposes, these setups are well comparable to each other both from the point of view of the accessible spectral range and the accuracy of the measurements.

The first setup (denoted as setup 1 and sketched in Fig. 2.2) operates at the Institute of Physics, Academy of Sciences of the Czech Republic in Prague. It is driven by a Quantronix Odin Ti:sapphire multipass femtosecond pulse amplifier producing $\approx 60\,\text{fs}$, $815\,\text{nm}$ laser
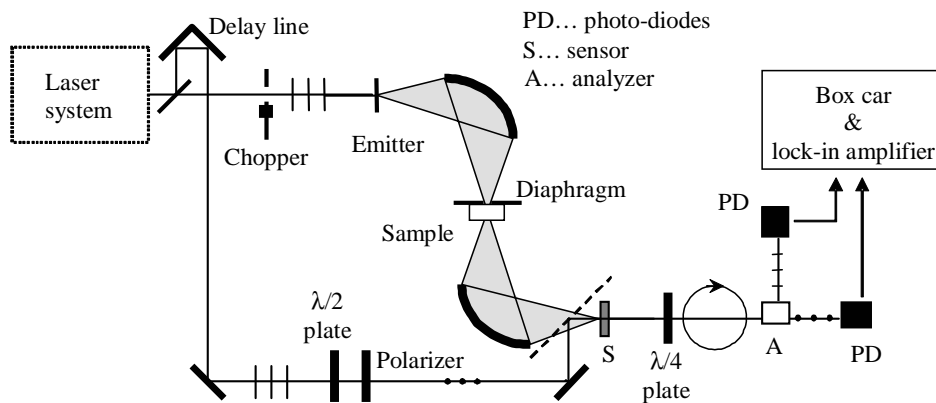
Figure 2.2: Scheme of the setup 1 for TDTTS.

pulses with energy about 1 mJ and repetition rate 1 kHz. About 30 % of the laser power is used to generate THz pulses via optical rectification in a 1 mm thick ⟨110⟩-oriented ZnTe crystal. A pair of ellipsoidal mirrors is used to focus the pulses on a sample and to refocus them to an electrooptic sensor, which consists of another 1 mm thick ⟨110⟩-oriented ZnTe crystal. A strongly attenuated laser beam serves for the gating detection: its ellipticity induced by the THz pulse is measured by a pair of balanced photodiodes (Fig. 1.3a). In order to improve the signal to noise ratio, the detected signal is first pre-filtered in a box-car amplifier, and further integrated in a lock-in amplifier synchronized with a mechanical chopper interrupting the excitation beam at frequency about 166 Hz.

The other setup (denoted as setup 2 and outlined in Fig. 2.3) is functioning at the University of Savoy in France. It is based on an unamplified Tsunami Ti:sapphire laser delivering 120 fs pulses with 800 nm central wavelength and with energy about 3 nJ at 82 MHz repetition rate. THz pulses are generated by optical excitation of a low-temperature-grown GaAs biased photoconductive antenna and pre-collimated with a 4-mm-diameter hyperhemispherical lens fabricated of high-resistivity-silicon. They are further focused to a sample using a pair of paraboloidal mirrors and refocused to a sensor by another pair. The sensor is similar to the emitter except its electrodes are connected to a lock-in current amplifier synchronized with a mechanical chopper interrupting the beam exciting the emitter at frequency about 1 kHz. The instantaneous THz field is thus proportional to the detected current.

2.2   Reflection spectroscopy

Principle and experimental setup

Though TDTTS is fully developed and reliable method, it is applicable to characterization of sufficiently transparent samples only. When the sample strongly attenuates the
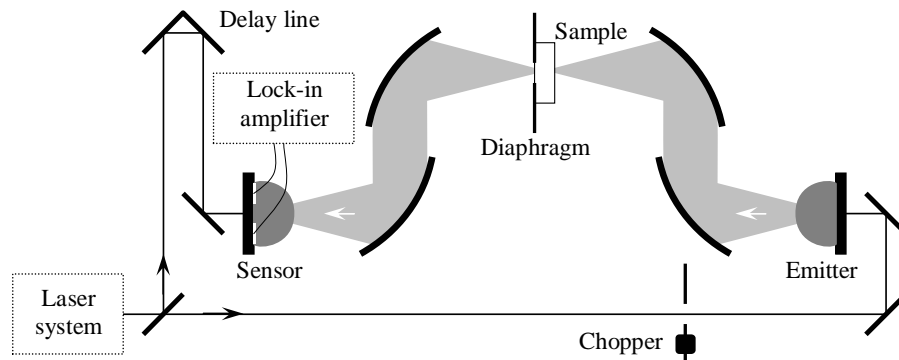
Figure 2.3: Scheme of the setup 2 for TDTTS.

passing THz pulse, the transmission spectroscopy becomes unusable while the reflection spectroscopy could bring the required information. The reflection spectroscopy may be also useful for investigation of thin films on substrates: The determination of film properties from transmission measurements may be very inaccurate owing to the smallness of the phase change induced by the thin film as compared to that induced by the substrate [147].

Like TDTTS, the time-domain THz reflection spectroscopy (TDTRS) requires a reference measurement of a sample with known characteristics, typically of a metallic mirror. The main difficulty of TDTRS consists in a strong dependence of the dielectric function on the reflectance phase: Mispositioning of the sample with respect to the reference mirror as small as $1\,\mu\text{m}$ causes changes in the reflectance phase sufficient to significantly influence the calculated dielectric function [148].

In order to overcome the reflectance phase problem, we have used a specific experimental arrangement described in detail in Ref. [149]. The key idea consists in making the THz beam and the optical gating beam copropagating between the emitter and the sample (Fig. 2.4), in contrast to usual arrangements where the copropagation takes place between the sample and the sensor only. Consequently, the displacement of the sample changes the length for the two beams by precisely the same amount, i.e., no phase change is observed in the measured THz waveform. The THz waveforms are normalized by the intensity of the gating beam reflected from the sample, which is measured by a separate (reference) photodiode. It should be noted that this setup requires an angle of incidence θ to be greater than $\sim 10°$. On the other hand, the setup is well adaptable for measurements in standard cryostats under an angle of incidence $\theta = 45°$.

For samples with sufficient optical thickness, the reflection from the front surface of the sample can be temporally separated from the reflection coming from its rear surface.
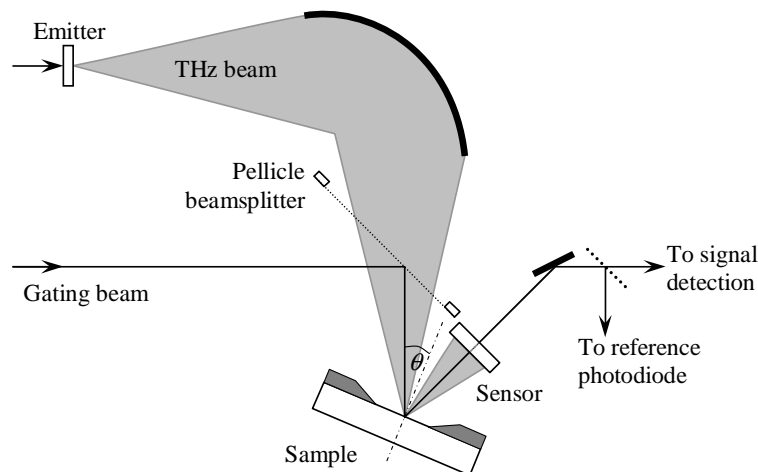
Figure 2.4: Relevant part of the setup for TDTS in the reflection geometry.

In this case the temporal windowing can be used for the data analysis of the time-domain signal. The corresponding reflectance R_0 then reads

$$\text{TM polarization:} \quad R_0 = \frac{\cos\theta - z \cdot \sqrt{1 - \left(\frac{\sin\theta}{n}\right)^2}}{\cos\theta + z \cdot \sqrt{1 - \left(\frac{\sin\theta}{n}\right)^2}} \tag{2.4}$$

$$\text{TE polarization:} \quad R_0 = \frac{z\cos\theta - \sqrt{1 - \left(\frac{\sin\theta}{n}\right)^2}}{z\cos\theta + \sqrt{1 - \left(\frac{\sin\theta}{n}\right)^2}} \tag{2.5}$$

Notice that for small angles of incidence ($\theta \lesssim 15°$) these expressions can be replaced by a simple approximation

$$R_0 \approx \pm \frac{1 - z}{1 + z} \tag{2.6}$$

which makes the determination of the wave impedance (refractive index) very straightforward.

In the present thesis, all the reflectivity experiments were carried out using the experimental arrangement depicted in Fig. 2.4. The rest of the apparatus (i.e. the laser system and methods for generation and detection of THz radiation) is inherited from the setup 1 for TDTTS described in page 34.

Applications

The difficulties with the reflectance phase mentioned above considerably favor usage of transmission spectroscopy. In turn, only few phase-sensitive spectroscopic studies in the reflection geometry have been performed.

A series of interesting studies focused on THz polar properties of liquid water [150–153]. Despite its importance, liquid water still remains a challenging system from both experimental and theoretical point of view due to its complex structural and dynamical properties. Its infrared spectra are related to intermolecular interaction due to permanent and induced dipole moments in the hydrogen bonded network of water molecules.

TDTRS is an important tool for investigation of free-carrier response in doped or thermally excited semiconductors, or in semiconductor epitaxial layers [148, 149, 154–157]. Polar modes in ferroelectric ceramic $SrBi_2Ta_2O_9$ have also been studied using TDTRS [149, 158]. TDTRS seems to be promising for *in vivo* studies, e.g. for skin cancer detection [116].

Chapter 3

Independent determination of dielectric and magnetic properties

Despite the countless spectroscopic studies in the terahertz (THz) region, there are only few studies focusing on the investigation of magnetic materials. Furthermore, most of these works [159–166] put up with postulating that the system exhibits only a dielectric or only a magnetic behavior, but not both at the same time. However, a simultaneous variation of both dielectric permittivity and magnetic permeability is likely to occur e.g. in rare-earth orthoferrites ($YFeO_3$, $TmFeO_3$, etc.) [159, 160], uniaxial antiferromagnetic fluorides (including FeF_2, CoF_2 and MnF_2) [161, 162] and molecular magnets [163]. The magnetic resonances in these materials are usually very narrow while the dielectric resonances are much broader. At the same time, there is a rapidly growing interest in metamaterials and especially in so-called left-handed materials [3, 4, 167–169], where the dispersion of effective dielectric and magnetic properties is very complex and occurs within the same spectral range. The need of reliable methods capable of simultaneous determination of effective dielectric and magnetic functions is also urged by recent demonstrations of metamaterials exhibiting a negative effective permeability in the THz spectral range [170–172].

In this chapter, the time-domain THz spectroscopy (TDTS) technique is extended for investigation of samples exhibiting both dielectric and magnetic properties. We develop and validate three representative approaches allowing simultaneous determination of magnetic and dielectric properties from TDTS measurements. For this purpose, we sum up in Sec. 3.1 basic concepts of the determination of refractive index and wave impedance from transmission and reflection measurements. Next, in Sec. 3.2 we introduce and test experimentally the schemes aiming at simultaneous determination of dielectric and magnetic functions. These schemes are further discussed and their capabilities are compared with each other in Sec. 3.3. The applicability of the developed approaches for the investigation of metamaterials is finally demonstrated in Sec. 3.4.

3.1   Basic concepts

Determination of the permittivity ε and permeability μ—or equivalently, of refractive index $n = \sqrt{\mu\varepsilon}$ and relative wave-impedance $z = \sqrt{\mu/\varepsilon}$—from spectroscopic measurements generally requires the knowledge of complex transmittance and reflectance spectra T and R. Such an approach has been described from the point of view of microwave applications in Ref. [173], but it was applied only to numerically calculated transmittance and reflectance spectra. In practice, this method is very sensitive to accurate determination of the sample thickness as well as to precise measurement of both reflectance and transmittance spectra [164, 174].

However, for the simultaneous determination of n and z, it is sufficient to choose any pair of independent measurable complex functions depending on these quantities. Thanks to the possibility of temporal windowing offered by TDTS, the spectra of n and z can be extracted from a pair of spectral functions corresponding to internal reflections (echoes). Fox example, the pairs $[T_0, R_0]$ or $[T_0, T_1]$ can be used (cf. Eqs. (2.3) and (2.6)). Such an approach brings an additional benefit: The dependence of T_k and R_k on n and z is much simpler compared to that of T and R and the extraction procedure is more direct and transparent. We show in the next section that the THz optical properties n and z can be obtained analytically from the experimental data in many cases: This avoids problems with crossing of branches of mathematical solutions encountered when R and T are only considered [174].

Based on the choice of measured quantities, several representative approaches for simultaneous determination of n and z can be devised. In the next section, we examine in detail the following methods:

- **Method A**
  Measurement of the transmittance and reflectance corresponding to the main echo (T_0 and R_0 are measured).

- **Method B**
  Measurement of the transmittance corresponding to the main and to the first echo (T_0 and T_1 are measured).

- **Method C**
  Measurement of the transmittances $T_{A,0}$ and $T_{B,0}$ corresponding to the main echo for two samples with different thicknesses d_A and d_B, respectively.

This list is not exhaustive. Approaches based on spectra corresponding to higher-order internal reflections can be naturally derived from this list, nevertheless we expect that potential advantages (lower noise, possibility of thickness refinement [175]) cannot bring at this stage significant improvement of the state of the art.

3.2   Experimental results

Transmittance and reflectance of the main echo (method A)

In the framework of this strategy, the values of optical properties n and z are simultaneously extracted from the reflectance R_0 and transmittance T_0 spectra corresponding to the directly passing pulses. The equation for the transmittance T_0 is then particularly simple, as the measurement can be performed under normal incidence (Eq. (2.3)). The reflectance measurement must be performed under oblique incidence ($\theta = 15°$ and s-polarized beam was employed in this study), therefore Eq. (2.5) has to be used. The set of Eqs. (2.3) and (2.5) was solved numerically for n and z.

Note however, that Eq. (2.5) can be well approximated by Eq. (2.6) for small angles of incidence. In such a case, the numerical extraction procedure can be replaced by an analytical one. First, the impedance is determined from the measured reflectance spectrum using Eq. (2.6):

$$z \approx \frac{1 + R_0}{1 - R_0} \tag{3.1}$$

(the error is about $3\,\%$ for $\theta = 15°$ and $z = 1/3.2$). Subsequently the refractive index is obtained from Eq. (2.3):

$$
\begin{aligned}
\operatorname{Re} n &= 1 + \frac{c}{2\pi f d}\left(\arg T_0 - \arg \frac{4z}{(z+1)^2} + 2\pi m\right), \\
\operatorname{Im} n &= \frac{c}{2\pi f d}\left(\ln\left|\frac{4z}{(z+1)^2}\right| - \ln|T_0|\right).
\end{aligned}
\tag{3.2}
$$

As it has been pointed out in Sec. 2.1, these equations always yield several branches of mathematical solutions (indexed by the integer m in Eq. (3.2)) and the physically correct branch has to be selected.

This approach was tested using a low-resistivity $0.885\,\mathrm{mm}$ thick ZnTe crystal. The THz properties of the sample determined from the measured transmittance and reflectance spectra T_0 and R_0 are summarized in Fig. 3.1. Due to its small size, the sample was fixed to an aperture with a diameter of $3.5\,\mathrm{mm}$. This implies that low-frequency components can be affected by parasitic diffraction effects, hence they are cut in the graphs. We can clearly observe the contribution of free carrier absorption in the plot of the complex refractive index. We can also identify a weak superimposed resonance around $1.7\,\mathrm{THz}$, which has been attributed to the TA(X) phonon [176]. Note however, that both these features are relatively weak and that they are hidden by the noise in the plots of complex impedance. In agreement with the assumption of a non-magnetic response of ZnTe at THz frequencies, we find that the permeability fits well the value $1 + 0\mathrm{i}$ (within the experimental noise).

Another material characterized by this method was the rare-earth orthoferrite TmFeO$_3$ [160]. The sample used was a $0.916\,\mathrm{mm}$ thick planparallel plate. Its normal was parallel to
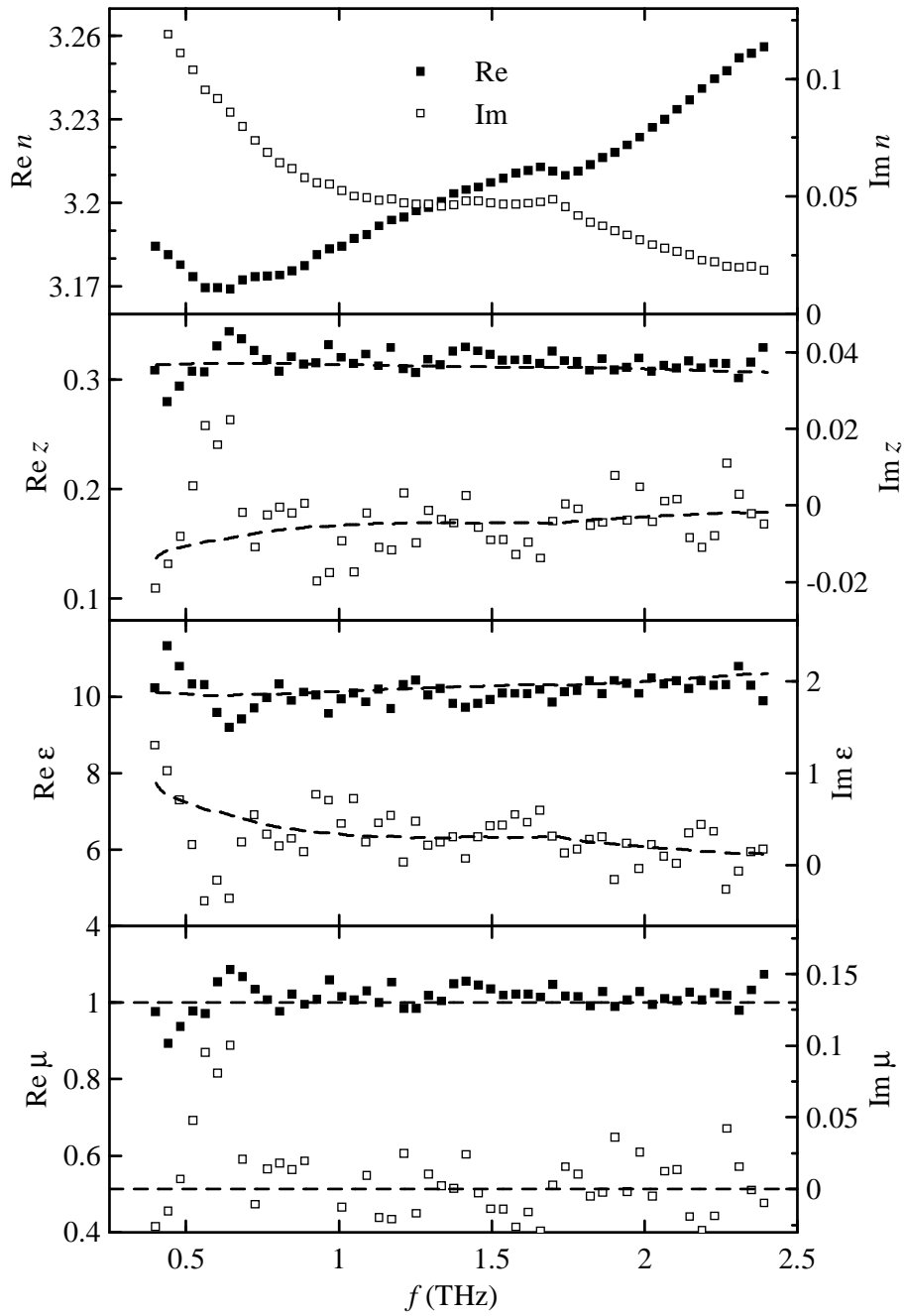
Figure 3.1: Refractive index n, wave impedance z, permittivity ε and permeability μ of the investigated ZnTe sample, extracted from the transmittance T_0 and reflectance R_0 corresponding to the main echo. The dashed lines indicate the results of evaluation of refractive index from the transmittance measurement assuming a non-magnetic sample ($\mu = 1$, i.e., $z = 1/n$).

the b crystallographic axis and it was oriented in the experiments so that the THz electric field was parallel to the a-axis. In this geometry, the THz spectra are expected to present a sharp antiferromagnetic mode at 0.7 THz [159]. As it is observed in Fig. 3.2, this very weak resonance is detected in the spectrum of the complex refractive index. The variation of the refractive index induced by the antiferromagnetic mode corresponds approximately to 1 % of the background value of Re n, thus exceeding the noise level by about an order
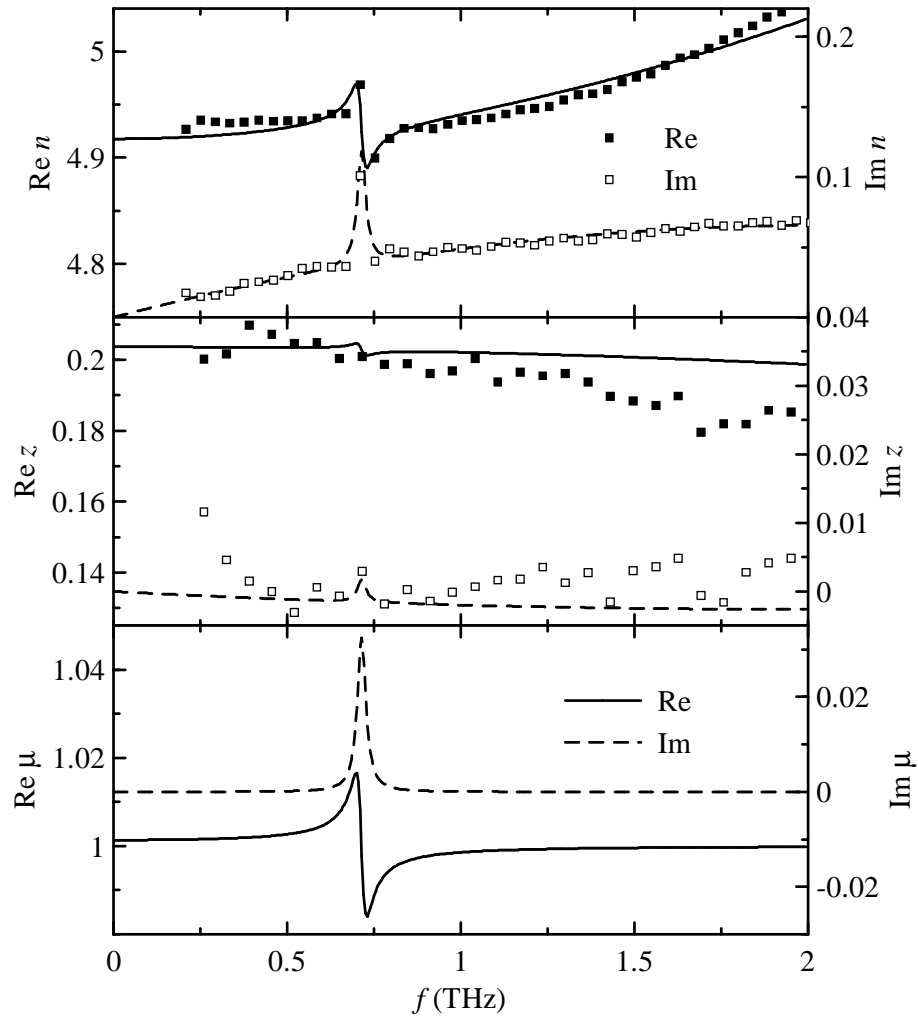
Figure 3.2: Refractive index n and impedance z of $TmFeO_3$ extracted from the transmittance and reflectance measurements corresponding to the main echo ($E \parallel a$, $H \parallel c$. Lines: fit of the spectra assuming a sharp magnetic resonance and a slow dielectric variation corresponding to a tail of a phonon mode. The resonance in the magnetic permeability results from the fit of the refractive index.

of magnitude. In contrast, the resonance is too weak to be observed in the spectrum of the complex impedance.

As it will be discussed in Sec. 3.3, the accuracy of the determination of the permittivity and permeability depends critically on the experimental error of the impedance spectrum. It is then clear that it is not possible to determine unambiguously whether the character of the observed mode is dielectric or magnetic from the measured data. It is worth to evaluate how much the precision of the impedance determination has to be improved in order to enable the unambiguous determination of the observed mode. For this purpose we have performed a simultaneous fit of the measured n and z using a model of a magnetic spectrum presenting a single underdamped harmonic oscillator and a dielectric spectrum exhibiting a slow variation related to a tail of a higher-frequency phonon mode. The results of this fit along with the calculated permeability are shown in Fig. 3.2. Apparently the magnetic mode induces a variation in the impedance spectrum of about $1\,\%$ of the value of $\mathrm{Re}\,z$ which is slightly below the noise level ($\approx 2\,\%$) observed in this part of the spectrum.

Transmittance of the main and of the first echo (method B)

This approach consists in measuring the transmittances T_0 and T_1 corresponding to the main pulse and to the first internal reflection respectively (cf. Eq. (2.3) with $k = 0$ and $k = 1$ respectively). The major advantages of this method are (i) the possibility of measurement under normal incidence, and (ii) the use of a single experimental setup instead of two considerably different configurations as required by the previous method. The determination of the THz properties of the sample is fully analytical. First, the impedance spectrum is determined from

$$\frac{T_0^3 \exp(4\pi \mathrm{i} f d/c)}{T_1} = \left(\frac{4z}{z^2 - 1} \right)^2 \tag{3.3}$$

and subsequently, the refractive index is obtained from Eqs. (3.2).

Note that the measured waveform may contain parasitic echoes from the emitter, detector and other optics. These artifacts should be avoided unless the first sample echo is separated from them in time.

We validate this method using a $0.452\,\mathrm{mm}$ thick sapphire crystal. The results of the measurements are shown in Fig. 3.3. The refractive index exhibits a flat response in agreement with Ref. [9].

Transmittance of samples with different thicknesses (method C)

The last approach is based on a measurement of transmittances $T_{A,0}$ and $T_{B,0}$ corresponding to the main echoes of two samples with different thicknesses (d_A and d_B). The
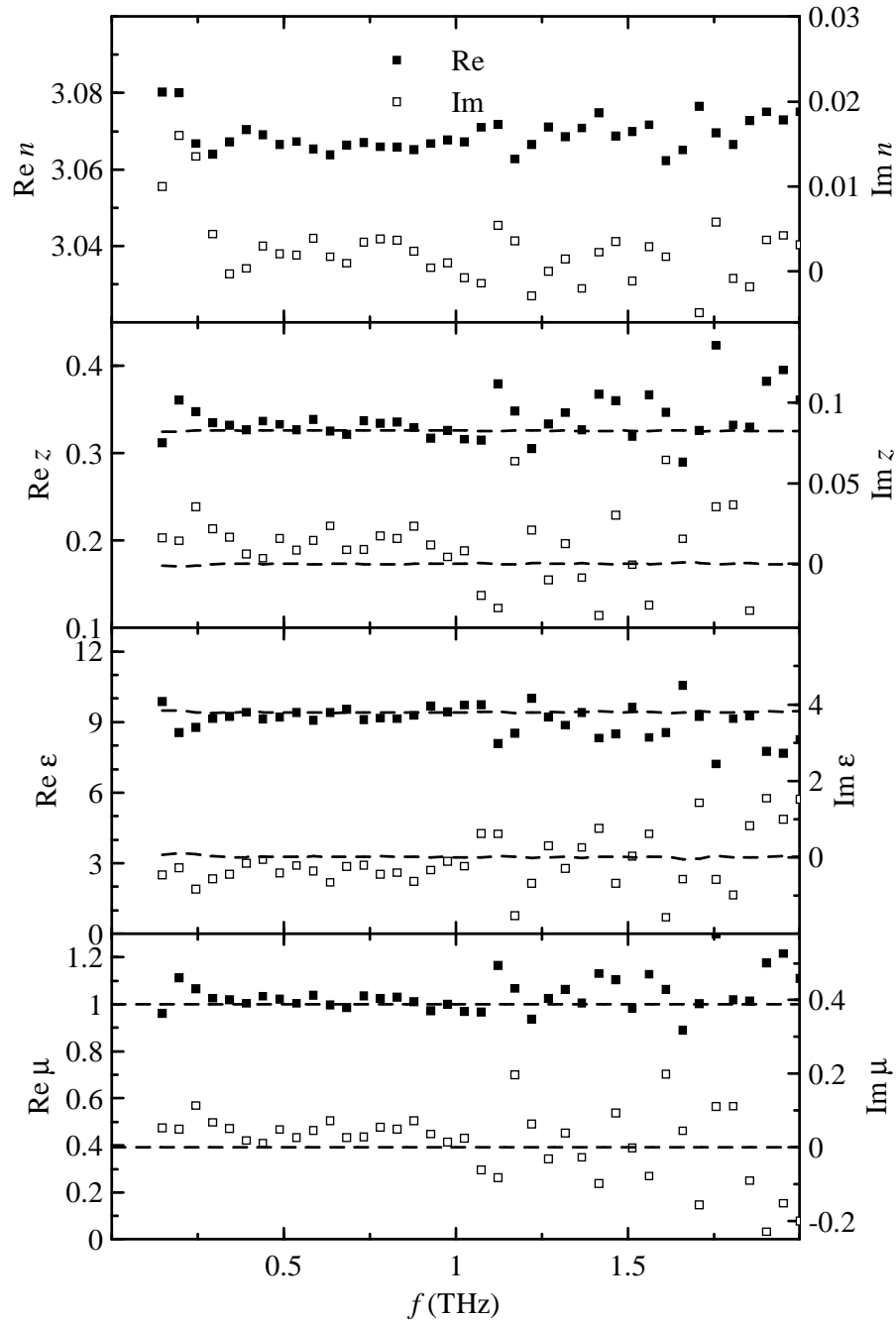
Figure 3.3: Refractive index n, wave impedance z, permittivity ε and permeability μ of the investigated sapphire sample, extracted from the transmittance corresponding to the main and to the first echo. The dashed lines indicate the evaluation of refractive index assuming a non-magnetic sample ($\mu = 1$, i.e., $z = 1/n$).

applicability of this method can be sometimes limited, since two samples of the same compound with different thicknesses should be available. The determination of the THz properties is based on a simultaneous inversion of two equations of the form (2.3) ($k = 0$) where d is replaced by d_A and d_B, respectively.

The calculations are straightforward as the ratio of transmittances $T_{A,0}/T_{B,0}$ directly yields a formula independent of the impedance

$$\frac{T_{A,0}}{T_{B,0}} = \exp\left(2\pi i (n-1) f (d_A - d_B)/c\right) \tag{3.4}$$

while the impedance can be analytically obtained from

$$(T_{B,0})^{\frac{d_A}{d_A - d_B}} (T_{A,0})^{\frac{d_B}{d_B - d_A}} = \frac{4z}{(z+1)^2} . \tag{3.5}$$

This method was checked using two teflon slabs with thicknesses 2.02 and 3.95 mm. The THz properties of the teflon determined by this method are displayed in Fig. 3.4. The flatness of the refractive index agrees very well with the data in Ref. [10].

3.3 Discussion

All the presented methods have several important characteristics in common. A brief inspection of plots of the refractive indices in Figs. 3.1–3.4 allows us to conclude that the refractive index can be determined very accurately, provided the determination of the sample thickness is accurate. The noise level of the data plotted in these figures is smaller than 0.01, i.e. few tenth of percent of the real part value. This can be quantitatively understood on the basis of Eq. (3.2) assuming real z. Increase of the sample thickness d is connected to an equivalent increase of the term $(\arg T_0 + 2m\pi)$ so that m is incremented each time when the value of $\arg T_0$ passes over the discontinuity at 2π. As the experimental error of $\arg T_0$ is independent of the sample thickness, the measurement of a very thick sample can provide a very accurate value of the real part of the refractive index with an experimental error scaling as $1/d$. Quantitatively, the relative errors of the complex refractive index caused by the noise in the measured spectra can be easily found by differentiating Eqs. (2.3) and (2.6):

$$\text{Method A:} \qquad \frac{\Delta n}{n} = \frac{c}{2\pi i f n d} \left(\frac{\Delta T_0}{T_0} + \frac{(1-z)^2}{2z} \frac{\Delta R_0}{R_0} \right) \tag{3.6}$$

$$\text{Method B:} \qquad \frac{\Delta n}{n} = \frac{c}{2\pi i f n d} \left(\frac{6z - z^2 - 1}{2(1+z^2)} \frac{\Delta T_0}{T_0} + \frac{(1-z)^2}{2(1+z^2)} \frac{\Delta T_1}{T_1} \right) \tag{3.7}$$

$$\text{Method C:} \qquad \frac{\Delta n}{n} = \frac{c}{2\pi i f n (d_A - d_B)} \left(\frac{\Delta T_{A,0}}{T_{A,0}} - \frac{\Delta T_{B,0}}{T_{B,0}} \right) \tag{3.8}$$
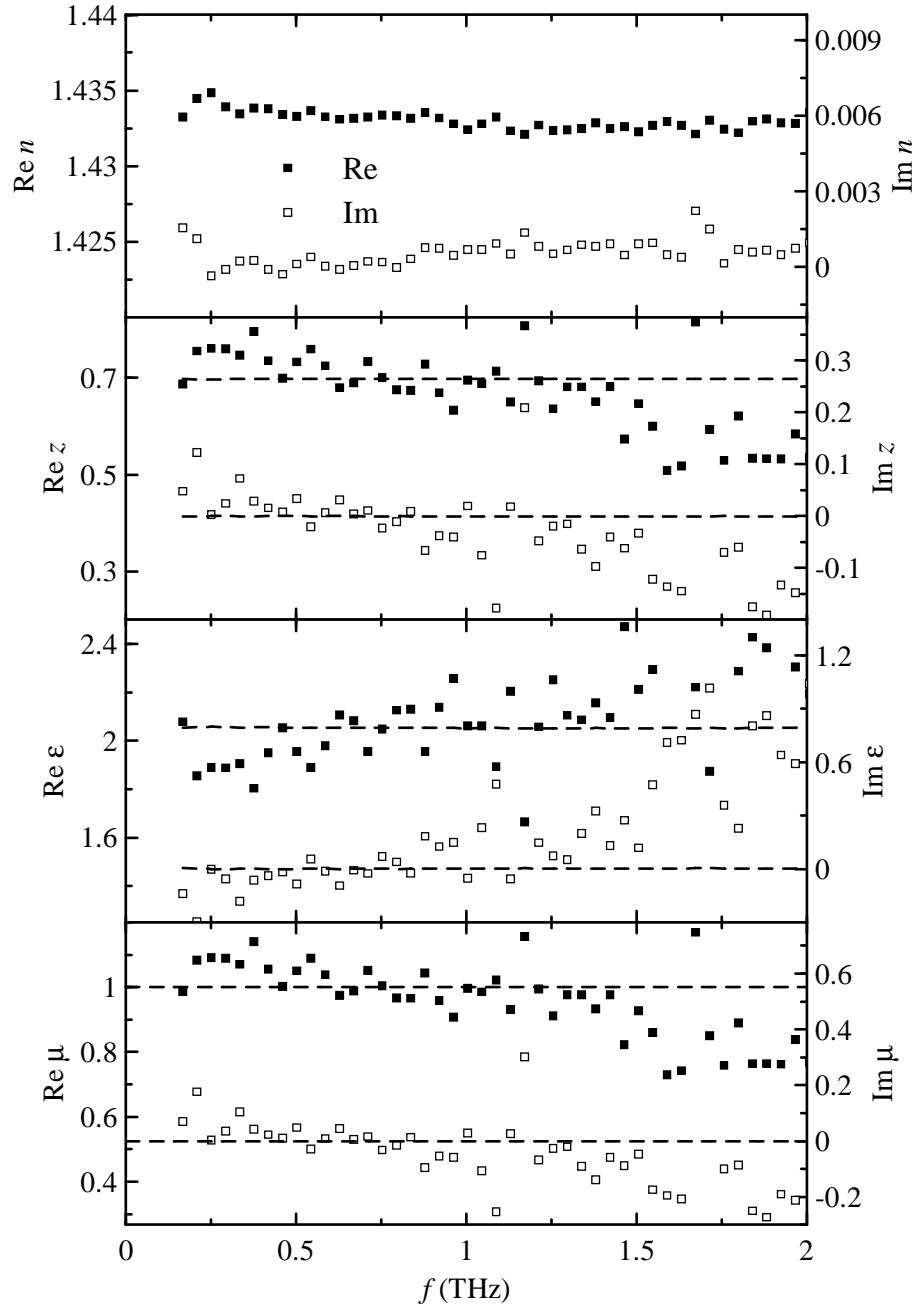
Figure 3.4: Refractive index n, wave impedance z, permittivity ε and permeability μ of the teflon, extracted from transmittances corresponding to main echoes of two samples with different thicknesses. The features around 1.2 and 1.7 THz are caused by water-vapor absorption. Dashed lines correspond to the evaluation based on the measured complex refractive index and on the assumption of a non-magnetic sample ($\mu = 1$, i.e., $z = 1/n$).

The errors of the measured reflectance and transmittance spectra ΔR_0 and ΔT_k, respectively involve both amplitude and phase error terms:

$$
\begin{aligned}
\frac{\Delta R_0}{R_0} &= \frac{\Delta|R_0|}{|R_0|} + \mathrm{i}\Delta\phi\,, \\
\frac{\Delta T_k}{T_k} &= \frac{\Delta|T_k|}{|T_k|} + \mathrm{i}\Delta\phi_k\,.
\end{aligned}
\tag{3.9}
$$

The expected increase of accuracy with increasing thickness clearly appears in Eqs. (3.6)–(3.8). Note however, that the precision of the determination of the refractive index in method C is controlled by the thickness difference $d_A - d_B$ of the two samples used rather than by the sample thickness itself. The variation of $|\Delta n/n|$ versus z is shown in Fig. 3.5a at $f = 1\,\mathrm{THz}$ and for the optical thicknesses nd and $n(d_A - d_B)$ equal to $0.7\,\mathrm{mm}$ (both n and z are assumed to be real for the sake of clarity). As it is observed, the experimental error is of the order of $0.1\,\%$ for all the tested methods in agreement with the experimental results.

It is necessary to stress that the thickness of the sample is limited by absorption losses. In order to avoid excessive absorption in the frequency range of interest 0.2–$2.0\,\mathrm{THz}$ while keeping the maximum thickness possible, it is optimal to approximately fulfill the condition $d \cdot \mathrm{Im}\, n \approx 0.05\,\mathrm{mm}$. Note also that thick samples ($d \cdot \mathrm{Re}\, n \gtrsim 0.7\,\mathrm{mm}$) are required in order to temporally resolve the internal reflections of ps-time duration THz pulses.

The impedance is always determined by a solution of an algebraic equation parameterized by the measured transmittances or reflectance (cf. Eqs. (3.1), (3.3) and (3.5)). The precision of z is thus determined by the spectroscopic performance of the given setup, which depends mainly on the scan-to-scan reproducibility of the signal and on the noise of the femtosecond laser system. In the case of reflectance measurements, it is also critically dependent on the correct reflectance phase determination. Anyway, the accuracy of the impedance spectra is not critically dependent on the value of the sample thickness. Strictly speaking, the sample thickness appears in Eqs. (3.3) and (3.5) as an additional parameter to be accurately determined, therefore a possible error Δd in this parameter may decrease the accuracy of the impedance value.

The permittivity and permeability can be expressed respectively as the ratio and product of the refractive index and impedance. Their accuracy is thus controlled by the quantity obtained with the least precision, i.e. by the impedance in our case. Improvement of the impedance accuracy is thus of prime importance. For this reason we compare the presented experimental approaches from the point of view of the sensitivity of z to the errors in the measured T_k and R_0 spectra. In the THz range, the inequality $\varepsilon > \mu$ holds for a large majority of materials, i.e. $0 < z < 1$. For clarity we restrict our discussion to this interval even if the formulae below permit its extension to any value of z. When we speak about low-impedance compounds we refer to materials with $z \approx 0.2$; by high-impedance compounds, materials with $z \approx 0.75$ are meant.
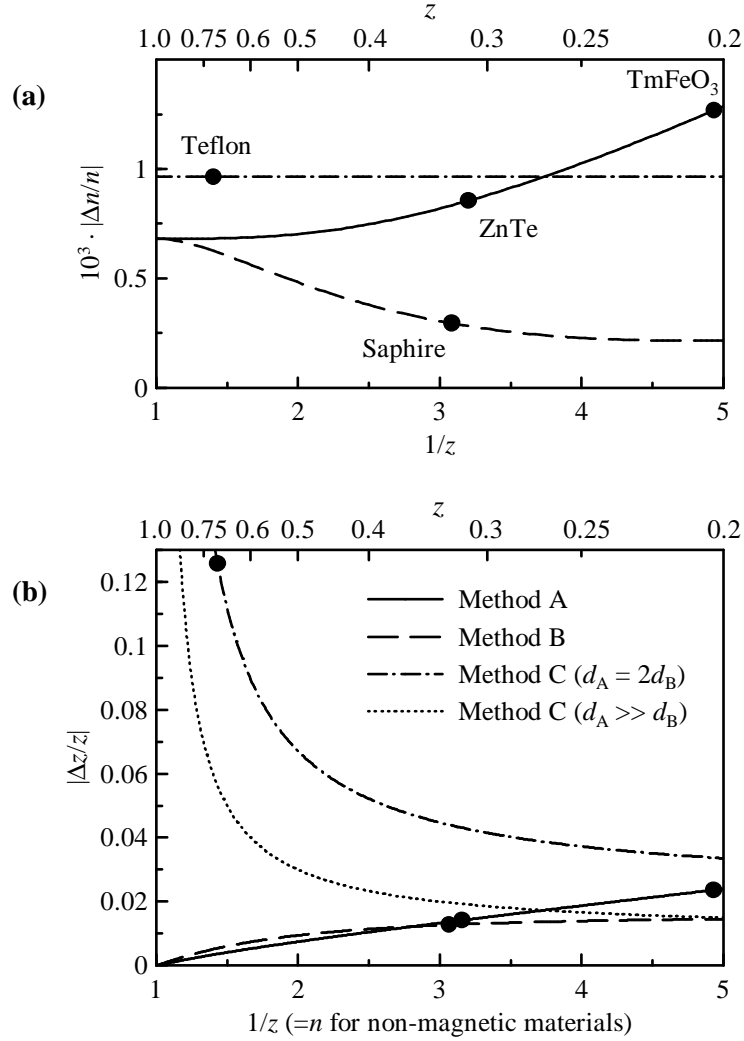
Figure 3.5: Relative errors $\Delta n/n$ (a) and $\Delta z/z$ (b) versus reciprocal impedance for the three methods discussed in the text assuming real n and z. (a) Plots based on Eqs. (3.6)–(3.8); $f = 1\,\mathrm{THz}$; $nd = 0.7\,\mathrm{mm}$ and $n(d_A - d_B) = 0.7\,\mathrm{mm}$. (b) Plots based on Eqs. (3.10), (3.11) and (3.13). The errors in the determination of the transmittances ($|\Delta T_k/T_k|$) and reflectance ($|\Delta R_0/R_0|$) spectra are assumed to be independent and equal to 0.01. The sample thickness is assumed to be determined exactly. Points on the curves represent impedances of the samples studied in this work.

Concerning the method A, Eq. (3.1) can be applied for small incidence angles. Its differentiation leads to the following estimation of the errors:

$$\frac{\Delta z}{z} = \frac{\Delta R_0}{R_0} \frac{z^2 - 1}{2z} . \tag{3.10}$$

The variation of the relative error $|\Delta z/z|$ versus $1/z$ is shown by the solid line in Fig. 3.5b assuming a real z and a 1% error in the reflectance determination ($|\Delta R_0/R_0| = 0.01$). For the investigated ZnTe sample, the last multiplicative term appearing in the right-hand side of Eq. (3.10) amounts approximately to 1.5 while $|R_0| \approx 0.5$. Consequently, Eq. (3.10) accounts for the noise level of $\Delta z \approx 0.01$–0.02 observed in Fig. 3.1. Note also in Fig. 3.5b that $|\Delta z/z|$ is smaller for higher values of impedance, so that it is about two times higher for TmFeO$_3$ than for ZnTe.

The situation is slightly more complex for the method B. First, let us assume that the thickness of the sample is exactly known. One then finds using Eq. (3.3):

$$\frac{\Delta z}{z} = \left[3\frac{\Delta T_0}{T_0} - \frac{\Delta T_1}{T_1} \right] \frac{1 - z^2}{2(1 + z^2)} \,, \tag{3.11}$$

The variation of the relative error $|\Delta z/z|$ versus $1/z$ is shown by the dashed line in Fig. 3.5b assuming that errors in the determination of T_0 and T_1 are independent and equal to 0.01. Numerically, this leads to similar values of Δz as in the previous case. In reality, for absorbing samples, the relative error in T_1 is expected to be larger than that in T_0. Note also that the uncertainty of the transmittance phase $\Delta\phi_j \propto f$ so that the uncertainty in the impedance value increases for high frequencies. This effect is clearly observed in Fig. 3.3 for frequencies higher than $1\,\mathrm{THz}$.

Concerning the effect of the uncertainty in the sample thickness Δd, one finds:

$$\frac{\Delta z}{z} = 2\pi i f \Delta d/c \, \frac{1 - z^2}{1 + z^2} \,. \tag{3.12}$$

This may introduce a systematic error which increases with frequency and reaches about 0.01 at $2\,\mathrm{THz}$ for an error as small as $1\,\mu\mathrm{m}$ in the absolute sample thickness determination.

Finally, we investigate the last method (C). Providing that the thicknesses of both samples are exactly known, differentiation of Eq. (3.5) leads to:

$$\frac{\Delta z}{z} = \left[\alpha\frac{\Delta T_{B,0}}{T_{B,0}} + \beta\frac{\Delta T_{A,0}}{T_{A,0}} \right] \frac{1 + z}{1 - z} \,, \tag{3.13}$$

where $\alpha = d_A/(d_A - d_B)$ and $\beta = d_B/(d_B - d_A)$. It clearly appears that the thicknesses of the two samples have to be chosen quite different from each other to minimize this error. In this study we have chosen $d_A \approx 2d_B$, i.e. $\alpha \approx 2$ and $\beta \approx -1$.

The term $(1 + z)/(1 - z)$ in Eq. (3.13) can take values from about 1.5 for materials with a low z to nearly 10 for high-impedance samples (cf. dotted line in Fig. 3.5b). We clearly see in Fig. 3.5b that high-impedance samples (like teflon chosen for our study) exhibit a considerably higher experimental error Δz than low-impedance ones. Indeed, for low-impedance samples the magnitude of the experimental error in Δz is found to be nearly comparable to that obtained in the analysis of the method B, while for high-impedance

samples it may increase by a factor of 10. This is observed in Fig. 3.4 (high-impedance sample) where the magnitude of Δz reaches 0.1 even for low frequencies.

Accounting for the uncertainty in the thickness of sample A (Δd_A) yields:
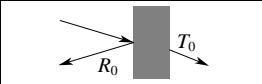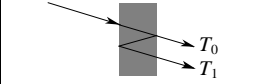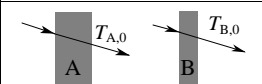
$$\frac{\Delta z}{z} \approx \Delta d_A \frac{d_B}{d_A - d_B} \frac{2\pi \mathrm{i} n f}{c} \frac{1+z}{1-z} \, . \tag{3.14}$$

Again, the systematic error introduced by this term will be significant especially for high-impedance compounds and at higher frequencies. We come to the same conclusion as above that the two samples should have quite different thicknesses, to minimize the experimental error. The main features of the three experimental methods discussed above are summarized in Tab. 3.1.

In our experiments the smallest variation of the magnetic permeability detectable in the impedance spectrum was about 0.1 (Fig. 3.2). We have seen that this is not sufficient to determine unambiguously the dielectric versus magnetic character of the resonance observed in $TmFeO_3$, the latter one being too weak ($\Delta\mu \approx 0.02$ [159]). On the other hand, the magnetic certain metamaterials may be sufficiently strong to be measurable by the methods developed in this chapter. This is even more likely in metamaterials exhibiting negative refraction, as they must necessarily present a spectral range with negative effective permeability and good transparency.

3.4 Application to metamaterials

In the introduction we claimed that the developed approaches can be used for investigating the metamaterials regardless their internal structure, provided the size of their unit cell is much smaller than the wavelength [169, 170, 177]. In such a case it is not necessary to consider the multiple reflections from each motif; therefore the metamaterial can be described

Method	Scheme	Experiment	Precision	Sample thickness
A	T_0 R_0	Two different setups required	Good	To be optimized for T_0
B	T_0 T_1	Very simple; parasite echoes should be avoided	Good at low frequencies; (can be worse at high frequencies)	– To be optimized for T_0 and to avoid excessive attenuation of T_1 – Precise knowledge is essential
C	$T_{A,0}$ $T_{B,0}$ A B	Two samples required	Medium; bad at high frequencies and/or for low impedance	Precise knowledge is essential

Table 3.1: Summary of specific properties of the three approaches presented in this chapter. All transmittance measurements are performed under normal incidence.

using an effective frequency-dependent permittivity and permeability. Consequently, the temporal windowing—which is the basis of all the described methods—can be applied. In order to provide a clear evidence of this, we performed a numerical simulation of a structure exhibiting an effective magnetic behavior, similar to that proposed by O'Brien and Pendry [177].

We studied a 2D-array of square dielectric rods with permittivity $\varepsilon_{\mathrm{rods}} = 200 + 5\mathrm{i}$, arranged in a square lattice with a period of $a = 50\,\mu\mathrm{m}$ (Fig. 3.6). The volume filling factor was equal to 0.5. The structure consisted of 256 periods along the propagation direction. The simulation was performed using the computer code (transfer matrix method) developed in the framework of this thesis and described in detail in Chap. 5. This code yields complex transmittance and reflectance spectra of this structure in the THz range (see Fig. 3.7a). The dispersion has its origin in the resonant character of the structure, which was shown to be related to the Mie resonances in the high-permittivity rods. The observed behavior can be described by an effective magnetic response [177].

These spectra can be used to calculate the expected transmitted and reflected wave-forms from the incident one (see Fig. 3.7b); the model incident waveform was chosen such that its spectrum approximatively matches that of the THz pulses delivered by our experimental apparatus. We can clearly resolve the echoes arising from the internal reflections at the faces of the sample. In this sense, all the methods developed in this chapter can be applied for the determination of the effective dielectric and magnetic response functions of the sample. In practice, the method B seems to be the best suited, as phase-sensitive reflectance measurement (required in method A) and preparation of samples with two different thicknesses (method C) may be difficult for metamaterials.

All the three methods developed in this chapter were used to extract the effective optical properties from the simulated waveforms. The results of methods A and B are summarized in Fig. 3.8; results of the method C are very similar and therefore they are
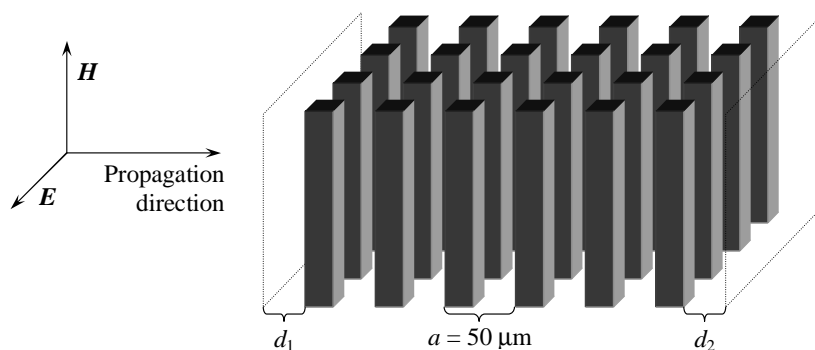
Figure 3.6: Scheme of the investigated metamaterial. The real structure consists of 256 periods along the propagation direction while it is infinite in the remaining two directions. The extent of the metamaterial is defined by the planes indicated by the dotted lines.
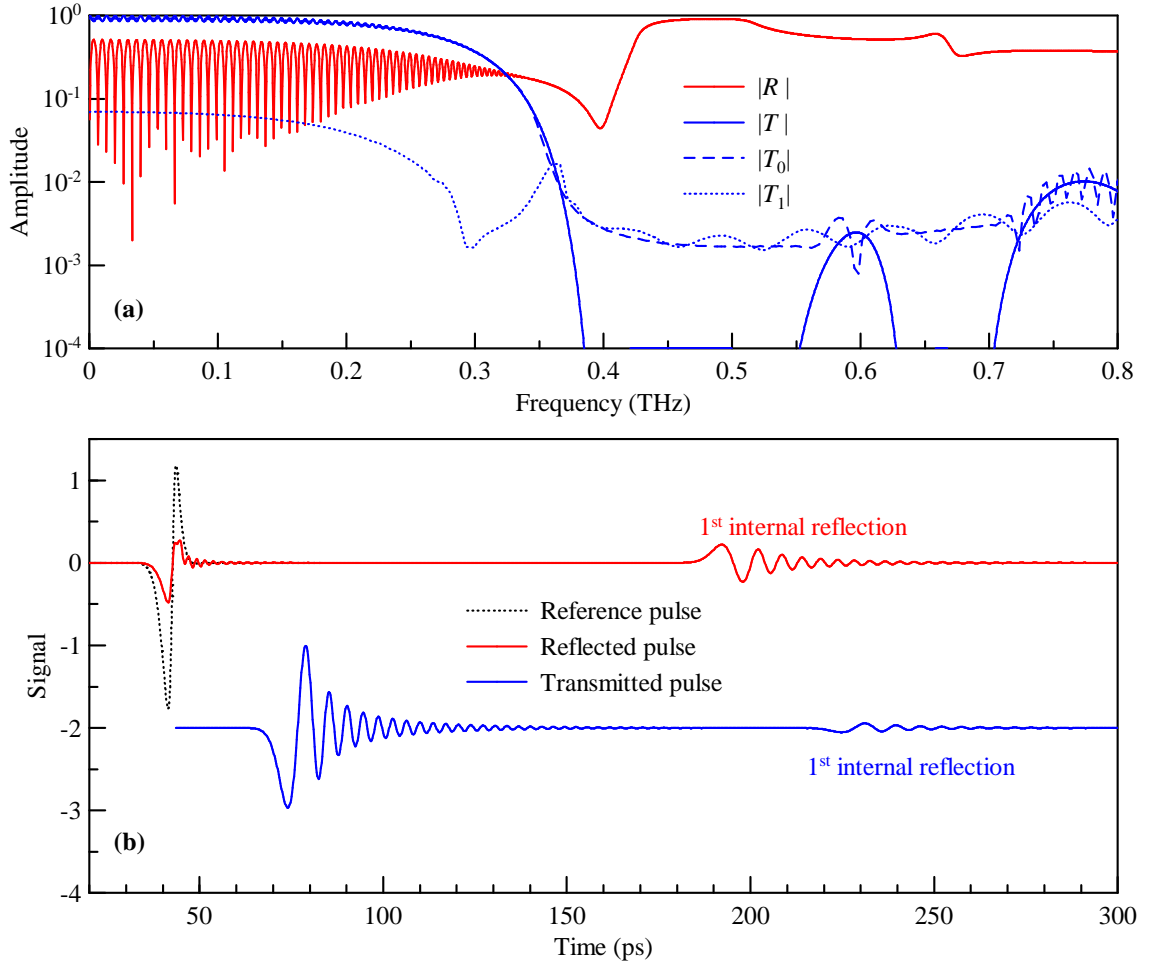
Figure 3.7: (a) Transmittance and reflectance spectra of the investigated metamaterial. $|R|$ and $|T|$ are the amplitude reflectance and transmittance of the structure, respectively, obtained by the computer simulation described in the text. $|T_0|$ and $|T_1|$ is the amplitude transmittance of the main echo and of the first internal reflection, respectively, obtained from the time-domain signal in figure (b) using the temporal windowing. (b) Time-domain waveforms. The transmitted and reflected pulses were calculated from the reference one using the complex transmittance and reflectance spectra respectively. The internal reflections can be temporally resolved in the THz pulse passing through and reflected from the metamaterial. The transmitted pulse is vertically shifted for graphical clarity.

not presented here. The simultaneous increase of the refractive index and wave impedance versus frequency indicates an effective magnetic behavior. Indeed, the real part of the magnetic permeability shows an onset of the magnetic resonance, while the dielectric response remains flat in the spectral range studied. The behavior of the effective properties
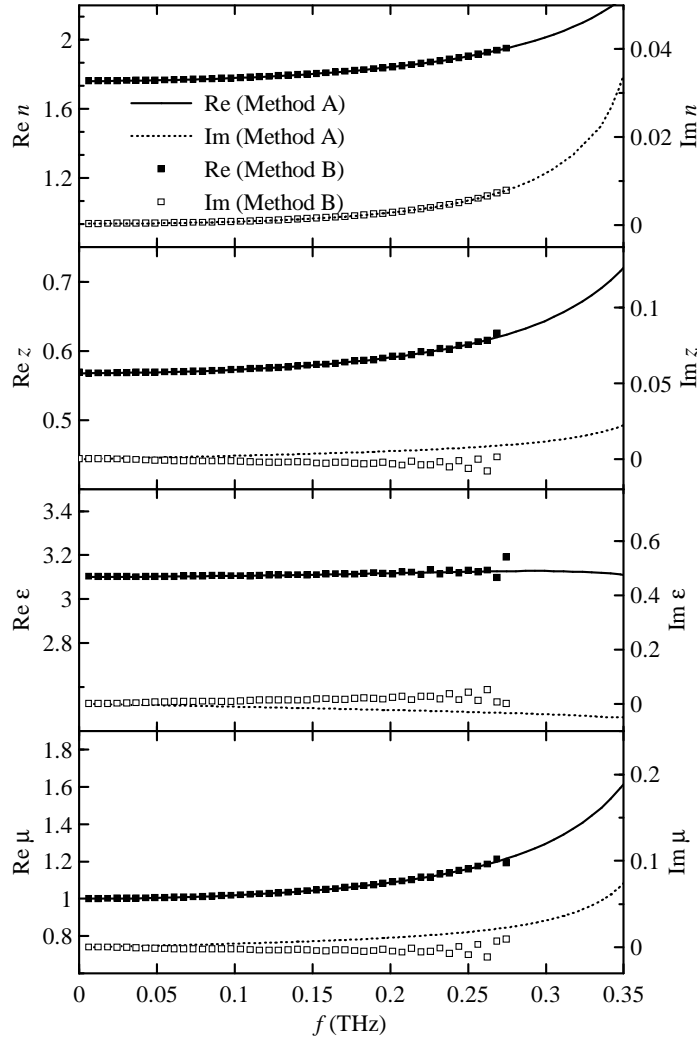
Figure 3.8: Refractive index n, wave impedance z, permittivity ε and permeability μ of the simulated metamaterial, determined by the methods A and B.

is similar to that presented in Ref. [177], where a structure consisting of an array of circular rods has been investigated.

The spectral range where the optical properties can be reliably determined is broader for the method A than for the method B: It is worth to compare the accuracy of both methods for our particular case of metamaterial. Concerning the method B, the errors $\Delta n/n$ and $\Delta z/z$ are controlled by the terms $\Delta T_0/T_0$ and $\Delta T_1/T_1$ (Eqs. (3.7) and (3.11)). The errors ΔT_0 and ΔT_1 contain at least the aliasing error, which arises from Fourier transformation of temporally windowed data. In our case, the aliasing error is of the order of $3 \cdot 10^{-3}$ (Fig. 3.7a). This error defines the lowest level of the transmittances T_0 and T_1

which can be obtained from the data. We remark that the transmittance T_1 is quite small at low frequencies, and it further decreases when the resonance is approached, attaining the error level for frequencies above 0.265 THz (see the kink in Fig. 3.7a followed by the characteristic ringing associated with the aliasing error). In turn, the transmittance T_1— and any derived optical properties—cannot be determined in this spectral range. The frequency range we access by the method A is broader. In this case, the absolute aliasing error is again of the order of $3 \cdot 10^{-3}$. However, the quantities $|R_0|$ and $|T_0|$ are considerably higher than $|T_1|$, thus the aliasing error level is reached at higher frequencies (~ 0.35 THz). The method A is thus applicable up to ~ 0.35 THz.

Note also the slight disagreement between values of Im z obtained by method A and B (Fig. 3.8). This can be understood from the fact that the position of the interface air/metamaterial is not unambiguously defined: Any amount of air before and after the first and last row of dielectric rods, respectively, can be regarded as a part of the meta-material.* In both cases, we considered the metamaterial exactly 256 periods long. The results of the method B are uniquely defined by this requirement. However, the choice of the air-layer thickness before the sample (d_1) influences the reflectivity, and subsequently mainly the wave impedance when the method A is employed. In the presented results, the air-layer thicknesses before and after the sample were the same ($d_1 = d_2$ in Fig. 3.6).

---

*The extent of the metamaterial does not result from physics: It is the task of the physicist to *define* what is the metamaterial and what is the surrounding medium. Different definitions of the limits of the metamaterial thus naturally result in different effective optical properties.

Part II

Photonic structures: From gratings to negative refraction

Chapter 4

Photonic structures and their fundamental properties

The articles of Yablonovitch [2] and John [178] in 1987 have given rise to a rapidly evolving field of electromagnetic band-gap structures. In fact, these works have initiated an unceasing progress in understanding and fabrication of artificial optical materials (metamaterials), which allow one to achieve desired optical properties by the structure design. In other words, these structures constitute an efficient way to the light flow control [179]. Unlike in the case of conventional materials, where the properties are determined by the atomic or molecular structure, the properties of metamaterials are fundamentally modified by their larger scale structure. For example, an array of purely dielectric rods with high permittivity dispersed in air exhibits a strong effective magnetic behavior (Ref. [177] and Sec. 3.4).

Though the phenomena observed in optical metamaterials are very rich and can be quite complex, the underlaying physics always consists in an electromagnetic problem of an inhomogeneous medium described by Maxwell's equations. In turn, many of the effects can be understood in terms of constructive and destructive interference of electromagnetic waves. However, quantitative results can be only rarely found in a close form, forcing the employment of numerical techniques. Most of them are applicable to several kinds of metamaterials. Numerical methods employed in this thesis are described in Chap. 5.

In this chapter, we only point out the principal characteristics and potential applications of two interesting kinds of optical metamaterials. Sec. 4.1 deals with photonic crystals (PCs). These are metamaterials with periodic variation of the permittivity, which may posses a forbidden photonic band where no propagative electromagnetic mode exists. Spatial confinement of a PC (see Fig. 4.1) leads to a so-called photonic crystal slab (PC slab) which is also discussed in this section. A special case of the PC slab—1D dielectric grating—is treated in detail in Chap. 6. In Sec. 4.2 we focus on the problem of left-handed media (LHM). These media exhibit spectral ranges where simultaneously $\varepsilon < 0$ and $\mu < 0$, causing a negative refraction of the incident beam. As classical materials
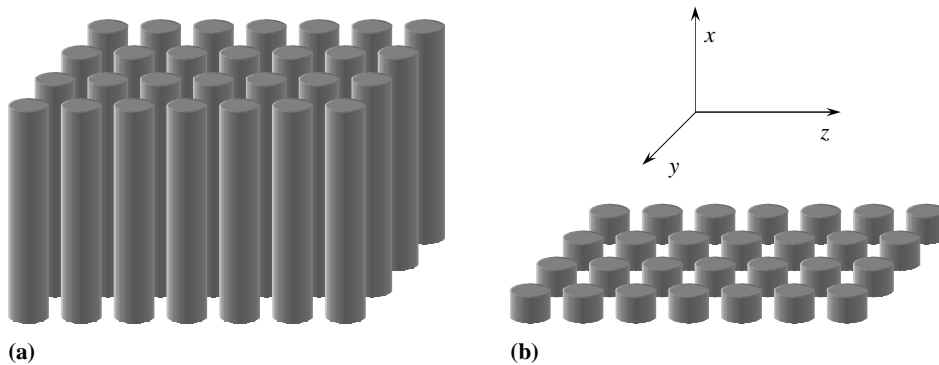
Figure 4.1: Difference between PC and PC slab, illustrated in the case of 2D structures. (a) The 2D PC is periodic in the yz plane (which typically contains the direction of propagation) while it is homogeneous and infinite along the x direction. (b) The 2D PC slab is also periodic in the yz plane. However, the structure is confined in the x direction.

with these properties are very unlikely to exist for higher frequencies, the metamaterial concepts is employed for their design and fabrication.

4.1   Photonic crystals and photonic crystal slabs

Waves propagating in PCs experience a periodic spatial variation of the permittivity, similarly as electrons in crystalline solids move in a periodic potential. In fact, there is a close analogy between photonic and solid crystals. In both cases, the wave functions are eigenmodes of a linear periodic operator (Tab. 4.1). Consequently, the Bloch's theorem applies, giving rise to electronic and photonic band structure, respectively. Also other terms, methods and results of the solid state physics can be often reused in the field of PCs.

Forbidden band is the key feature of PCs. It is a range of frequencies where no allowed electromagnetic states exist [180–182]. This means that incident electromagnetic modes with frequencies belonging to the forbidden band are reflected from the PC while no radiation passes through the PC [183, 184]. The vanishing photon density of states in the forbidden band also implies inhibition of spontaneous emission [2].

The origin of the forbidden band can be understood in a model situation, where a weak periodic perturbation is superposed on a constant refractive index* n (an analogy of the nearly-free-electron model). The dispersion relation of a homogeneous medium is simply

---

*Strictly speaking, the existence of the forbidden band in PCs is related to the periodicity of the dielectric permittivity as well as of the magnetic permeability. However, for frequencies above $\sim 100\,\text{GHz}$ magnetic excitations do not significantly contribute to magnetic permeability ($\mu = 1$) and we then refer to the periodicity of permittivity or refractive index only, according to the common practice.

Quantity	Electrons	Photons
Wave function	ψ	E
Periodic function	Potential $V(x)$	Permittivity $\varepsilon(x)$
Wave equation	Schrödinger's $\left(-\dfrac{\hbar^2}{2m}\dfrac{\partial^2}{\partial x^2} + \hat{V}(x)\right)\psi = E\psi$	Maxwell's $\dfrac{1}{\varepsilon(x)}\dfrac{\partial^2 E}{\partial x^2} = \dfrac{\omega^2}{c^2}E$
Length scale	Units of Å	Arbitrary

Table 4.1: Comparison between electrons in solid crystals and photons in photonic crystals. 1D systems are considered for clarity.

the light cone $\omega = c|k|/n$ (follow Fig. 4.2). In the presence of an infinitesimally small periodic perturbation of the refractive index, the light cone has to be mapped into a single Brillouin zone, leading to the degeneracy in the highly symmetric points (zone center and zone boundaries). As the strength of the perturbation increases, the degeneracy in these points is lifted and the dispersion curve splits, i.e. forbidden bands are created. This simple model also permits to estimate that the wavelength corresponding to the lowest forbidden band is comparable with the period of the PC.

If the periodicity of the PC is broken, e.g. by an insertion of a defect into otherwise periodic lattice, a so called defect mode—analogical to an impurity level in solid crystal—may be created inside the forbidden band. The defect mode appears in the spectra as a peak in the density of states, therefore it may result in a narrow peak in transmittance spectra. The defect mode is also characterized by a strong spatial field localization in the vicinity of the defect [183, 185–187]. This is very important for the possibility of enhancement of non-linear phenomena [188].
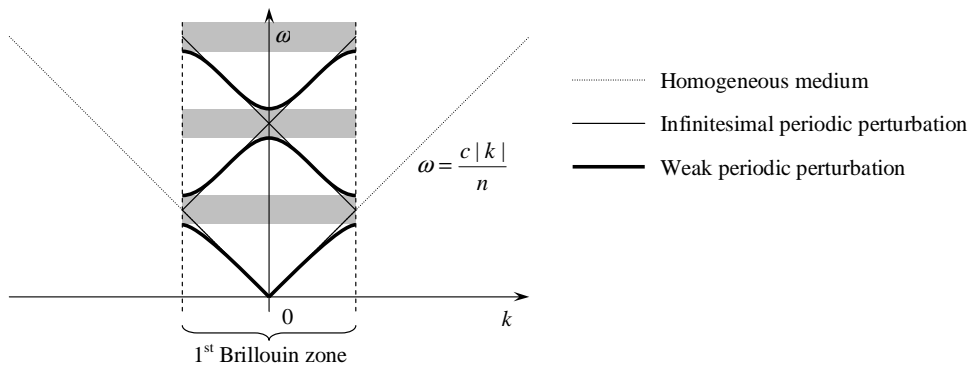
Figure 4.2: Illustration of the origin of the photonic forbidden band.

PCs comply to a scaling law [189] which has no equivalent in natural solid crystals. The scaling law means that increasing the length scale of a PC does not modify its band structure except the appropriate reduction of the wave-vector scale and frequency scale. This allows investigations of PCs with length scales suitable for construction and subsequent generalization of the results e.g. to the visible spectral range where the fabrication of PCs remains a challenging problem. Conversely, solid crystals do not obey the scaling law, as change in the length scale of the atomic lattice in a solid crystal leads to very complex changes of the electronic potential $\hat{V}$.

PC slabs resemble in many aspects to PCs. In particular, PC slabs exhibit a forbidden band for propagating waves if the incident beam travels along the direction of periodicity. Indeed, the forbidden band may be blue shifted due to the spatial confinement [190]. In reality, all PCs produced for experiments or applications are finite and thus more or less spatially confined; when the forbidden band is studied, one does not often distinguish between PC and PC slab. The remarkable difference between PCs and PC slabs consists in the existence of guided modes, similar to those in a planar waveguide [191]. The electromagnetic field of these modes is bounded to the slab (i.e. confined in the x direction in Fig. 4.1).

Applications

The unceasing miniaturization and increasing speed of electronic devices leads to higher power dissipation and to greater sensitivity to the synchronization of signal [192]. On the other hand, light can propagate nearly without losses in many dielectrics and it can carry a considerably larger amount of information. Consequently, there is a continuous demand to replace many of the electronic devices by optical technologies. As PCs and PC slabs can easily control the flow of the light, they are very perspective components in many fields including telecommunication and computing. Despite the great progress in the field of research in PCs, an all-optical chip is still to be constructed.

Active devices based on PCs are related to the control of the emission from PCs [2]. The inhibition or enhancement of spontaneous emission allows construction of lasers with very low threshold [189, 193–195]. Control of emission in PCs can provide highly-directive sources of spectrally narrow radiation as well [196–198]. Also an all-optical transistor based on a photonic band-gap material has been proposed [199].

The most straightforward passive device made of a PC is a spectral filter [200]. Such filters are often based on defect modes. Point defects act as microcavities [201, 202] while perfect mirrors based on planar defects may be fabricated [203, 204]. A great interest is devoted to line defects in PCs, which can act as waveguides. Such waveguides may include sharp bends [205–208], and they also allow designing of compact mode couplers [209]. Furthermore, PCs may exhibit the so-called superprism phenomenon, i.e. a wave propagation highly sensitive to the incident angle and wavelength [210]. This effect naturally permits design of ultrasmall signal demultiplexers [211, 212].

Concerning PC slabs, they have attracted considerable attention especially due to the possibility of optimization of quasi-phase matching for second-harmonic generation [213, 214]. They can also serve as a basis of efficient input/output couplers, splitters, filters or signal multiplexers [215–217].

Finally, we would like to point out that not all PCs are artificial materials. Notably the diffraction of X-rays on the crystal lattice is nothing else than a propagation of electromagnetic waves in periodically modulated media. Photonic lattices in the visible region can be found in nature as well. For example, photonic band gap is responsible for the blue iridescence in the butterfly *Morpho rhetenor*: Its wings are covered by discrete multilayers of cuticle and air, which act as highly-reflective PC [218, 219]. Multilayer structures also cause the observed color in several species of flora. In particular, let us name the fern-like tropical *Selaginella* [219].

4.2 Left-handed media

The roots of investigation of LHM (media with $\varepsilon < 0$ and $\mu < 0$) date back at least to the sixties, to the work of Veselago [3]. He suggested that many of the optical phenomena— including Doppler's and Čerenkov's effect—are reversed in LHM (see also the review [220]). One of the most remarkable phenomena is the Snell's law reversal, called also negative refraction.

Due to the lack of naturally available LHM, the Veselago's work fell into oblivion till the break of the millennium, when the metamaterial concept made it possible to design LHM [221] and examine experimentally its optical properties at least in the microwave range [168, 222]. The research in LHM has been further stimulated by the prediction of Pendry that LHM could be used to conceive a perfect lens. He claimed that such a lens would permit imaging with resolution beyond the diffraction limit which makes a principal restriction for the resolution achievable using positive-index lenses [167].

Negative refraction

First, we examine the propagation of electromagnetic waves in an isotropic homogeneous medium characterized by a relative dielectric permittivity ε and relative magnetic permeability μ. Let us suppose that the electric and magnetic fields are monochromatic plane waves with wave-vector $\boldsymbol{k}$, i.e. $\boldsymbol{E}, \boldsymbol{H} \propto \mathrm{e}^{\mathrm{i}(\omega t - \boldsymbol{k} \cdot \boldsymbol{r})}$. The Maxwell's *curl* equations yield the following relationship between the amplitudes of the vectors of electric and magnetic fields:

$$
\begin{aligned}
\boldsymbol{H} &= \frac{1}{\omega \mu_0 \mu} \boldsymbol{k} \times \boldsymbol{E} \\
\boldsymbol{E} &= -\frac{1}{\omega \varepsilon_0 \varepsilon} \boldsymbol{k} \times \boldsymbol{H}.
\end{aligned} \tag{4.1}
$$

The vectors $\boldsymbol{k}$, $\boldsymbol{E}$ and $\boldsymbol{H}$ form a right-handed set when $\varepsilon > 0$ and $\mu > 0$ while they form a left-handed set for $\varepsilon < 0$ and $\mu < 0$—hence the terms right-handed media (RHM) and left-handed media (LHM). These relations can be combined with Maxwell's *div* equations into the wave-equation

$$|\boldsymbol{k}|^2 \boldsymbol{E} = \tilde{n}^2 k_0^2 \cdot \boldsymbol{E}. \tag{4.2}$$

where $k_0 = \omega/c$ and $\tilde{n}^2 = \mu\varepsilon$. The medium supports propagating waves if $\tilde{n}^2 > 0$: This is the case of both RHM and LHM. However, only evanescent waves can exist in media with $\mathrm{sign}\,\varepsilon \neq \mathrm{sign}\,\mu$. The refractive index $\tilde{n}$ can be both positive as well as negative in both RHM and LHM; its sign then corresponds to waves traveling in opposite directions. Following the ideas of RHM, one can chose the direction of the wave vector $\boldsymbol{k}$, and subsequently work only with the positive refractive index $\tilde{n}$. However, a more pertinent approach consists in the characterization of waves in terms of the direction of the energy flux they carry. Inspection of the Poynting vector $\boldsymbol{S}$ shows that vectors $\boldsymbol{k}$ and $\boldsymbol{S}$ are opposite in LHM, in contrast to RHM where they follow the same direction:

$$\boldsymbol{S} = \boldsymbol{k} \cdot \frac{|\boldsymbol{E}|^2}{2\omega\mu_0\mu} = \boldsymbol{k} \cdot \frac{|\boldsymbol{H}|^2}{2\omega\varepsilon_0\varepsilon}. \tag{4.3}$$

Let us define the direction of the energy flux by the unit vector $\boldsymbol{s} = \boldsymbol{S}/|\boldsymbol{S}|$. Then:

$$\begin{aligned}
\boldsymbol{E}, \boldsymbol{H} &\propto \mathrm{e}^{\mathrm{i}(\omega t - \tilde{n} k_0\, \boldsymbol{s}\cdot\boldsymbol{r})} \quad \text{in RHM,} \\
\boldsymbol{E}, \boldsymbol{H} &\propto \mathrm{e}^{\mathrm{i}(\omega t + \tilde{n} k_0\, \boldsymbol{s}\cdot\boldsymbol{r})} \quad \text{in LHM,}
\end{aligned} \tag{4.4}$$

which can be unified by a definition of the refractive index n taking negative values in LHM:

$$n = \left\{ \begin{array}{ll} \tilde{n} & (\text{RHM}) \\ -\tilde{n} & (\text{LHM}) \end{array} \right. \rightarrow \mathrm{e}^{\mathrm{i}(\omega t - n k_0\, \boldsymbol{s}\cdot\boldsymbol{r})} \tag{4.5}$$

Using this definition of the refractive index, it is straightforward to show the validity of the Snell's law for refraction at an interface between media with refractive indices n_1 and n_2:

$$n_1 \sin\theta_1 = n_2 \sin\theta_2, \tag{4.6}$$

where θ_1 is the angle of incidence and θ_2 is the angle of refraction. It is thus clear that a negative refraction occurs at an interface between LHM and RHM.

The negative refraction itself allows a conception of a *planar* lens (Fig. 4.3). Moreover, it was realized by Pendry that such a lens is capable of focusing evanescent waves as well, making it possible to form a 2D image using all Fourier components of the field, including those connected to the object near field [167]. This would mean that the diffraction limit found in classical lenses could be overcome. Though this prediction as well as the existence of a LHM itself seemed to be quite controversial and provoked a brisk discussion, both ideas are nowadays generally accepted [223–232].
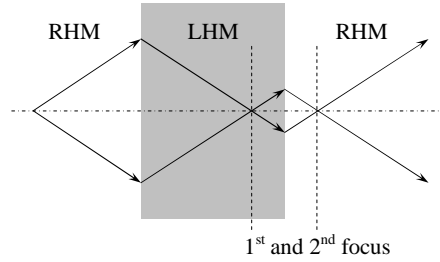
Figure 4.3: The beam at the interface between RHM and LHM is refracted at a negative angle with respect to the surface normal. Consequently, a planar LHM-slab embedded in a RHM may act as a lens.

Left-handed metamaterials

Majority of natural materials is characterized by positive ε and μ. A strongly negative dielectric permittivity can be found in metals bellow the plasma frequency; a weakly negative effective ε is exhibited by an array of thin metallic wires (diluted metal) below a renormalized plasma frequency [233, 234]. But what about LHM? The key point is to find a medium with negative magnetic permeability [235]. Indeed, a mixture of such a material e.g. with the diluted metal ($\varepsilon < 0$) may behave as an effective LHM, according to the effective medium theory in the static limit.

An effective magnetic resonance accompanied by a spectral range where $\mu < 0$ can be observed in metallic split-ring resonators, as recently predicted Pendry et al. [4]. In order to achieve simultaneously $\varepsilon < 0$, these resonators can be embedded in an array of thin metallic wires [221]. Such a metamaterial has been extensively experimentally and theoretically investigated to verify the predictions like negative refraction and negative phase velocity [168, 169, 236–241].

Another kind of metamaterial exhibiting an effective magnetic resonance is an array of particles with high dielectric permittivity. These particles (dielectric rods or dielectric spheres) may exhibit Mie's resonances which are responsible for the effective magnetic behavior [177, 242]. The effective magnetic response can be also understood in terms of effective medium theory in the quasi-static limit [243].

The negative refraction is not necessarily associated only with LHM. For example, negative refraction occurs in PCs too [244–247]. As the dimensions of unit cell of PC are comparable to the radiation wavelength, one cannot describe such a structure using effective material parameters.

Finally, it should be pointed out that majority of the investigated left-handed metamaterials or negative-permeability metamaterials are periodic arrays. In turn, many of the numerical methods developed for investigation of PCs can be also used for the studies on left-handed metamaterials. For example, this is the case of the metamaterial examined in Sec. 3.4.

Chapter 5

Calculations of the optical properties of photonic structures

As we have already stated in Chap. 4, the calculations of properties of 2D and 3D photonic structures mostly rely on numerical simulations. The numerical methods employed in this thesis are reviewed in this chapter. For this purpose, we first formulate the electromagnetic problem to be solved (Sec. 5.1). The rest of the chapter is devoted to the description of individual numerical methods. Plane wave expansion method, which was one of the first methods employed for numerical simulations of multi-dimensional photonic crystals (PCs), is treated in Sec. 5.2. In Sec. 5.3, transfer matrix method (TMM) is discussed in detail. Based on this method, a computer code has been developed in the framework of this thesis, which was then applied to numerical simulations of structures described in subsequent chapters and also to that discussed in Sec. 3.4.

5.1 Description of photonic structures

Here we sum up the basic assumptions and equations which are related to the electromagnetic problem under investigation. We restrict ourselves to structures composed of isotropic materials exhibiting a linear dielectric and magnetic response. We also assume that there are no free carriers and no conduction. The Maxwell's equations in such a situation read

$$\left.\begin{aligned}
\nabla \times \boldsymbol{E}(\boldsymbol{r},t) &= -\mu_0 \frac{\partial}{\partial t}[\mu(\boldsymbol{r})\boldsymbol{H}(\boldsymbol{r},t)] \\
\nabla \times \boldsymbol{H}(\boldsymbol{r},t) &= \varepsilon_0 \frac{\partial}{\partial t}[\varepsilon(\boldsymbol{r})\boldsymbol{E}(\boldsymbol{r},t)] \\
\nabla \cdot [\varepsilon(\boldsymbol{r})\boldsymbol{E}(\boldsymbol{r},t)] &= 0 \\
\nabla \cdot [\mu(\boldsymbol{r})\boldsymbol{H}(\boldsymbol{r},t)] &= 0,
\end{aligned}\right\} \qquad (5.1)$$

where $\varepsilon(\boldsymbol{r})$ and $\mu(\boldsymbol{r})$ represent the relative dielectric permittivity and relative magnetic permeability, respectively.

All methods treated in this chapter deal with spectral components of the electromagnetic field rather than with its temporal profile. The spectral decomposition is assumed in the form $\boldsymbol{F}(\boldsymbol{r},t) \mapsto \boldsymbol{F}(\boldsymbol{r},\omega)\exp(-\mathrm{i}\omega t)$, where the vector $\boldsymbol{F} = \{\boldsymbol{E},\boldsymbol{H}\}$ represents the entire electromagnetic field. Eqs. (5.1) are thus transformed into the following set:

$$
\begin{aligned}
\nabla \times \boldsymbol{E}(\boldsymbol{r},\omega) &= \mathrm{i}\omega\mu_0\mu(\boldsymbol{r},\omega)\boldsymbol{H}(\boldsymbol{r},\omega) \\
\nabla \times \boldsymbol{H}(\boldsymbol{r},\omega) &= -\mathrm{i}\omega\varepsilon_0\varepsilon(\boldsymbol{r},\omega)\boldsymbol{E}(\boldsymbol{r},\omega) \\
\nabla \cdot [\varepsilon(\boldsymbol{r},\omega)\boldsymbol{E}(\boldsymbol{r},\omega)] &= 0 \\
\nabla \cdot [\mu(\boldsymbol{r},\omega)\boldsymbol{H}(\boldsymbol{r},\omega)] &= 0.
\end{aligned}
\tag{5.2}
$$

The ω-dependence of the fields and of the response functions ε and μ will not be explicitly marked in the rest of the chapter in order to preserve graphical clarity.

The full definition of the electromagnetic problem also requires specification of boundary conditions. As each method may use slightly different boundary conditions, their formulation will be discussed separately in the context of each method.

5.2   Plane wave expansion method

The plane wave expansion method is the most straightforward approach for calculating photonic band-structure of PCs [181, 248]. Indeed, the perfect periodicity allows application of the Bloch's theorem to the set of Eqs. (5.2). The spatial dependence of the electromagnetic field can be separated into components

$$
\boldsymbol{F}(\boldsymbol{r}) \mapsto \boldsymbol{F_k}(\boldsymbol{r})\exp(\mathrm{i}\boldsymbol{k}\cdot\boldsymbol{r}),
\tag{5.3}
$$

where the wave-vector $\boldsymbol{k}$ belongs to the first Brillouin zone and $\boldsymbol{F_k}(\boldsymbol{r})$ is a periodic function with the same periodicity as the investigated PC. Consequently, the field $\boldsymbol{F_k}$ can be expanded into the plane wave basis:

$$
\boldsymbol{F_k}(\boldsymbol{r}) = \sum_{\boldsymbol{G}} \boldsymbol{F_{kG}}\exp(\mathrm{i}\boldsymbol{G}\cdot\boldsymbol{r}).
\tag{5.4}
$$

The sum runs over all reciprocal-lattice vectors $\boldsymbol{G}$. Substitution of this expression into Eqs. (5.2) and elimination of $\boldsymbol{E}$ yields the following eigenvalue equation:

$$
\sum_{\boldsymbol{G'}} \xi_{\boldsymbol{G}-\boldsymbol{G'}}(\boldsymbol{k}+\boldsymbol{G}) \times [(\boldsymbol{k}+\boldsymbol{G'}) \times \boldsymbol{H_{kG'}}] = -\frac{\omega_n^2(\boldsymbol{k})}{c^2}\boldsymbol{H_{kG}}.
\tag{5.5}
$$

The index n labels the different bands of the dispersion relation $\omega(\boldsymbol{k})$ for a given wave-vector $\boldsymbol{k}$. The Fourier components $\xi_{\boldsymbol{G}}$ of the reciprocal permittivity are defined as

$$\xi_{\boldsymbol{G}} = \frac{1}{V} \int \frac{\mathrm{e}^{-\mathrm{i}\boldsymbol{G}\boldsymbol{r}}}{\varepsilon(\boldsymbol{r})} \, \mathrm{d}^3\boldsymbol{r} \tag{5.6}$$

where the integration runs over the volume V of the elementary cell. For the sake of simplicity, a possible magnetic response of the constituents is neglected in Eq. (5.5) ($\mu \equiv 1$). The magnetic field $\boldsymbol{H}$ is thus transversal and the vectors $\boldsymbol{H}_{\boldsymbol{kG}}$ can be expressed as a linear combination of two vectors orthogonal to $\boldsymbol{k} + \boldsymbol{G}$.

Eq. (5.5) represents an eigenvalue problem. As it is usually solved numerically, the infinite matrix needs to be truncated. Let's suppose that we take into account N plane waves ($N = N_x N_y N_z$)—or equivalently, N reciprocal vectors $\boldsymbol{G}$ (N_x is the number of points in the reciprocal lattice in the x-direction etc.). The computational time then grows as $O((N_x N_y N_z)^3)$ for each wave-vector $\boldsymbol{k}$, as the matrix to be diagonalized has the dimensions $2N \times 2N$ [249]. The time required for the simulation may make it hard to achieve a good convergence for 3D structures. In particular, simulations of structures with large or rapid variation of the dielectric permittivity are especially time-consuming because a large number of Fourier components $\xi_{\boldsymbol{G}}$ has to be taken into account.

Investigation of defect modes using plane wave expansion method is also possible by employing a super-cell technique [186]. However, large super-cells are required to minimize the coupling between neighboring defects. Consequently, a large number of plane waves has to be used, leading to enormous computational times.

5.3 Transfer matrix method

The TMM allows calculation of optical properties of PCs as well as calculation of photonic band structures [250–252]. This method is also notably faster than plane wave expansion method.

In this section we first recall the TMM in 1 dimension: This is a well-known technique useful for analytical and numerical calculations of transmittances and reflectances of multi-layered stacks and 1D PCs [253, 254]. After that, we describe a multi-dimensional version of this method developed by Pendry et al. [250–252], which is suitable for simulations of 2D and 3D PCs.

Transfer matrix method in 1 dimension

In 1D TMM, the electric and magnetic fields at opposite sides of the stack are linked via a transfer matrix $\mathbf{T}$ (Fig. 5.1a):

$$\begin{pmatrix} \boldsymbol{E}_0 \\ \boldsymbol{H}_0 \end{pmatrix} = \mathbf{T} \cdot \begin{pmatrix} \boldsymbol{E}_k \\ \boldsymbol{H}_k \end{pmatrix}. \tag{5.7}$$
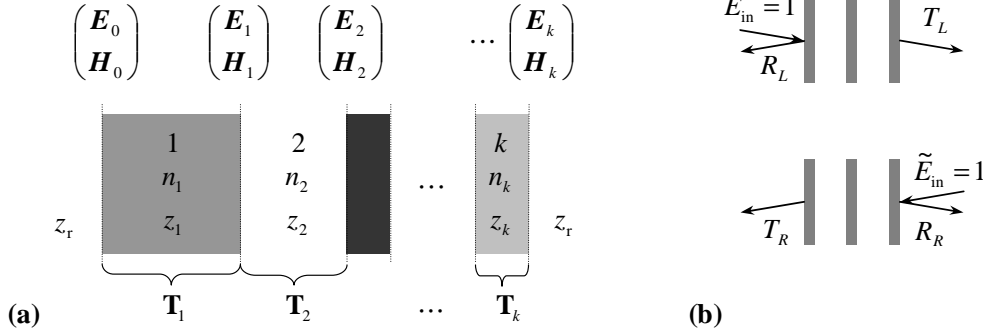
Figure 5.1: (a) Schematic of 1D TMM and its parameters n_j and z_j. (b) Definition of transmittances and reflectances of a stack of homogeneous layers. Note that these quantities can be defined for an incidence from both left- and right-hand side of the stack.

This transfer matrix can be expressed as a product of transfer matrices $\mathbf{T}_j$ corresponding to the constituting homogeneous layers:

$$\mathbf{T} = \mathbf{T}_1 \cdot \mathbf{T}_2 \cdot \cdots \cdot \mathbf{T}_k, \tag{5.8}$$

where each matrix $\mathbf{T}_j$ links the fields at the surfaces of these layers:

$$\begin{pmatrix} \boldsymbol{E}_{j-1} \\ \boldsymbol{H}_{j-1} \end{pmatrix} = \mathbf{T}_j \cdot \begin{pmatrix} \boldsymbol{E}_j \\ \boldsymbol{H}_j \end{pmatrix}. \tag{5.9}$$

For the sake of simplicity we consider only the case of normal incidence. Propagation along the z axis can be thus described using a single component of electric and magnetic field (e.g. E_x and H_y), and the size of transfer matrices reduces to 2×2. Note also, that the tangential components of the fields $\boldsymbol{E}$ and $\boldsymbol{H}$ are continuous across the interface. In turn, we do not need to take care whether the fields $E_{x,j}$ and $H_{y,j}$ are determined just before or just after the interface between the layers.

The transfer matrix $\mathbf{T}_j$ of a homogeneous layer can be simply derived from Eqs. (5.2):

$$\mathbf{T}_j = \begin{pmatrix} T_{j,11} & T_{j,12} \\ T_{j,21} & T_{j,22} \end{pmatrix} = \begin{pmatrix} \cos k_j d_j & \mathrm{i} z_0 z_j \sin k_j d_j \\ \frac{\mathrm{i}}{z_0 z_j} \sin k_j d_j & \cos k_j d_j \end{pmatrix}, \tag{5.10}$$

where $k_j = \omega n_j / c$ is a wave-vector, d_j is the layer thickness, z_j and n_j are its relative wave-impedance and refractive index, respectively, and $z_0 = \sqrt{\mu_0/\varepsilon_0}$ is the wave-impedance of vacuum.

The transmittance and reflectance of the structure can be expressed by decomposing the electromagnetic field into waves propagating left and right. When the incident wave

irradiates the left surface of the structure (Fig. 5.1b top), the field transmittance T_L and reflectance R_L read:

$$
\begin{aligned}
T_L &= \frac{2}{T_{11} + T_{22} + \frac{T_{12}}{z_r z_0} + z_r z_0 T_{21}} \\
R_L &= \frac{T_{11} - T_{22} + \frac{T_{12}}{z_r z_0} - z_r z_0 T_{21}}{T_{11} + T_{22} + \frac{T_{12}}{z_r z_0} + z_r z_0 T_{21}},
\end{aligned}
\tag{5.11}
$$

where z_r stands for the relative wave-impedance of the medium which surrounds the structure. When the incident wave impinges on the structure from the right (Fig. 5.1b bottom), the corresponding transmittance T_R and reflectance R_R can be written as

$$
\begin{aligned}
T_R &= \frac{2}{T_{11} + T_{22} + \frac{T_{12}}{z_r z_0} + z_r z_0 T_{21}} \quad (= T_L) \\
R_R &= -\frac{T_{11} - T_{22} - \frac{T_{12}}{z_r z_0} + z_r z_0 T_{21}}{T_{11} + T_{22} + \frac{T_{12}}{z_r z_0} + z_r z_0 T_{21}}.
\end{aligned}
\tag{5.12}
$$

The formulae (5.8), (5.10), (5.11) and (5.12) thus constitute a straightforward recipe how to calculate the transmittance and reflectance spectra of a multilayered stack, providing the structural parameters of the layers (thickness, wave impedance and refractive index) are known. Note that $T_R^2 + R_R^2 = T_L^2 + R_L^2 = 1$ in absence of losses.

Transfer matrix method in 2 and 3 dimensions

The basic idea of multi-dimensional TMM strongly resembles to the 1D TMM. A transfer matrix links electric and magnetic fields at both ends of the investigated structure (Fig. 5.2). However, in the general case the structure is assumed to be inhomogeneous along x, y and z so that the fields show a spatial distribution in the xy-plane.

The fields in planes $z = 0$ and $z = L_z$ can be linked using the integral relation

$$
\boldsymbol{F}(x, y, L_z) = \iint \mathbf{T}_{L_z,0}(x, y | x', y') \cdot \boldsymbol{F}(x', y', 0) \, \mathrm{d}x' \mathrm{d}y',
\tag{5.13}
$$

where the vector $\boldsymbol{F} = \{E_x, E_y, E_z, H_x, H_y, H_z\}$ represents the electromagnetic field and $\mathbf{T}_{L_z,0}(x, y | x', y')$ stands for a transfer operator between planes $z = 0$ and $z = L_z$. Analogically as in the case of 1D TMM, the entire structure can be regarded as a multi-layer stack of inhomogeneous slices. The transfer operator $\mathbf{T}_{L_z,0}$ can be expressed as a composition of operators $\mathbf{T}_{z_j,z_{j-1}}$ corresponding to these slices. For example,

$$
\mathbf{T}_{z_2,0}(x_2, y_2 | x_0, y_0) = \iint \mathbf{T}_{z_2,z_1}(x_2, y_2 | x_1, y_1) \cdot \mathbf{T}_{z_1,0}(x_1, y_1 | x_0, y_0) \, \mathrm{d}x_1 \mathrm{d}y_1.
\tag{5.14}
$$

For numerical purposes, it is necessary to find a discrete version of these operators.
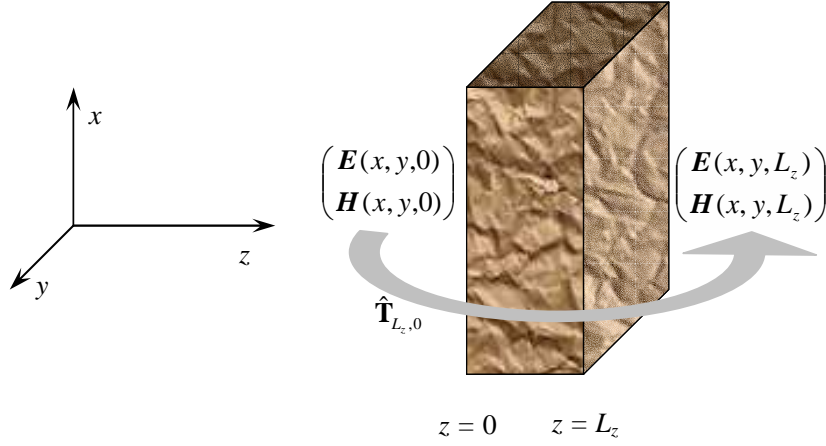
Figure 5.2: Scheme of the TMM in 3D. The transfer matrix $\mathbf{T}_{L_z,0}$ relates the field distributions in planes $z = 0$ and $z = L_z$.

According to the original approach [250], we assume the xyz space to be discretized by an equidistant rectangular mesh of points. The number of mesh points along the x-, y- and z-direction is denoted as N_x, N_y and N_z, respectively, and the corresponding spacing between the mesh points is $\Delta x = L_x/N_x$, $\Delta y = L_y/N_y$ and $\Delta z = L_z/N_z$ respectively. The Maxwell's *curl* equations (5.2) are discretized by approximating the $\nabla \times \boldsymbol{E}$ term by forward differences and by approximating the $\nabla \times \boldsymbol{H}$ term by backward differencies:

$$
\left.
\begin{aligned}
-\mathrm{i}\omega\varepsilon_0\varepsilon(\boldsymbol{r})E_x(\boldsymbol{r}) &= \frac{H_z(\boldsymbol{r}) - H_z(\boldsymbol{r} - \Delta\boldsymbol{y})}{\Delta y} - \frac{H_y(\boldsymbol{r}) - H_y(\boldsymbol{r} - \Delta\boldsymbol{z})}{\Delta z} \\
-\mathrm{i}\omega\varepsilon_0\varepsilon(\boldsymbol{r})E_y(\boldsymbol{r}) &= \frac{H_x(\boldsymbol{r}) - H_x(\boldsymbol{r} - \Delta\boldsymbol{z})}{\Delta z} - \frac{H_z(\boldsymbol{r}) - H_z(\boldsymbol{r} - \Delta\boldsymbol{x})}{\Delta x} \\
-\mathrm{i}\omega\varepsilon_0\varepsilon(\boldsymbol{r})E_z(\boldsymbol{r}) &= \frac{H_y(\boldsymbol{r}) - H_y(\boldsymbol{r} - \Delta\boldsymbol{x})}{\Delta x} - \frac{H_x(\boldsymbol{r}) - H_x(\boldsymbol{r} - \Delta\boldsymbol{y})}{\Delta y} \\
\mathrm{i}\omega\mu_0\mu(\boldsymbol{r})H_x(\boldsymbol{r}) &= \frac{E_z(\boldsymbol{r} + \Delta\boldsymbol{y}) - E_z(\boldsymbol{r})}{\Delta y} - \frac{E_y(\boldsymbol{r} + \Delta\boldsymbol{z}) - E_y(\boldsymbol{r})}{\Delta z} \\
\mathrm{i}\omega\mu_0\mu(\boldsymbol{r})H_y(\boldsymbol{r}) &= \frac{E_x(\boldsymbol{r} + \Delta\boldsymbol{z}) - E_x(\boldsymbol{r})}{\Delta z} - \frac{E_z(\boldsymbol{r} + \Delta\boldsymbol{x}) - E_z(\boldsymbol{r})}{\Delta x} \\
\mathrm{i}\omega\mu_0\mu(\boldsymbol{r})H_z(\boldsymbol{r}) &= \frac{E_y(\boldsymbol{r} + \Delta\boldsymbol{x}) - E_y(\boldsymbol{r})}{\Delta x} - \frac{E_x(\boldsymbol{r} + \Delta\boldsymbol{y}) - E_x(\boldsymbol{r})}{\Delta y}
\end{aligned}
\right\} \quad (5.15)
$$

Two functions can be eliminated from this system: It is suitable to eliminate $E_z(\boldsymbol{r})$ and $H_z(\boldsymbol{r})$. The remaining components (E_x, E_y, H_x and H_y) are continuous across the interfaces between individual slices, so it is not necessary to take care whether they are

measured just before or just after the interface. We obtain [250]:

$$
\frac{E_x(\boldsymbol{r}+\Delta\boldsymbol{z})-E_x(\boldsymbol{r})}{\Delta z} = -\mathrm{i}\omega\mu_0\mu(\boldsymbol{r})H_y(\boldsymbol{r}) +
$$
$$
+ \frac{\dfrac{H_y(\boldsymbol{r}+\Delta\boldsymbol{x})-H_y(\boldsymbol{r})}{\Delta x} - \dfrac{H_x(\boldsymbol{r}+\Delta\boldsymbol{x})-H_x(\boldsymbol{r}+\Delta\boldsymbol{x}-\Delta\boldsymbol{y})}{\Delta y}}{\mathrm{i}\omega\varepsilon_0\varepsilon(\boldsymbol{r}+\Delta\boldsymbol{x})\cdot\Delta x} -
$$
$$
- \frac{\dfrac{H_y(\boldsymbol{r})-H_y(\boldsymbol{r}-\Delta\boldsymbol{x})}{\Delta x} - \dfrac{H_x(\boldsymbol{r})-H_x(\boldsymbol{r}-\Delta\boldsymbol{y})}{\Delta y}}{\mathrm{i}\omega\varepsilon_0\varepsilon(\boldsymbol{r})\cdot\Delta x}
\tag{5.16}
$$

$$
\frac{E_y(\boldsymbol{r}+\Delta\boldsymbol{z})-E_y(\boldsymbol{r})}{\Delta z} = +\mathrm{i}\omega\mu_0\mu(\boldsymbol{r})H_x(\boldsymbol{r}) +
$$
$$
+ \frac{\dfrac{H_y(\boldsymbol{r}+\Delta\boldsymbol{y})-H_y(\boldsymbol{r}-\Delta\boldsymbol{x}+\Delta\boldsymbol{y})}{\Delta x} - \dfrac{H_x(\boldsymbol{r}+\Delta\boldsymbol{y})-H_x(\boldsymbol{r})}{\Delta y}}{\mathrm{i}\omega\varepsilon_0\varepsilon(\boldsymbol{r}+\Delta\boldsymbol{y})\cdot\Delta y} -
$$
$$
- \frac{\dfrac{H_y(\boldsymbol{r})-H_y(\boldsymbol{r}-\Delta\boldsymbol{x})}{\Delta x} - \dfrac{H_x(\boldsymbol{r})-H_x(\boldsymbol{r}-\Delta\boldsymbol{y})}{\Delta y}}{\mathrm{i}\omega\varepsilon_0\varepsilon(\boldsymbol{r})\cdot\Delta y}
\tag{5.17}
$$

$$
\frac{H_x(\boldsymbol{r}+\Delta\boldsymbol{z})-H_x(\boldsymbol{r})}{\Delta z} = +\mathrm{i}\omega\varepsilon_0\varepsilon(\boldsymbol{r}+\Delta\boldsymbol{z})E_y(\boldsymbol{r}+\Delta\boldsymbol{z}) +
$$
$$
+ \frac{\dfrac{E_x(\boldsymbol{r}+\Delta\boldsymbol{y}+\Delta\boldsymbol{z})-E_x(\boldsymbol{r}+\Delta\boldsymbol{z})}{\Delta y} - \dfrac{E_y(\boldsymbol{r}+\Delta\boldsymbol{x}+\Delta\boldsymbol{z})-E_y(\boldsymbol{r}+\Delta\boldsymbol{z})}{\Delta x}}{\mathrm{i}\omega\mu_0\mu(\boldsymbol{r}+\Delta\boldsymbol{z})\cdot\Delta x} -
$$
$$
- \frac{\dfrac{E_x(\boldsymbol{r}-\Delta\boldsymbol{x}+\Delta\boldsymbol{y}+\Delta\boldsymbol{z})-E_x(\boldsymbol{r}-\Delta\boldsymbol{x}+\Delta\boldsymbol{z})}{\Delta y} - \dfrac{E_y(\boldsymbol{r}+\Delta\boldsymbol{z})-E_y(\boldsymbol{r}-\Delta\boldsymbol{x}+\Delta\boldsymbol{z})}{\Delta x}}{\mathrm{i}\omega\mu_0\mu(\boldsymbol{r}-\Delta\boldsymbol{x}+\Delta\boldsymbol{z})\cdot\Delta x}
\tag{5.18}
$$

$$
\frac{H_y(\boldsymbol{r}+\Delta\boldsymbol{z})-H_y(\boldsymbol{r})}{\Delta z} = -\mathrm{i}\omega\varepsilon_0\varepsilon(\boldsymbol{r}+\Delta\boldsymbol{z})E_x(\boldsymbol{r}+\Delta\boldsymbol{z}) +
$$
$$
+ \frac{\dfrac{E_x(\boldsymbol{r}+\Delta\boldsymbol{y}+\Delta\boldsymbol{z})-E_x(\boldsymbol{r}+\Delta\boldsymbol{z})}{\Delta y} - \dfrac{E_y(\boldsymbol{r}+\Delta\boldsymbol{x}+\Delta\boldsymbol{z})-E_y(\boldsymbol{r}+\Delta\boldsymbol{z})}{\Delta x}}{\mathrm{i}\omega\mu_0\mu(\boldsymbol{r}+\Delta\boldsymbol{z})\cdot\Delta y} -
$$
$$
- \frac{\dfrac{E_x(\boldsymbol{r}+\Delta\boldsymbol{z})-E_x(\boldsymbol{r}-\Delta\boldsymbol{y}+\Delta\boldsymbol{z})}{\Delta y} - \dfrac{E_y(\boldsymbol{r}+\Delta\boldsymbol{x}-\Delta\boldsymbol{y}+\Delta\boldsymbol{z})-E_y(\boldsymbol{r}-\Delta\boldsymbol{y}+\Delta\boldsymbol{z})}{\Delta x}}{\mathrm{i}\omega\mu_0\mu(\boldsymbol{r}-\Delta\boldsymbol{y}+\Delta\boldsymbol{z})\cdot\Delta y}
\tag{5.19}
$$

These equations allow calculation of the electromagnetic field distribution in the plane $z + \Delta z$ providing it is known in the plane z. It is convenient to introduce a transfer matrix $\mathbf{T}_{z+\Delta z,z}$ linking the field distributions in planes z and $z + \Delta z$:

$$\tilde{\boldsymbol{F}}(z + \Delta z) = \mathbf{T}_{z+\Delta z,z} \cdot \tilde{\boldsymbol{F}}(z). \qquad (5.20)$$

where $\tilde{\boldsymbol{F}}$ represents the E_x, E_y, H_x and H_y components of the electromagnetic field on the discrete mesh in the xy plane (this vector contains $4N_x N_y$ components). Due to the sparseness of the matrices $\mathbf{T}_{z+\Delta z,z}$ defined by Eqs. (5.16)–(5.19), the propagation along the entire structure takes only $O(N_x N_y N_z)$ operations.

Eq. (5.20) must be accompanied by appropriate boundary conditions. Here we consider an infinite periodic structure filling the space along the x and y directions, the periods being L_x and L_y respectively. As the Bloch's theorem applies along these directions, the fields at the elementary cell boundaries are subject to conditions $\tilde{\boldsymbol{F}}(x + L_x, y, z) = \mathrm{e}^{\mathrm{i}k_x L_x} \tilde{\boldsymbol{F}}(x, y, z)$ and $\tilde{\boldsymbol{F}}(x, y + L_y, z) = \mathrm{e}^{\mathrm{i}k_y L_y} \tilde{\boldsymbol{F}}(x, y, z)$. Consequently, it is sufficient to deal with fields inside a single cell in the xy plane.

Concerning the z-direction, there are two important situations, depending on what result we want to obtain from the simulation. In order to calculate the band structure, it is convenient to assume that the structure is infinite and periodic with period L_z. In turn, the fields along the z direction are subject to the Bloch condition

$$\tilde{\boldsymbol{F}}(L_z) = \mathbf{T}_{L_z,0} \cdot \tilde{\boldsymbol{F}}(0) = \mathrm{e}^{\mathrm{i}k_z L_z} \tilde{\boldsymbol{F}}(0). \qquad (5.21)$$

Obviously, the eigenvalues of the transfer matrix $\mathbf{T}_{L_z,0}$ for a *single* period define a set of values $\mathrm{e}^{\mathrm{i}k_z L_z}$. It is thus possible to calculate k_z as a function of parameters ω, k_x and k_y which defines the dispersion curves of the band-structure $\omega(\boldsymbol{k})$. The most time-consuming step consists in the diagonalization of the matrix $\mathbf{T}_{L_z,0}$ which requires $O((N_x N_y)^3)$ operations.

Calculation of transmittance and reflectance spectra requires employment of a slightly different procedure. The real-space representation of the transfer matrix $\mathbf{T}_{L_z,0}$ (defined by Eqs. (5.16)–(5.19)) has to be transformed into the plane wave basis. This basis (denoted as $\tilde{\boldsymbol{F}}^{\mathrm{vac}}$) can be constructed e.g. from the eigenvectors of transfer matrix $\mathbf{T}_{z+\Delta z,z}^{\mathrm{vac}}$ describing a slice of vacuum. The vectors of this basis can be written in the form

$$\boldsymbol{F}^{\mathrm{vac}}(x, y, z) = \boldsymbol{F}^{\mathrm{vac}} \exp\left[\mathrm{i}(k_x + G_x)x + \mathrm{i}(k_y + G_y)y + \mathrm{i}k_z z\right], \qquad (5.22)$$

where G_x and G_y are reciprocal lattice vectors. By substituting this expression into Eqs. (5.15) we obtain the relation between the vectors $\boldsymbol{E}^{\mathrm{vac}}$ and $\boldsymbol{H}^{\mathrm{vac}}$:

$$\begin{aligned}
\boldsymbol{\kappa}^E \times \boldsymbol{E}^{\mathrm{vac}} &= \omega \mu_0 \boldsymbol{H}^{\mathrm{vac}} \\
\boldsymbol{\kappa}^H \times \boldsymbol{H}^{\mathrm{vac}} &= -\omega \varepsilon_0 \boldsymbol{E}^{\mathrm{vac}}
\end{aligned} \qquad (5.23)$$

where

$$
\begin{aligned}
\boldsymbol{\kappa}^E &= \left[\frac{\mathrm{e}^{\mathrm{i}(k_x+G_x)\Delta x} - 1}{\Delta x}, \frac{\mathrm{e}^{\mathrm{i}(k_y+G_y)\Delta y} - 1}{\Delta y}, \frac{\mathrm{e}^{\mathrm{i}k_z\Delta z} - 1}{\Delta z} \right] \\
\boldsymbol{\kappa}^H &= \left[\frac{1 - \mathrm{e}^{-\mathrm{i}(k_x+G_x)\Delta x}}{\Delta x}, \frac{1 - \mathrm{e}^{-\mathrm{i}(k_y+G_y)\Delta y}}{\Delta y}, \frac{1 - \mathrm{e}^{-\mathrm{i}k_z\Delta z}}{\Delta z} \right].
\end{aligned}
\tag{5.24}
$$

Only transversal modes (satisfying the Maxwell's *div* equations) are used for the construction of the plane wave basis. The longitudinal modes are thus automatically eliminated in subsequent calculations.

Combination of Eqs. (5.23) provides the following dispersion relation:

$$
\frac{\omega^2}{c^2} = \left(\frac{2\sin\frac{(k_x+G_x)\Delta x}{2}}{\Delta x} \right)^2 + \left(\frac{2\sin\frac{(k_y+G_y)\Delta y}{2}}{\Delta y} \right)^2 + \left(\frac{2\sin\frac{k_z\Delta z}{2}}{\Delta z} \right)^2
\tag{5.25}
$$

which is important for the construction of the basis (k_z as a function of other parameters has to be calculated). Note that this expression coincides with the dispersion relation $\omega^2/c^2 = (k_x+G_x)^2 + (k_y+G_y)^2 + k_z^2$ obtained from *exact* Maxwell's equations in the limit $\Delta x, \Delta y, \Delta z \to 0$.

Let us label the j-th vector of the plane wave basis as $\tilde{\boldsymbol{F}}_j^{\mathrm{vac}}$ (the index j includes reciprocal lattice vectors G_x and G_y along with the polarization state). The transfer matrix $\mathbf{T}_{z+\Delta z,z}^{\mathrm{vac}}$ describing a slice of vacuum is diagonal in this basis:

$$
\bar{\mathbf{T}}_{z+\Delta z,z}^{\mathrm{vac}} = \begin{pmatrix}
\mathrm{e}^{\mathrm{i}k_{z,1}^{\mathrm{vac}}\Delta z} & & & & & \\
& \mathrm{e}^{\mathrm{i}k_{z,2}^{\mathrm{vac}}\Delta z} & & & \bigcirc & \\
& & \ddots & & & \\
& & & \mathrm{e}^{-\mathrm{i}k_{z,1}^{\mathrm{vac}}\Delta z} & & \\
& \bigcirc & & & \mathrm{e}^{-\mathrm{i}k_{z,2}^{\mathrm{vac}}\Delta z} & \\
& & & & & \ddots
\end{pmatrix}
\tag{5.26}
$$

The eigenvalues $\mathrm{e}^{\mathrm{i}k_{z,j}^{\mathrm{vac}}\Delta z}$ and the related eigenvectors $\tilde{\boldsymbol{F}}_j^{+\mathrm{vac}}$ correspond to waves traveling from left to right while the eigenvalues $\mathrm{e}^{-\mathrm{i}k_{z,j}^{\mathrm{vac}}\Delta z}$ and corresponding eigenvectors $\tilde{\boldsymbol{F}}_j^{-\mathrm{vac}}$ describe waves traveling in the opposite direction. Each eigenvalue is doubly degenerate and corresponds to the two possible polarization states of electromagnetic waves. Note also that typically only a few vacuum modes are propagative (i.e., $k_{z,j}^{\mathrm{vac}}$ is a real number). Especially for low frequencies, the majority of the vacuum modes is evanescent, (i.e. $k_{z,j}^{\mathrm{vac}}$ is imaginary) as it can be easily seen from Eq. (5.25).

Transformation of an arbitrary transfer matrix $\mathbf{T}$ into the plane wave basis can be accomplished using a unitary transformation $\mathbf{S}$:

$$
\bar{\mathbf{T}} = \mathbf{S}^\dagger \cdot \mathbf{T} \cdot \mathbf{S},
\tag{5.27}
$$

where the columns of the unitary matrix $\mathbf{S}$ are formed by the eigenvectors $\tilde{\boldsymbol{F}}_j^{\text{vac}}$, provided they are normalized to unity. With regard to the order of the eigenvectors introduced in Eq. (5.26), we denote the distinct blocks of the matrix $\bar{\mathbf{T}}$ as follows:

$$\bar{\mathbf{T}} = \begin{pmatrix} \bar{\mathbf{T}}^{++} & \bar{\mathbf{T}}^{+-} \\ \bar{\mathbf{T}}^{-+} & \bar{\mathbf{T}}^{--} \end{pmatrix} \tag{5.28}$$

Now it is straightforward to calculate the transmittance and reflectance matrices [251]. If the structure is irradiated by a wave traveling from left, the appropriate transmittance and reflectance matrices $\mathbf{T}_{\text{L}}$ and $\mathbf{R}_{\text{L}}$ should obey the relation (Fig. 5.3)

$$\begin{pmatrix} \mathbf{T}_{\text{L}} \\ \mathbf{0} \end{pmatrix} = \begin{pmatrix} \bar{\mathbf{T}}^{++} & \bar{\mathbf{T}}^{+-} \\ \bar{\mathbf{T}}^{-+} & \bar{\mathbf{T}}^{--} \end{pmatrix} \cdot \begin{pmatrix} \mathbf{1} \\ \mathbf{R}_{\text{L}} \end{pmatrix}, \tag{5.29}$$

where $\mathbf{1}$ is an identity matrix, representing all the modes which can impinge on the structure. The transmittance and reflectance matrices thus read

$$\begin{aligned} \mathbf{T}_{\text{L}} &= \bar{\mathbf{T}}^{++} - \bar{\mathbf{T}}^{+-} \cdot (\bar{\mathbf{T}}^{--})^{-1} \cdot \bar{\mathbf{T}}^{-+} \\ \mathbf{R}_{\text{L}} &= -(\bar{\mathbf{T}}^{--})^{-1} \cdot \bar{\mathbf{T}}^{-+}. \end{aligned} \tag{5.30}$$

The meaning of elements of these matrices is clear. For example, the element $\mathbf{T}_{\text{L},jk}$ describes how the mode k (incident of the structure) couples into the mode j transmitted through the structure.

Analogically, if the structure is irradiated by a wave traveling from the right, the transmittance and reflectance matrices $\mathbf{T}_{\text{R}}$ and $\mathbf{R}_{\text{R}}$ should obey the relation

$$\begin{pmatrix} \mathbf{R}_{\text{R}} \\ \mathbf{1} \end{pmatrix} = \begin{pmatrix} \bar{\mathbf{T}}^{++} & \bar{\mathbf{T}}^{+-} \\ \bar{\mathbf{T}}^{-+} & \bar{\mathbf{T}}^{--} \end{pmatrix} \cdot \begin{pmatrix} \mathbf{0} \\ \mathbf{T}_{\text{R}} \end{pmatrix}, \tag{5.31}$$
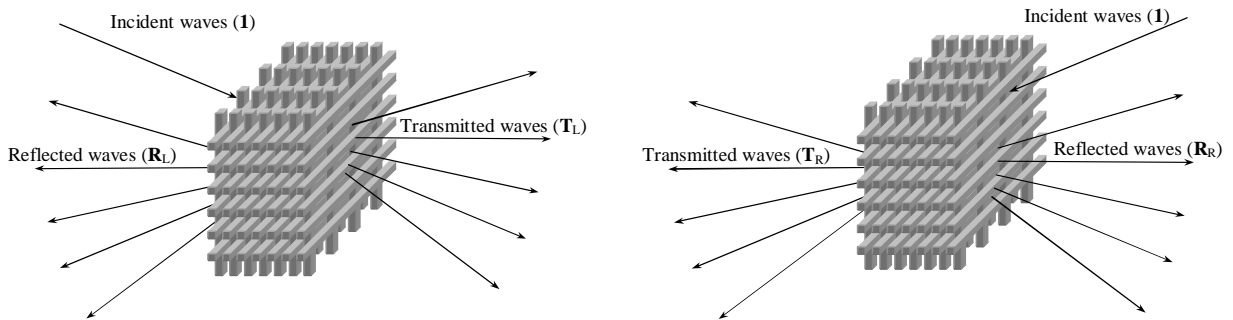
Figure 5.3: Transmittance and reflectance spectra of a multi-dimensional structure. Single incident wave does not produce just one reflected and transmitted wave as in the case of multi-layered stacks, but also diffracted modes may be excited. The modes may be generally both propagative or evanescent.

resulting in

$$\begin{aligned}
\mathbf{T}_R &= (\bar{\mathbf{T}}^{--})^{-1} \\
\mathbf{R}_R &= \bar{\mathbf{T}}^{+-} \cdot (\bar{\mathbf{T}}^{--})^{-1}
\end{aligned} \tag{5.32}$$

Though the algorithm based on composition of transfer matrices seems to be very simple, it suffers from an essential numerical instability. The transfer matrix $\mathbf{T}$ nearly always contains huge eigenvalues corresponding to evanescent waves growing to the right, and at the same time, there are very small eigenvalues for evanescent waves decaying towards the right [cf. Eq. (5.26)]. Composition of such matrices must necessarily lead to wrong values of the small eigenvalues, resulting in incorrect calculation of corresponding modes and subsequently in a numerical instability.

In order to suppress the instability, a multiple scattering formula has to be used [251]. Let us denote by indices 1, 2 and $1+2$ the matrices corresponding to sub-structures 1, 2, and to their composition, respectively. Instead of calculating the transfer matrix of the composed structure $1 + 2$ as a product of the transfer matrices corresponding to the sub-structures ($\mathbf{T}_{1+2} = \mathbf{T}_1 \mathbf{T}_2$), we may develop an algorithm entirely based on transmittance and reflectance matrices. For this purpose, one has to express the transfer matrices $\mathbf{T}_1$ and $\mathbf{T}_2$ in terms of transmittance and reflectance matrices, and subsequently, to calculate the transmittance and reflectance matrices of the composed structure $1+2$. A straightforward calculation based on Eqs. (5.30) and (5.32) yields

$$\begin{aligned}
\mathbf{T}_{R,1+2} &= \mathbf{T}_{R,1}(\mathbf{1} - \mathbf{R}_{L,2}\,\mathbf{R}_{R,1})^{-1}\,\mathbf{T}_{R,2} \\
\mathbf{R}_{R,1+2} &= \mathbf{R}_{R,2} + \mathbf{T}_{L,2}\,\mathbf{R}_{R,1}(\mathbf{1} - \mathbf{R}_{L,2}\,\mathbf{R}_{R,1})^{-1}\,\mathbf{T}_{R,2} \\
\mathbf{T}_{L,1+2} &= \mathbf{T}_{L,2}(\mathbf{1} - \mathbf{R}_{R,1}\,\mathbf{R}_{L,2})^{-1}\,\mathbf{T}_{L,1} \\
\mathbf{R}_{L,1+2} &= \mathbf{R}_{L,1} + \mathbf{T}_{R,1}\,\mathbf{R}_{L,2}(\mathbf{1} - \mathbf{R}_{R,1}\,\mathbf{R}_{L,2})^{-1}\,\mathbf{T}_{L,1}.
\end{aligned} \tag{5.33}$$

This procedure is equivalent to the multiplication of transfer matrices. However, the algorithm (5.33) is numerically much more stable than the multiplication of matrices, as the difference between the highest and lowest eigenvalues is considerably reduced. The disadvantage of this method consists in the degradation of the computational speed as each composition takes $O((N_x N_y)^3)$ operations. In practice, the transfer matrices are thus multiplied for relatively thin slices for which the ratios between the large and small eigenvalues of the transfer matrix still remain reasonable. Multiple scattering formalism is then employed in order to connect together these slices.

Chapter 6

Study of a grating coupler

Periodically modulated dielectric waveguides (i.e. dielectric gratings) have attracted considerable attention especially due to the possibility of optimization of quasi-phase matching for second-harmonic generation [213, 214]. Elements based on periodically modulated waveguides are also very promising from the point of view of applications in optical communications: They can serve for construction of efficient input/output couplers, splitters, filters or signal multiplexers [215–217]. The dielectric core of the waveguide can be replaced by a metal: The guiding is then accomplished by excitation of surface plasmon polaritons [255]. This can lead to further miniaturization of photonic circuits [256, 257].

The problem of linear guided modes in periodic gratings has been rigorously described a long time ago e.g. by Peng et al. [258]. However, since this period only little has been learned about the band structure of these modes and especially about corresponding radiation losses in dielectric gratings. Theoretical studies were performed for example on gratings with low modulation of permittivity of constituting materials, on shallow gratings or conversely, on infinitely thick gratings; usually only a narrow frequency range has been examined [216, 259, 260].

There are several phenomena which make the periodically modulated dielectric waveguides interesting even in the case of low modulation of permittivity. In particular, owing to the periodicity the momentum conservation law does not hold strictly any more: Momentum conservation modulo reciprocal lattice vector is only required. In turn, a propagative plane wave coming from the surrounding medium can couple into some of the guided modes. Excitation of a guided mode usually results in narrow features in transmittance spectra. From the angular dependence of frequency of these features it is possible to partially reconstruct the photonic band structure of the guided modes [261–263].

The authors in Ref. [263] conducted an experimental study of a thin grating on a substrate and of a free-standing thick grating. While they succeeded in interpreting weakly periodically modulated grating coupler in terms of band structure of a planar waveguide, an interpretation of the measurements on the thick grating is the subject of this chapter.

In order to explain the experimental data from Ref. [263], the transfer matrix method

(TMM) described in Sec. 5.3 is first employed for numerical simulation of the transmittance spectra. Based on these spectra, the reconstruction of the band structure of guided modes is performed in Sec. 6.1. Next, in Sec. 6.2, a rigorous modal approach is applied for direct calculation of the band structure of guided modes. Results obtained using these two approaches are finally compared and discussed in Sec. 6.3.

The scheme of the investigated structure is shown in Fig. 6.1. In the calculations, we assume the grating thickness $d = 210\,\mu\text{m}$, period $L = 385\,\mu\text{m}$ and filling factor (ratio between the integrated areas of silicon and the total grating area) $\xi = 0.455$ in accordance with Ref. [263]. The real part of permittivity is set to 11.68 (permittivity of silicon). In the case of the TMM simulation, frequency independent dielectric losses 0.008i are included to match the transmittance spectra with experiment. However, the dielectric losses are omitted in the rigorous modal approach in order to determine correctly the proper radiation losses.

We assume that the structure is infinite along the y-direction and that the plane of incidence of electromagnetic radiation is perpendicular to the grooves. The problem is 2D and in turn, Maxwell's equations split into two independent systems describing TE- and TM-modes, respectively. As the experiments in Ref. [263] have been carried out using TE-polarization only (electric field parallel with grooves), we restrict the calculations to this case, too.

6.1 Analysis of transmittance spectra

When a grating is illuminated by a plane wave under an angle of incidence θ (Fig. 6.2), a guided mode may be excited when the wave-vector component parallel with the grating surface $k_{\text{in}}^{\parallel}$ is conserved:

$$k_{\text{in}}^{\parallel} \equiv \frac{\omega}{c}\sin\theta = \beta + mG_1, \tag{6.1}$$

where β is the wave-vector of the guided mode and m is an integer value. (Throughout the entire chapter we assume that β is restricted to the first Brillouin zone, i.e. $|\beta| < \frac{\pi}{L}$.) Conversely, the guided mode can couple into other propagative modes: A part of the
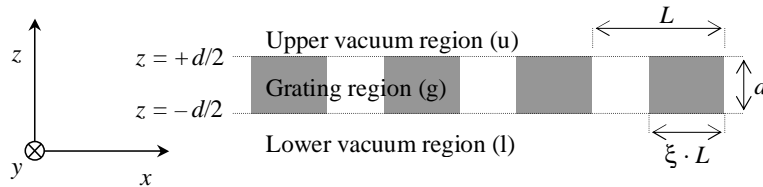
Figure 6.1: Scheme of the investigated grating. Dark regions are made of high-resistivity silicon while regions representing vacuum are in white.
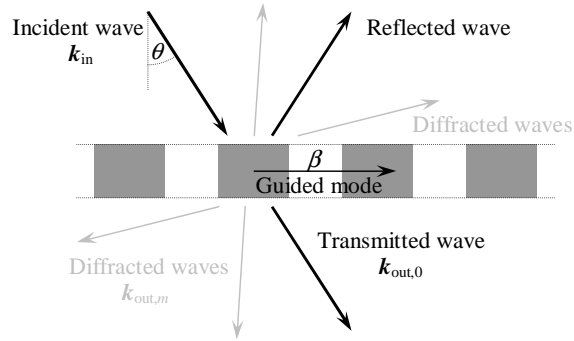
Figure 6.2: Diffraction processes and guiding in a grating: The incident wave may excite a guided mode, which can further couple to diffracted modes.

energy of the guided mode is carried out of the structure by waves which can be classified as transmitted, reflected or diffracted (Fig. 6.2). This results in appearance of narrow features in transmittance spectra [264]. Provided the angular dependence $\omega(\theta)$ of these features is measured or calculated, a part of the band structure $\omega(\beta)$ can be reconstructed from Eq. (6.1) (as $|\sin\theta| \leq 1$, we have no information modes with $\omega/c < |\beta + mG_1|$). The band structure of guided modes represents those modes which are allowed to travel along the x-direction inside the waveguide. It is important to distinguish the band structure of guided modes being calculated here from the band structure of photonic crystals which describe fully delocalized modes.

Here we calculate the transmittance spectra using the TMM described in Sec. 5.3. These spectra are compared with experimental results from Ref. [263] in Fig. 6.3. The agreement between these spectra is very good in the entire frequency range: The global behavior of the transmittance as well as the frequencies of the sharp resonances match very well.

For frequencies below 500 GHz, the spectra in Fig. 6.3 are dominated by wide oscillations with a period of about 200 GHz. These fringes constitute a signature of Fabry–Pérot (FP) effect in a structure which behaves like a homogeneous layer with effective dielectric properties. However, for frequencies above 300 GHz a series of narrow resonances superposed onto the FP fringes develops. These resonances are caused by excitation of guided modes.

In order to reconstruct the band structure of guided waves, the frequencies of corresponding resonances need to be determined. Generally, the shape of the resonance could be well fitted in terms of Fano's resonances [265]. Nevertheless, from the shape of Fano's resonances we expect that the resonant frequencies can be sufficiently accurately approximated by positions of dips in the transmittance spectra. The band structure based on Eq. (6.1) is reconstructed in Fig. 6.4 for both experimental and simulated transmittance spectra.
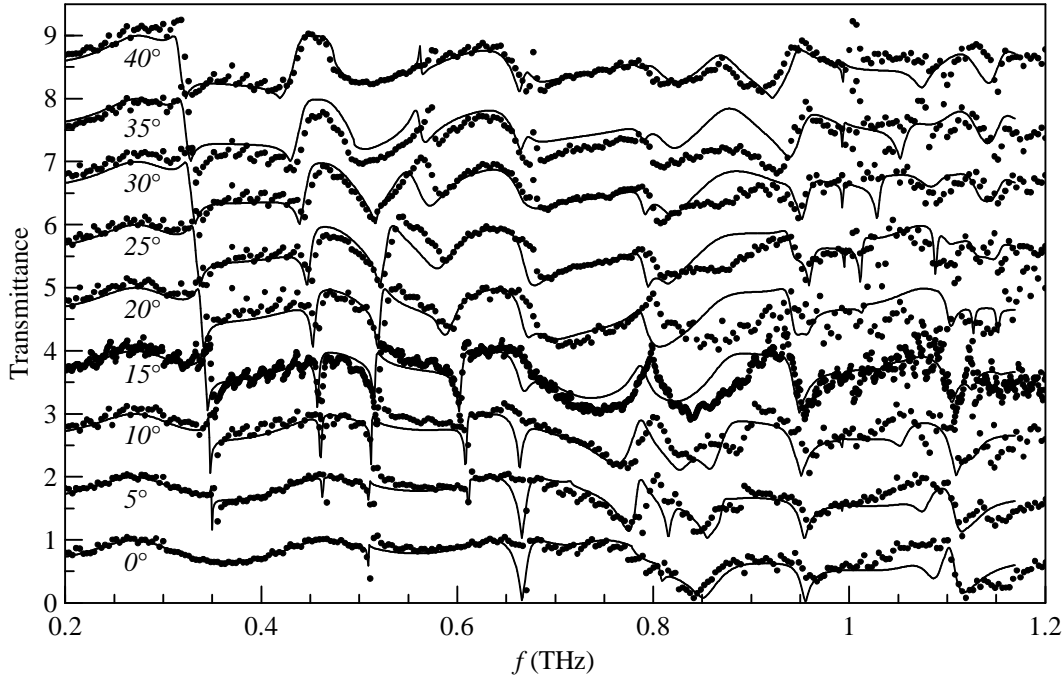
Figure 6.3: Transmittance of the grating versus frequency for different angles of incidence as indicated in the figure. Solid lines: results of the TMM simulation, points: experimental results from Ref. [263]. Each plot has been shifted vertically by 1 as compared to the one below.

In the figure, we can infer on existence of forbidden bands, which are expected to arise in periodically modulated structures. A more detailed discussion will follow in Sec. 6.3. Here we only note that several problems are encountered in the analysis of the transmittance spectra. For example, it is nearly impossible to distinguish features due to FP reflections and due to excitation of guided modes, especially for higher angles of incidence and higher frequencies. The shape of the transmittance curve also becomes very complicated when modes with similar frequencies are excited. This method does not also provide any information about the modes below the light line in vacuum ($|\beta| > \frac{\omega}{c}$) as they cannot be excited by a propagative wave from the exterior.

6.2   Modal approach

The investigated structure can be divided into three regions: into homogeneous upper and lower vacuum regions and into a periodic grating region (Fig. 6.1). The field in each region can be expressed as a superposition of its eigenmodes. In the modal approach, one seeks for such combinations of the eigenmodes which satisfy appropriate boundary conditions.
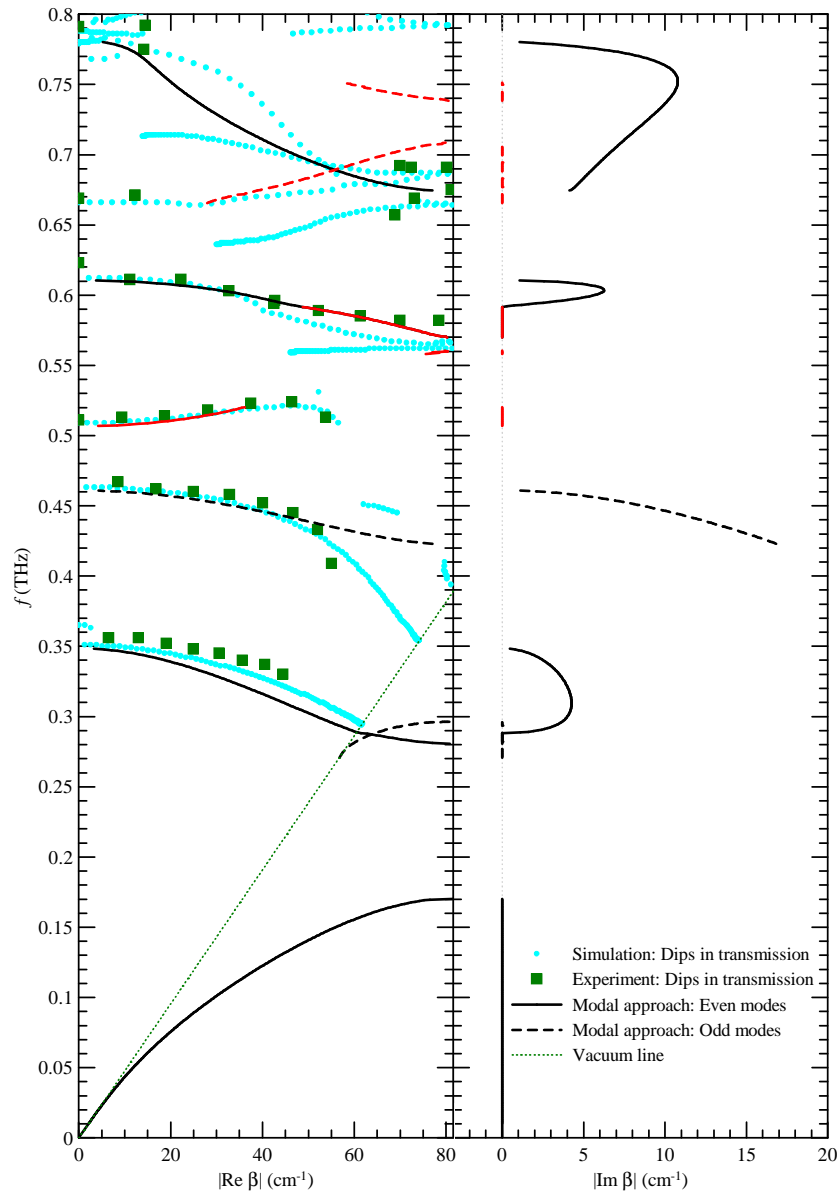
Figure 6.4: Band structure of guided modes in the investigated grating. The blue circles are result of band-structure reconstruction based on numerically calculated transmittance spectra (Sec. 6.1) while the green squares represent band-structure reconstruction based on the experimental data from Ref. [263]. The dispersion of guided modes calculated using the modal approach is plotted using black solid lines for even modes and using black dashed lines for odd modes. The modes with $|\operatorname{Im}\beta| > 0$ are leaky. The red curves represent the resonant modes for which the expression (6.17) becomes particularly small (but non-zero within the computer precision). The dotted green line indicates dispersion of light in vacuum. The differences between individual data are discussed in Sec. 6.3.

For this purpose, we start with construction of eigenmodes in the grating and vacuum regions. Next, we match the fields at the interfaces between the grating and vacuum regions and impose appropriate boundary conditions on fields when $|z| \to \infty$. The resulting equation is finally solved numerically.

The Maxwell's equations relevant for characterization of eigenmodes for the TE polarization read (refer to Eqs. (5.2)):

$$
\begin{aligned}
-\frac{\partial E_y}{\partial z} &= \mathrm{i}\omega\mu_0 H_x \\
\frac{\partial E_y}{\partial x} &= \mathrm{i}\omega\mu_0 H_z \\
\frac{\partial H_x}{\partial z} - \frac{\partial H_z}{\partial x} &= -\mathrm{i}\omega\varepsilon_0\varepsilon(x)E_y
\end{aligned}
\tag{6.2}
$$

where the fields E_y, H_x and H_z depend on x- and z- coordinates only. Substitution for H_x and H_z yields the fundamental wave-equation:

$$
\frac{\partial^2 E_y}{\partial x^2} + \frac{\partial^2 E_y}{\partial z^2} = -k_0^2\varepsilon(x)E_y,
\tag{6.3}
$$

where $k_0 = \omega/c$. Periodicity of the problem in the x-direction allows us to expand the solution in terms of Bloch's waves. Furthermore, as the separate regions are homogeneous in the z-direction, the fields can be taken in the form

$$
E_y(x, z) = \sum_G F_G \mathrm{e}^{\mathrm{i}k_z z + \mathrm{i}(\beta + G)x}.
\tag{6.4}
$$

The sum runs over all reciprocal lattice vectors $G = \frac{2\pi m}{L}$, where m is an integer value. Substitution of this sum into the wave equation (6.3) yields an eigenvalue problem (k_z may be a general complex number):

$$
k_0^2 \sum_{G'} \varepsilon_{G-G'} F_{G'} - (\beta + G)^2 F_G = k_z^2 F_G,
\tag{6.5}
$$

in which the Fourier components ε_G of the permittivity are defined as

$$
\varepsilon_G = \frac{1}{L} \int_0^L \varepsilon(x)\mathrm{e}^{-\mathrm{i}Gx}\mathrm{d}x.
\tag{6.6}
$$

Solution of the secular equation (6.5) is trivial for the vacuum regions, as $\varepsilon_{G-G'} = \delta_{GG'}$ and therefore the matrix on the left-hand side is diagonal (the eigenmodes are either propagative or evanescent plane waves). Denoting the q-th eigenvalue k_z in the vacuum regions as v_q and the components of the corresponding eigenvector F_G as V_{Gq}, we can immediately write

$$
\begin{aligned}
V_{Gq} &= \delta_{Gq} \\
v_q^2 &\equiv v_G^2 = k_0^2 - (\beta + G)^2.
\end{aligned}
\tag{6.7}
$$

In the grating region, we denote the q-th eigenvalue k_z as a_q and the components of the corresponding eigenvector F_G as A_{Gq}. However, in this case we need to solve Eq. (6.5) numerically.

The field in each region can be expressed as an arbitrary superposition of the eigenmodes. Thus in the grating region (g),

$$
\begin{aligned}
E_y^{\mathrm{g}}(x,z) &= \sum_q \sum_G \alpha_q^+ A_{Gq} \mathrm{e}^{\mathrm{i}(\beta+G)x+\mathrm{i}a_q z} + \sum_q \sum_G \alpha_q^- A_{Gq} \mathrm{e}^{\mathrm{i}(\beta+G)x-\mathrm{i}a_q z} \\
\mu_0 \omega H_x^{\mathrm{g}}(x,z) &= -\sum_q \sum_G \alpha_q^+ A_{Gq} a_q \mathrm{e}^{\mathrm{i}(\beta+G)x+\mathrm{i}a_q z} + \sum_q \sum_G \alpha_q^- A_{Gq} a_q \mathrm{e}^{\mathrm{i}(\beta+G)x-\mathrm{i}a_q z}
\end{aligned}
\tag{6.8}
$$

where $\alpha_q^{\pm}$ is the amplitude of the q-th eigenmode. Analogically, the field in the upper (u) and lower (l) vacuum region can be written as a superposition of plane waves with amplitudes $\nu_G^{\mathrm{u/l}\pm}$:

$$
\begin{aligned}
E_y^{\mathrm{u/l}}(x,z) &= \sum_G \nu_G^{\mathrm{u/l}+} \mathrm{e}^{\mathrm{i}(\beta+G)x+\mathrm{i}v_G z} + \sum_G \nu_G^{\mathrm{u/l}-} \mathrm{e}^{\mathrm{i}(\beta+G)x-\mathrm{i}v_G z} \\
\mu_0 \omega H_x^{\mathrm{u/l}}(x,z) &= -\sum_G \nu_G^{\mathrm{u/l}+} v_G \mathrm{e}^{\mathrm{i}(\beta+G)x+\mathrm{i}v_G z} + \sum_G \nu_G^{\mathrm{u/l}-} v_G \mathrm{e}^{\mathrm{i}(\beta+G)x-\mathrm{i}v_G z}.
\end{aligned}
\tag{6.9}
$$

As the tangential components of electric and magnetic field must be continuous across interfaces, following boundary conditions need to be satisfied:

$$
\begin{aligned}
E_y^{\mathrm{g}}(x,z=+d/2) &= E_y^{\mathrm{u}}(x,z=+d/2) \\
H_x^{\mathrm{g}}(x,z=+d/2) &= H_x^{\mathrm{u}}(x,z=+d/2) \\
E_y^{\mathrm{g}}(x,z=-d/2) &= E_y^{\mathrm{l}}(x,z=-d/2) \\
H_x^{\mathrm{g}}(x,z=-d/2) &= H_x^{\mathrm{l}}(x,z=-d/2)
\end{aligned}
\tag{6.10}
$$

Finally, we have to impose boundary conditions for $|z| \to \infty$. We assume that the grating is irradiated by a single plane wave with parallel wave-vector $\beta + \Gamma$ (Γ is an arbitrary reciprocal lattice vector)* from the upper vacuum region. However, no wave is incident onto the grating from the lower vacuum region. In this case, the electric field in the upper half-space described by Eq. (6.9) reads ($\mathrm{Re}\, v_G \geq 0$, $\mathrm{Im}\, v_G \geq 0$)

$$
\begin{aligned}
E_y^{\mathrm{u}}(x,z) &= \sum_G \nu_G^{\mathrm{u}+} \mathrm{e}^{\mathrm{i}(\beta+G)x+\mathrm{i}v_G z} + \nu_\Gamma^{\mathrm{u}-} \mathrm{e}^{\mathrm{i}(\beta+\Gamma)x-\mathrm{i}v_\Gamma z} \\
\mu_0 \omega H_x^{\mathrm{u}}(x,z) &= -\sum_G \nu_G^{\mathrm{u}+} v_G \mathrm{e}^{\mathrm{i}(\beta+G)x+\mathrm{i}v_G z} + \nu_\Gamma^{\mathrm{u}-} v_\Gamma \mathrm{e}^{\mathrm{i}(\beta+\Gamma)x-\mathrm{i}v_\Gamma z}.
\end{aligned}
\tag{6.11}
$$

---

*We systematically assume β to lie in the first Brillouin zone. Hence the addition of the reciprocal lattice vector Γ is required to account for all possible waves propagating in the vacuum.

The second right-hand side terms describe the incident wave while the first right-hand side terms include the waves reflected and diffracted by the grating and the evanescent field of the modes guided by the grating. Similarly, the field in the lower half-space is expressed as

$$
\begin{aligned}
E_y^{\mathrm{l}}(x, z) &= \sum_G \nu_G^{\mathrm{l}-} \mathrm{e}^{\mathrm{i}(\beta+G)x - \mathrm{i}v_G z} \\
\mu_0 \omega H_x^{\mathrm{l}}(x, z) &= \sum_G \nu_G^{\mathrm{l}-} v_G \mathrm{e}^{\mathrm{i}(\beta+G)x - \mathrm{i}v_G z}.
\end{aligned}
\tag{6.12}
$$

Using Eqs. (6.10), we can now eliminate $\nu^{\mathrm{u}+}$ and $\nu^{\mathrm{l}-}$, resulting in a set of equations which must be satisfied for all G:

$$
\begin{aligned}
\sum_q \alpha_q^+ \underbrace{A_{Gq}(v_G - a_q)\mathrm{e}^{\mathrm{i}a_q d/2}}_{=M_{Gq}} + \sum_q \alpha_q^- \underbrace{A_{Gq}(v_G + a_q)\mathrm{e}^{-\mathrm{i}a_q d/2}}_{=P_{Gq}} &= e_G(\Gamma) \\
\sum_q \alpha_q^+ \underbrace{A_{Gq}(v_G + a_q)\mathrm{e}^{-\mathrm{i}a_q d/2}}_{=P_{Gq}} + \sum_q \alpha_q^- \underbrace{A_{Gq}(v_G - a_q)\mathrm{e}^{\mathrm{i}a_q d/2}}_{=M_{Gq}} &= 0,
\end{aligned}
\tag{6.13}
$$

where $e_G(\Gamma) = 2v_G \mathrm{e}^{-\mathrm{i}v_G d/2}$ for $G = \Gamma$ and $e_G(\Gamma) = 0$ for $G \neq \Gamma$. Equivalently, we can write this set in a matrix notation,

$$
\begin{pmatrix} \mathbf{M} & \mathbf{P} \\ \mathbf{P} & \mathbf{M} \end{pmatrix} \begin{pmatrix} \boldsymbol{\alpha}^+ \\ \boldsymbol{\alpha}^- \end{pmatrix} = \begin{pmatrix} \boldsymbol{e} \\ \mathbf{0} \end{pmatrix}
\tag{6.14}
$$

allowing us to express the amplitudes of eigenmodes in the grating region:

$$
\begin{aligned}
\boldsymbol{\alpha}^+ &= [\mathbf{1} - (\mathbf{M}^{-1}\mathbf{P})^2]^{-1} \mathbf{M}^{-1} \boldsymbol{e} \\
\boldsymbol{\alpha}^- &= [\mathbf{1} - (\mathbf{P}^{-1}\mathbf{M})^2]^{-1} \mathbf{P}^{-1} \boldsymbol{e},
\end{aligned}
\tag{6.15}
$$

provided the matrices $\mathbf{M}$ and $\mathbf{P}$ are regular. (The regularity of these matrices was checked during the numerical calculations.)

Guided modes are characterized by an absence of the wave incident from exterior (formally we can write $\boldsymbol{e} = \mathbf{0}$), i.e., the matrix at the left-hand side of Eq. (6.14) has to be singular. Equivalently, this condition can be expressed as

$$
\det(\mathbf{M}^{-1}\mathbf{P} \pm \mathbf{1}) = 0.
\tag{6.16}
$$

The studied structure has a mirror symmetry in the plane $z = 0$, therefore the eigenmodes can be classified according to their parity. In particular, we will refer to odd and even modes with respect to the symmetry of the electric field E_y. Substitution $\boldsymbol{\alpha}^+ = -\mathbf{P}^{-1}\mathbf{M}\boldsymbol{\alpha}^-$ (from Eq. (6.14)) into Eq. (6.8) immediately shows that the upper sign corresponds to odd modes while the lower one corresponds to even modes.

A special care needs to be taken when solving this equation numerically. One should note that Eq. (6.14) with $\boldsymbol{e} = \mathbf{0}$ is satisfied when at least one of the eigenvalues a_q equals to

zero (this fact is easily seen from Eq. (6.13): in this case, the matrix on the left-hand side contains two identical rows hence the determinant vanishes). However, such a situation is in conflict with the expansion (6.8) which is complete, and consequently valid, only if $a_q \neq 0$ for all q [266]. This problem can be avoided if the root of the following expression is sought instead:

$$\frac{|\det(\mathbf{M}^{-1}\mathbf{P} \pm \mathbf{1})|}{\min_q |a_q|}. \tag{6.17}$$

In practice, the following procedure is used for each frequency ω to determine the corresponding set of β. The eigenvalues a_q and eigenvectors A_{Gq} of Eq. (6.5) are numerically computed for a given ω and for a trial complex value of the wave-vector β. We used 11 reciprocal wave-vectors for the field expansion and we verified that no significant change occurred when more wave-vectors were taken into account. Based on the values $a_q(\beta)$ and $A_{Gq}(\beta)$, the determinant of the matrix $\mathbf{M}^{-1}\mathbf{P} \pm \mathbf{1}$ is calculated. This process is repeated in root finding of expression (6.17), which was accomplished by minimization of its square by the simplex method for two variables (real and imaginary part of β) [267].

Two kinds of solutions are found: (i) True guided modes for which β is real and the field outside the grating is evanescent, and (ii) leaky modes for which β is complex, i.e., the mode is attenuated along the structure owing to the radiation of electromagnetic energy out of the structure.

Another interesting situation arises when the matrix $\mathbf{M}^{-1}\mathbf{P} \pm \mathbf{1}$ from Eqs. (6.16) and (6.17) becomes nearly, but not exactly singular. This occurs when the minimum reached during the minimization of the square of Eq. (6.17) is very small but non-zero within the machine precision. The corresponding mode, which we will call *resonant*, strongly resembles to a guided one, however it cannot exist without excitation by a plane wave from the exterior of the waveguide. These modes are analogous to constructive FP interferences observed when a homogeneous planar waveguide (=slab) is irradiated by a wave from the exterior. In the periodically modulated waveguide, even a very weak incident wave can couple a significant amount of energy into resonant modes leading to a considerable enhancement of the field inside the waveguide. This means that an incident radiation with appropriate values of β can efficiently excite resonant modes. In turn, resonant modes cause pronounced features in transmittance spectra (Fig. 6.3).

6.3   Discussion

The results of the modal approach employed in this section are summarized in Fig. 6.4. Obviously, only the true guided modes lie below the vacuum line: These modes do not exhibit any radiation losses as they cannot couple to the modes propagating in vacuum regions. (There are only three such modes in our case.) All guided modes above the vacuum line are leaky. The first leaky mode develops from the true guided mode at 0.29 THz. Note that the radiation losses of the displayed leaky modes are quite high. For

example, the attenuation at $0.32\,\mathrm{THz}$ in silicon with $\varepsilon = 11.68 + 0.008\mathrm{i}$ is just $0.11\,\mathrm{cm}^{-1}$ while the radiation losses in the investigated structure exceed $4\,\mathrm{cm}^{-1}$ in this spectral range. The results of the rigorous modal approach clearly indicate the presence and the spectral positions of forbidden bands. The first forbidden band is quite wide and spreads between 0.17 and $0.27\,\mathrm{THz}$. Note that for frequencies inside the forbidden band the electromagnetic radiation cannot propagate inside the waveguide along the x-direction, and can only radiate into the free space (this fact was used e.g. to design an efficient light-emitting diode [268]).

It is important to compare the band structure reconstructed from transmittance spectra (Sec. 6.1) and the band structure obtained from the rigorous approach (Sec. 6.2). The agreement is quite good for the second and third even mode, starting at $0.35\,\mathrm{THz}$ and $0.61\,\mathrm{THz}$ respectively. On the other hand, the former approach does not permit to distinguish between leaky and resonant modes (e.g. the mode starting at $0.51\,\mathrm{THz}$ and part of the mode ending at $0.57\,\mathrm{THz}$). The band structure reconstruction based on transmittance spectra also fails e.g. for higher β for the odd mode starting at $0.46\,\mathrm{THz}$.

The band structure reconstruction from transmittance spectra becomes particularly tricky for higher frequencies. Firstly, crossings between the dispersion curves of the leaky and resonant modes (e.g. at $0.69\,\mathrm{THz}$) necessarily leads to a complicated behavior of transmittance spectra. Secondly, longer reciprocal lattice vectors start to play a role in Eq. (6.1) for higher frequencies (i.e., m becomes non-zero). This is equivalent to the mapping of the dispersion relation into the first Brillouin zone, which yields further dispersion curves. Though the rigorously defined band structure is unique, the dispersion curves obtained from the transmittance spectra do often considerably differ for various m. This is best seen in the region ~ 0.65–$0.70\,\mathrm{THz}$ where three branches are obtained from the transmittance spectra while there is only a single branch calculated using the rigorous modal approach.

In conclusion, two methods were employed for investigation of properties of a periodically modulated dielectric waveguide. The rigorous approach allows us to distinguish between three interesting features: (i) true guided modes which propagate without radiation losses along the grating and which cannot be detected in the transmittance spectra; (ii) leaky modes which are guided along the structure but show radiation losses; these modes are detected in the transmittance spectra; (iii) other resonant modes, which, on the one hand, cannot exist without excitation by a wave from the exterior, and on the other hand, are characterized by a strong confinement of the electromagnetic field inside the waveguide; these modes are also detected in the transmittance spectra. The method based on the analysis of transmittance spectra provides fingerprints of leaky and resonant modes; however, it does not offer any way to distinguish between them. On the other hand, this method can directly exploit the data obtained from simple transmittance measurements.

We have found that the dispersion of the modes obtained by the two methods are in a quantitative agreement for low frequencies ($f \lesssim c/L$). However, the rigorous modal approach brings more information and is also applicable at higher frequencies.

Chapter 7

Tunable photonic crystals

Photonic crystals (PCs) are artificial materials which can control the flow of the light. In particular, PCs can act as high-quality filters. The filtering parameters are determined by the structure of the PC: Filter properties can be simply modified by changing the structure of the PC. For example, the stop-band frequency can be shifted by scaling the geometrical parameters of the PC. However, such an approach is very cumbersome as it requires to fabricate many PCs, and to replace the PC each time the filtering properties have to be modified. In order to extend the applicability and flexibility of PCs, it is thus very important to control their properties dynamically. There can be several aims of the control, including light switching [269–271], tuning of forbidden bands [272–276] and tuning of defect modes [277–280].

In this chapter we focus on formation of defect modes and on their tunability in 1D PCs operating in the terahertz (THz) range. First, in Sec. 7.1, we investigate theoretically the properties of defect modes in a PC with a twinning defect (see e.g. the scheme in page 92), with a particular interest to the design of a widely tunable structure. A detailed spectroscopic investigation of a PC with variable defect-layer thickness is performed in Sec. 7.2. In this case, the defect is formed by an air layer; its tunability is then achieved by changing its thickness (distance between the right and left part of the structure). Despite the small flexibility of this structure, we use it to demonstrate our model of the defect formation in PCs. Finally, in Sec. 7.3, we present results on thermally tunable PCs. In this section, we design and fabricate PCs widely tunable by temperature, and we perform their theoretical and experimental investigations.

7.1   Twinning defect in one-dimensional photonic crystals

Various defect types can be found in 1D PCs, including vacancies, substitutions or interstitials. Properties of these defects have been covered in several theoretical studies [187, 281–283]. On the other hand, only a little attention has been devoted to the twinning defect, despite the fact that it can be often constructed very easily.
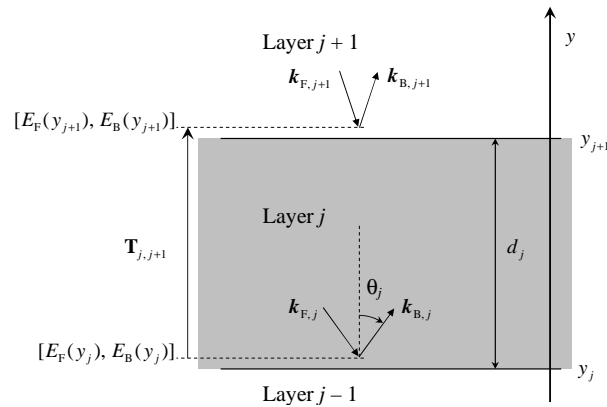
The twinning defect is in detail examined theoretically in this section. We assume that the defect is enclosed between two identical photonic structures, which possess a forbidden band. We investigate in more detail the important case where the photonic structures surrounding the defect are PCs composed of two alternating layers. Throughout this chapter, we assume that all materials exhibit both dielectric and magnetic response. Inclusion of the magnetic response is not generally necessary for PCs operating in the THz or optical range where the dielectric response dominates. However, the magnetic response may be important e.g. in the microwave range: Its inclusion into the theoretical description thus allows to use the results for any spectral region by a simple application of the scaling law [189, 284]. In order to simplify the theoretical analysis, we neglect the losses of the constituting materials.

In this section, we proceed as follows. We recall an alternative formulation of the transfer matrix method (TMM), which is subsequently used to derive analytical formulae describing the formation of the defect mode. This allow us to discuss various mechanisms of tunability of defect modes, and to provide directions for the design of a structure with wide tunability.

Transfer matrix method

The theoretical framework in this section is based on a TMM. In order to preserve coherence with the previously published article (Ref. [285]), we use a slightly different formulation of the TMM as compared to Sec. 5.3. In brief, the transfer matrix now links electric fields of waves propagating forward (E_{F}) and backward (E_{B}) in plane $y = y_j$ with those in plane $y = y_{j+1}$ (Fig. 7.1):

$$\left(\begin{array}{c} E_{\mathrm{F}}(y_{j+1}) \\ E_{\mathrm{B}}(y_{j+1}) \end{array} \right) = \mathbf{T}_{j,j+1} \cdot \left(\begin{array}{c} E_{\mathrm{F}}(y_j) \\ E_{\mathrm{B}}(y_j) \end{array} \right). \tag{7.1}$$

Figure 7.1: Schematic of parameters of the TMM utilized in this chapter.

The transfer matrix for the j-th homogeneous layer reads

$$\mathbf{T}_{j,j+1} = \begin{pmatrix} T_{11} & T_{12} \\ T_{21} & T_{22} \end{pmatrix} =$$
$$= \frac{w_{j,j+1}}{2} \begin{pmatrix} (1+x_{j,j+1})\exp(-\mathrm{i}k_{y,j}d_j) & (1-x_{j,j+1})\exp(+\mathrm{i}k_{y,j}d_j) \\ (1-x_{j,j+1})\exp(-\mathrm{i}k_{y,j}d_j) & (1+x_{j,j+1})\exp(+\mathrm{i}k_{y,j}d_j) \end{pmatrix} \tag{7.2}$$

where $k_{y,j} = (\omega n_j/c)\cos\theta_j$ is the y-component of the wave vector in the j-th layer, d_j and n_j are its thickness and refractive index, respectively, θ_j is the angle between the wave vector and the y-axis, f is the frequency and c is the speed of light in vacuum. The parameters $w_{j,j+1}$ and $x_{j,j+1}$ differ for TE and TM polarizations (z_j is the wave impedance of the j-th layer):

$$\left. \begin{array}{cc} \text{TE polarization} & \text{TM polarization} \\[2mm] w_{j,j+1} = 1 & w_{j,j+1} = \dfrac{\cos\theta_j}{\cos\theta_{j+1}} \\[4mm] x_{j,j+1} = \dfrac{z_{j+1}}{z_j}\cdot\dfrac{\cos\theta_j}{\cos\theta_{j+1}} & x_{j,j+1} = \dfrac{z_{j+1}}{z_j}\cdot\dfrac{\cos\theta_{j+1}}{\cos\theta_j} \end{array} \right\} \tag{7.3}$$

The angles θ_j are determined by the Snell's law:

$$n_j \sin\theta_j = n_{j+1}\sin\theta_{j+1}. \tag{7.4}$$

As we are dealing with non-absorbing media, the elements of the matrix $\mathbf{T}_{j,j+1}$ satisfy the relations

$$T_{22} = T_{11}^* \quad \text{and} \quad T_{12} = T_{21}^*. \tag{7.5}$$

The relations (7.5) equally hold for any stack of non-absorbing layers. For such a structure, characterized by a transfer matrix $\mathbf{Q}$, we can write

$$\begin{pmatrix} E_{\mathrm{I}} \\ E_{\mathrm{R}} \end{pmatrix} = \begin{pmatrix} Q_{11} & Q_{21}^* \\ Q_{21} & Q_{11}^* \end{pmatrix} \cdot \begin{pmatrix} E_{\mathrm{T}} \\ 0 \end{pmatrix} \tag{7.6}$$

where E_{I}, E_{R}, and E_{T} stand for incident, reflected, and transmitted electric fields, respectively. It is then clear that the expressions $1/Q_{11}$ and Q_{21}/Q_{11} can be identified with complex transmittance and reflectance, respectively, i.e., the transfer matrix of any structure can be expressed in terms of its complex transmittance ($T = E_{\mathrm{T}}/E_{\mathrm{I}}$) and reflectance ($R = E_{\mathrm{R}}/E_{\mathrm{I}}$):

$$\begin{pmatrix} E_{\mathrm{I}} \\ E_{\mathrm{R}} \end{pmatrix} = \begin{pmatrix} 1/T & R^*/T^* \\ R/T & 1/T^* \end{pmatrix} \cdot \begin{pmatrix} E_{\mathrm{T}} \\ 0 \end{pmatrix}. \tag{7.7}$$

Description of twinning defect

A scheme of the structure under investigation is shown in Fig. 7.2. The structure consists of a defect (D), surrounded by Bragg mirrors—PCs created as a repeated sequence of layers $F \ldots L$.

The transfer matrix $\mathbf{M}$ linking the fields in the middle of the defect structure and in the outer medium is given by:

$$\mathbf{M} = \mathbf{A} \cdot \mathbf{S}^N \cdot \boldsymbol{\Delta} \tag{7.8}$$

where $\mathbf{S}$ is the transfer matrix of a unit cell of the PC and $\boldsymbol{\Delta}$ is the transfer matrix of a "half" of the defect structure (see Fig. 7.2). Matrix $\mathbf{A}$ stands for the interface between the outer medium and the PC. This interface is considered as an infinitesimally thin layer $\tilde{L}$ with the same wave impedance and refractive index as the last layer L adjacent to the defect. This formally introduced layer does not change the physical properties of the structure but it allows clear separation of the properties of the Bragg mirrors (as described by the matrix $\mathbf{S}^N$) from the coupling to the outer medium.

It is convenient to express the transfer matrix $\mathbf{S}^N$ in terms of complex transmittance $(te^{i\tau})$ and reflectance $(re^{i\varrho})$ of the Bragg mirrors. If the Bragg mirror is irradiated by a wave E_{I} from the left side, the transmitted and reflected waves $E_{\mathrm{T}} = E_{\mathrm{I}}te^{i\tau}$ and $E_{\mathrm{R}} = E_{\mathrm{I}}re^{i\varrho}$, respectively, have to fulfill

$$\begin{pmatrix} E_{\mathrm{I}} \\ E_{\mathrm{R}} \end{pmatrix} = \mathbf{S}^N \cdot \begin{pmatrix} E_{\mathrm{T}} \\ 0 \end{pmatrix}. \tag{7.9}$$

Following Eq. (7.7), the matrix $\mathbf{S}^N$ reads

$$\mathbf{S}^N = \frac{1}{t} \begin{pmatrix} e^{-i\tau} & re^{-i(\varrho-\tau)} \\ re^{i(\varrho-\tau)} & e^{i\tau} \end{pmatrix}. \tag{7.10}$$

Since we do not consider absorbing media, $r^2 + t^2 = 1$.
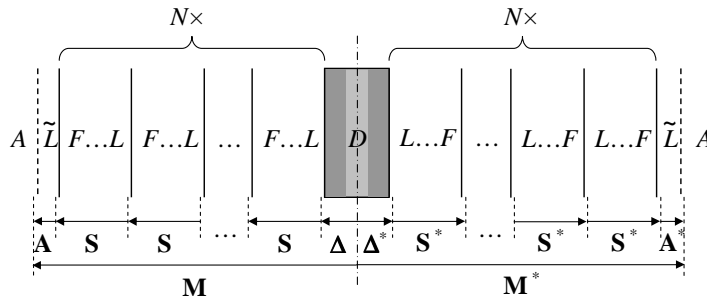
Figure 7.2: The scheme of the investigated structure and the corresponding transfer matrices. A single period of the PC (Bragg mirror) consists of an arbitrary sequence of layers $F \ldots L$, starting with F and ending with L; the period is repeated N times. The defect is denoted by D while the outer medium is labeled as A. The role of the layer $\tilde{L}$ is described in the text.

Defect modes are eigenmodes of the structure; their electromagnetic field is localized close to the defect layer. The problem possesses a mirror symmetry, therefore the eigenmodes can be classified according to their parity. The corresponding fields in the middle of the structure thus read

$$\begin{pmatrix} 1 \\ \pm 1 \end{pmatrix}, \tag{7.11}$$

where the upper and lower sign describes even and odd modes, respectively, according to the symmetry of the electric field. Application of the transfer matrix $\mathbf{M}$ then yields the fields at the boundaries of the entire structure. These fields must vanish for defect modes, i.e.,

$$\mathbf{M} \begin{pmatrix} 1 \\ \pm 1 \end{pmatrix} = \begin{pmatrix} 0 \\ 0 \end{pmatrix} \quad \text{and} \quad \mathbf{M}^* \begin{pmatrix} 1 \\ \pm 1 \end{pmatrix} = \begin{pmatrix} 0 \\ 0 \end{pmatrix} \tag{7.12}$$

for the left and right face of the structure, respectively. These equations are equivalent and represent conditions for frequencies of defect modes. Using Eq. (7.5), they can be reduced to a very simple form

$$M_{11} \pm M_{21}^* = 0. \tag{7.13}$$

We now restrict ourselves only to frequencies for which the Bragg mirrors surrounding the defect exhibit a photonic band gap. The presence of the structural defect between the Bragg mirrors can lead to an emergence of defect mode(s) in the forbidden band, i.e., the transmittance of the entire structure reaches 1 while its reflectance vanishes. Assuming that the Bragg mirrors surrounding the defect are perfect in the sense that $t \to 0$ and $r \to 1$ in the forbidden band, Eq. (7.13) yields after a direct but lengthy calculation

$$e^{i(\varrho - 2\tau)} = -\frac{\Delta_{21} \pm \Delta_{11}^*}{\Delta_{11} \pm \Delta_{21}^*}. \tag{7.14}$$

The amplitude of both sides of this equation is obviously equal to 1, therefore it is sufficient to consider only the phase. One finds:

$$\begin{aligned} 2\tau - \varrho &= 2\arg(\Delta_{11} + \Delta_{21}^*) + (2n+1)\pi & \text{(upper sign, i.e. even modes)} \\ 2\tau - \varrho &= 2\arg(\Delta_{11} - \Delta_{21}^*) + 2n\pi & \text{(lower sign, i.e. odd modes)}, \end{aligned} \tag{7.15}$$

where arg denotes the argument of a complex number and n is an arbitrary integer value. Eq. (7.15) does not contain the properties of the outer medium A. This is because we are working in the limit of perfect Bragg mirrors: The defect modes are strongly localized in the vicinity of the defect, therefore their interaction with the outer medium A is eliminated.

If the defect D is a single homogeneous layer with thickness d_{D}, the substitution of Eq. (7.2) for $\boldsymbol{\Delta}$ allows to simplify the results of Eqs. (7.15) into a single expression:

$$k_{y,\mathrm{D}}d_{\mathrm{D}} = m\pi + \underbrace{2\arctan\left(\frac{\tan\kappa}{x_{\mathrm{D,L}}}\right)}_{\varphi}, \quad \text{where} \quad \kappa = \frac{\varrho(f) - 2\tau(f) + \pi}{2}, \tag{7.16a}$$

or equivalently,

$$k_{y,\mathrm{D}}d_{\mathrm{D}} = (m+1)\pi - 2\underbrace{\arctan\left(\frac{x_{\mathrm{D,L}}}{\tan\kappa}\right)}_{\tilde{\varphi}}. \tag{7.16b}$$

The integer m now serves for unique identification of defect modes: Even values denote even modes while odd values correspond to odd modes. Owing to the frequency dependence of the phase spectra $\varrho(f)$ and $\tau(f)$, Eqs. (7.16) are transcendent for the frequency of defect mode. Nevertheless, the relative tunability of defect modes by the relative variation of the defect thickness can be calculated analytically:

$$\frac{d_{\mathrm{D}}}{f}\frac{\mathrm{d}f}{\mathrm{d}d_{\mathrm{D}}} = -\frac{1}{1 - \dfrac{cx_{\mathrm{D,L}}}{\pi n_{\mathrm{D}}d_{\mathrm{D}}\cos\theta_{\mathrm{D}}}\cdot\dfrac{\mathrm{d}\kappa}{\mathrm{d}f}\cdot\dfrac{1}{(1-x_{\mathrm{D,L}}^2)\cos(\varrho-2\tau)+(x_{\mathrm{D,L}}^2+1)}}. \tag{7.17}$$

Providing the fields are homogeneous in x and z directions ($\theta_j = 0$ for all j), the thickness of the defect layer and its refractive index appear just in the form of a product $d_{\mathrm{D}}n_{\mathrm{D}}$. In this case, the relative tunability of defect modes by the relative variation of n_{D} is described by an identical expression.

We now calculate the enhancement of the electromagnetic field in the middle of the defect. Fot that purpose we need to evaluate the electric fields that are propagating forward (E_{F}) and backward (E_{B}) in the middle of the defect. Let us consider the case when the structure is irradiated only from the left side by a wave with electric field E_{I}. The magnitudes of the total electric field ($= E_{\mathrm{F}} + E_{\mathrm{B}}$) and of the total magnetic induction ($= (E_{\mathrm{F}} - E_{\mathrm{B}})n_{\mathrm{D}}/c$) in the middle of the defect are determined using

$$E_{\mathrm{F}} \pm E_{\mathrm{B}} = \frac{1}{M_{11} \pm M_{21}^*}E_{\mathrm{I}}. \tag{7.18}$$

The enhancement of the field is the strongest for frequencies corresponding to defect modes in the limit of perfect Bragg mirrors (Eqs. (7.15)) [183]. However, it is necessary to use $t \neq 0$ when substituting into Eq. (7.18). The divergence in the limit $t \to 0$ has origin in the fact that the defect mode is fully localized in the limit $t = 0$ and thus the problem does not support propagative modes, which are essential for the definition of the field enhancement.

For even defect modes and upper signs in Eq. (7.18) or for odd defect modes and lower signs, the substitution for $\mathbf{M}$ from Eqs. (7.8) and (7.10) yields

$$\frac{E_{\mathrm{F}} \pm E_{\mathrm{B}}}{E_{\mathrm{I}}} = \frac{4}{w_{L,A}t}\cdot\frac{1}{\mathrm{e}^{-\mathrm{i}\tau}(\Delta_{11}\pm\Delta_{21}^*)(1+x_{\mathrm{L,A}})+\mathrm{e}^{\mathrm{i}\tau}(\Delta_{21}\pm\Delta_{11}^*)(1-x_{\mathrm{L,A}})}. \tag{7.19}$$

When the media A and L are the same (i.e., $w_{\mathrm{L,A}} = 1$ and $x_{\mathrm{L,A}} = 1$), this equation considerably simplifies:

$$\frac{E_F \pm E_B}{E_I} = \frac{2}{t} \cdot \frac{e^{i\tau}}{\Delta_{11} \pm \Delta_{21}^*}. \tag{7.20}$$

The field enhancement (enhancement of electric field for even modes or enhancement of the magnetic field for odd modes) is always inversely proportional to the transmittance t of the Bragg mirrors inside the forbidden band, i.e., the lower is the transmittance t of the Bragg mirrors, the stronger is the enhancement of the field in the middle of the defect.

The enhancement factor in this equation can be straightforwardly evaluated for a homogeneous defect layer:

$$\frac{1}{\Delta_{11} \pm \Delta_{21}^*} = \frac{1}{w_{D,L}} \cdot \frac{1}{\begin{bmatrix} 1 \\ x_{D,L} \end{bmatrix} \cos \dfrac{k_{y,D} d_D}{2} - i \begin{bmatrix} x_{D,L} \\ 1 \end{bmatrix} \sin \dfrac{k_{y,D} d_D}{2}} \tag{7.21}$$

For the opposite case (electric field of odd modes or magnetic field of even modes), Eq. (7.18) vanishes in the limit $t \to 0$ (band gap of the Bragg mirrors): A simple analysis shows that it is directly proportional to t.

Discussion

From a general point of view, Eqs. (7.15) offer the possibility of determining the frequencies of defect modes as soon as the parameters of the Bragg mirrors and of the defect are known. For a single-layer defect (Eq. (7.16)) it is necessary to know the physical properties of the defect, wave impedance of the medium surrounding the defect (layer L) and the frequency dependence of the phases ϱ and τ, determined either theoretically or experimentally [286–288]. Note that Eqs. (7.15) and (7.16) are general and that they were derived only with the assumption of a perfect reflection from the structure surrounding the defect ($r \to 1$). Hence a disordered PC can be described by these equations as well.

Note that if the structure depicted in Fig. 7.2 contains just a single-layer defect, it becomes in principle a Fabry–Pérot (FP) cavity embedded in a complex structure (Bragg mirrors). The terms φ and $\tilde{\varphi}$, respectively, that appear in Eqs. (7.16) add an extra phase shift as compared to a classical FP cavity enclosed in ideal metallic mirrors. These extra phase shifts account for the distributed reflection of the electromagnetic wave on the Bragg mirrors.

Tunability by optical thickness of the defect. We now discuss in detail the specific case, where a single-layer defect is surrounded by Bragg mirrors with elementary cells consisting of two layers of equal optical thickness (they are labeled as F and L, coherently with Fig. 7.2). Such a structure provides the highest possible ratio of the forbidden band width to its central frequency f_c [289]. For normal incidence, there are two substantial quantities that characterize such Bragg mirrors: (i) The optical thickness l_{tot} of a single period, which controls the central frequency f_c of the forbidden band, and (ii) the contrast of impedances of the constituents $x_{F,L} = z_L/z_F$ (Eq. (7.3)). The value

of $x_{\mathrm{F,L}}$ controls the phase shift κ appearing in Eq. (7.16) and thus strongly influences the properties of defect modes. One can verify that $\tan\kappa(f_{\mathrm{c}}) = 0$ for $x_{\mathrm{F,L}} > 1$ while $1/\tan\kappa(f_{\mathrm{c}}) = 0$ for $x_{\mathrm{F,L}} < 1$.

Following the values of $x_{\mathrm{D,L}}$ and $x_{\mathrm{F,L}}$, we can describe two qualitatively different behaviors of defect mode properties.

- For $x_{\mathrm{D,L}} \gg 1$ and $x_{\mathrm{F,L}} > 1$ ($z_{\mathrm{L}} \gg z_{\mathrm{D}}$ and $z_{\mathrm{L}} > z_{\mathrm{F}}$), the phase shift φ in Eq. (7.16a) becomes small. The defect modes thus approach those of the classical FP cavity surrounded by ideal metallic mirrors (dotted curves in Fig. 7.3a). Analogically, for $x_{\mathrm{D,L}} \ll 1$ and $x_{\mathrm{F,L}} < 1$ ($z_{\mathrm{L}} \ll z_{\mathrm{D}}$ and $z_{\mathrm{L}} < z_{\mathrm{F}}$), the phase shift $\tilde{\varphi}$ in Eq. (7.16b) becomes small and in turn, the defect modes again resemble to the modes of FP cavity (except the mode numbering and parity).

  In these cases, the defect mode can be tuned over the entire forbidden band. Moreover, if the defect optical thickness is sufficiently small ($\lesssim l_{\mathrm{tot}}$, i.e., $m = 0$ or $m = 1$), there is only a single defect mode in the entire tuning range (Fig. 7.3a).

  In the optical or in the THz region, the magnetic response of materials can be neglected, i.e., $z_j = 1/n_j$. The requirements on $x_{\mathrm{D,L}}$ and $x_{\mathrm{F,L}}$ are thus transformed to $n_{\mathrm{L}} \ll n_{\mathrm{D}}$ and $n_{\mathrm{L}} < n_{\mathrm{F}}$ or $n_{\mathrm{L}} \gg n_{\mathrm{D}}$ and $n_{\mathrm{L}} > n_{\mathrm{F}}$, which means that we arrange the layers in the PC to achieve the highest refractive index contrast between the defect and the adjacent layers.

- The behavior is more complicated for the remaining two cases which correspond to the arrangement of the lowest impedance contrast between the defect and the adjacent layers. Let us first examine the case $x_{\mathrm{F,L}} > 1$ and $x_{\mathrm{D,L}} \ll 1$ ($z_{\mathrm{L}} \ll z_{\mathrm{D}}$ and $z_{\mathrm{L}} > z_{\mathrm{F}}$). In turn, $\tan\kappa$ crosses zero for $f = f_{\mathrm{c}}$, i.e., the defect levels coincide with FP cavity modes $k_{y,\mathrm{D}}d_{\mathrm{D}} = \pi m$ without an additional phase shift for this particular frequency (Fig. 7.3a). However, immediately as $\tan\kappa$ becomes non-zero for $f = f_{\mathrm{c}} \pm \Delta f$, the phase shift φ tends to $\pm\pi/2$ because the value of $1/x_{\mathrm{D,L}}$ is high (see Eq. (7.16a)), i.e., $k_{y,\mathrm{D}}d_{\mathrm{D}} = (m \pm 1)\pi$. In other words, the m-th mode is attracted to the $m \pm 1$-st FP cavity mode for $f \neq f_{\mathrm{c}}$. This behavior is demonstrated by a dash-dotted curves in Fig. 7.3a. There is thus a wide range of optical thicknesses of defects for which the tunability is practically excluded (Figs. 7.3a and 7.3b), i.e., a large change in the optical thickness $n_{\mathrm{D}}d_{\mathrm{D}}$ of the defect is necessary to tune the defect-mode frequency in the vicinity of f_{c}. Similar discussion based on Eq. (7.16b) leads to analogical results for the last case where $x_{\mathrm{F,L}} < 1$ and $x_{\mathrm{D,L}} \gg 1$ ($z_{\mathrm{L}} \gg z_{\mathrm{D}}$ and $z_{\mathrm{L}} < z_{\mathrm{F}}$).

  The structures with parameters $x_{\mathrm{F,L}}$ and $x_{\mathrm{D,L}}$ discussed in this paragraph are thus of limited interest in applications requiring wide tunability.

We can also estimate the maximal relative tunability of defect modes by optical thickness (Eq. (7.17)). From Kramers-Kronig analysis [288] it can be shown that the derivative
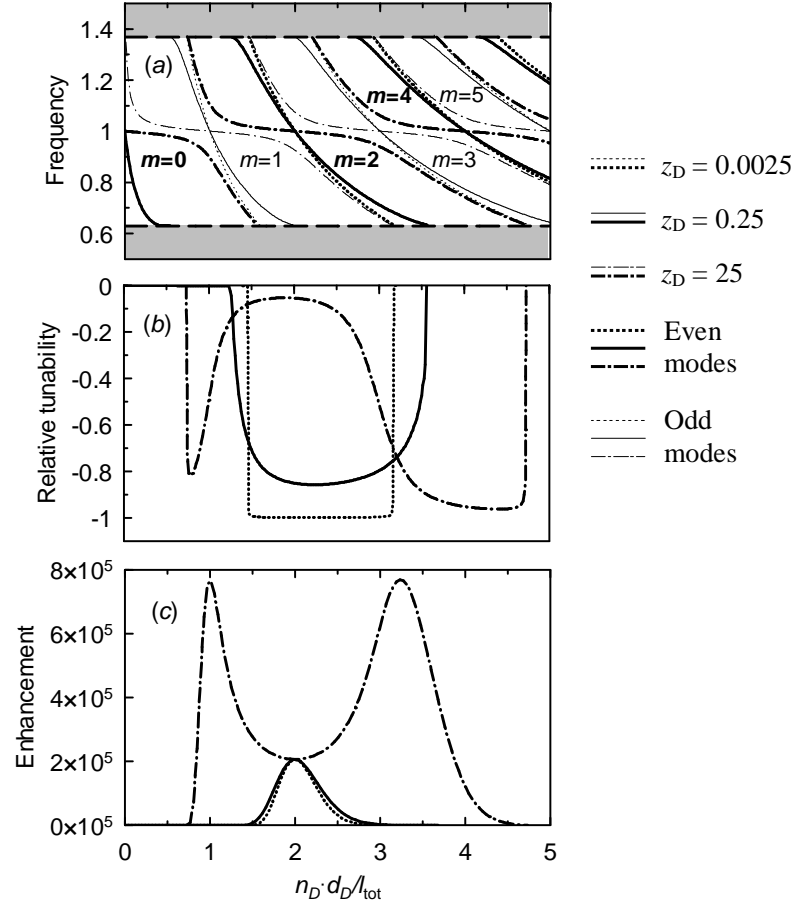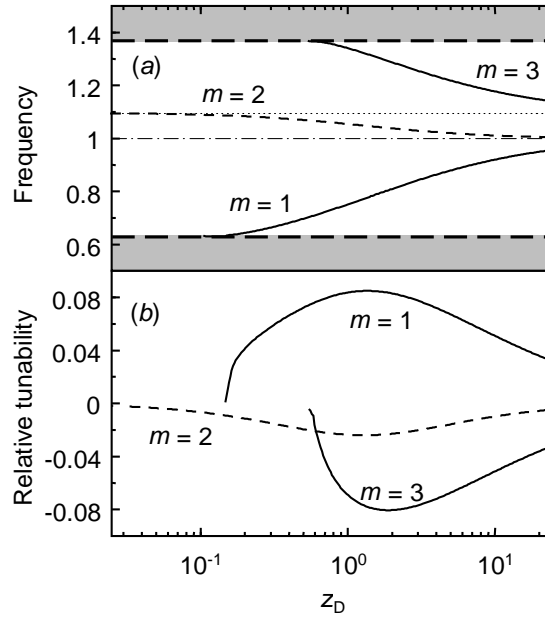
Figure 7.3: (a) Dimensionless frequency (in units of $c/(2l_{\mathrm{tot}})$; $l_{\mathrm{tot}} = n_F d_F + n_L d_L$) of defect modes, (b) their relative tunability by optical thickness, and (c) enhancement of the electric field in the middle of the defect versus optical thickness of the defect. Dashed lines in (a) indicate band edges; thicker curves, even-parity modes; and thinner curves, odd-parity modes. The calculations were made with $\theta = 0°$ and $z_D = 0.0025$ (dotted curves), $z_D = 0.25$ (solid curves), and $z_D = 25$ (dashed-dotted curves). Parameters of the PC are $n_F d_F = n_L d_L = l_{\mathrm{tot}}/2$, $z_F = 1/3.4$, and $z_L = z_A = 1$. Infinite Bragg mirrors ($N \to \infty$) are considered in (a) and (b) while Bragg mirrors composed of 10 periods are assumed in (c). For clarity, only modes with $m = 2$ are plotted in (b) and (c).

of $\varrho - 2\tau$ versus frequency is always negative, and consequently the maximum relative tunability by relative variation of optical thickness is limited by -1 (Fig. 7.3b). Such a situation occurs in two cases: $x_{D,L} \to 0$ ($z_D \to \infty$) and $x_{D,L} \to \infty$ ($z_D \to 0$). In the THz or optical range, these conditions can be translated into the requirement $n_D \to 0$ or $n_D \to \infty$. In practice, it is much simpler to find a material with high n_D than to find a material with $n_D < 1$.

Field enhancement. Enhancement of the electric field inside the defect is of great interest in conjunction with nonlinear phenomena in PCs [290, 291]. Because of the presence of the factor $1/t$ in Eq. (7.20), the electric field enhancement is proportional to the quality of the Bragg mirrors (e.g., it grows rapidly with the number of periods), whereas the factor $1/(\Delta_{11} \pm \Delta_{21}^*)$ stands for the enhancement that is due to the properties of the defect. For a single-layer defect (Eq. (7.21)) the magnitude of the latter enhancement factor may vary from $1/w_{\mathrm{D,L}}$ to $1/(w_{\mathrm{D,L}} x_{\mathrm{D,L}})$. The last term then causes an increase in the maximum enhancement when the impedance of the defect is larger than that of the last layer L (Fig. 7.3c). In contrast, for $n_{\mathrm{D}} d_{\mathrm{D}} = m l_{\mathrm{tot}}$ the enhancement factor does not depend any more on impedance z_{D} at normal incidence ($\theta_j = 0$ for all j).

Tunability by impedance of the defect. This mechanism of tunability is important in microwave devices where it is not difficult to vary the impedance of the defect [284]. As shown in Fig. 7.4, such tunability is an order of magnitude lower than that by optical thickness. Depending on the position in the bandgap with respect to f_{c}, the frequency of the defect modes either increases with impedance ($f < f_{\mathrm{c}}$) or decreases ($f > f_{\mathrm{c}}$). Indeed, the right-hand side of Eq. (7.16a) is a monotonic function of $x_{\mathrm{D,L}}$, increasing or decreasing according to the sign of $\tan \kappa$ and intersecting zero for $f = f_{\mathrm{c}}$. In the limit of
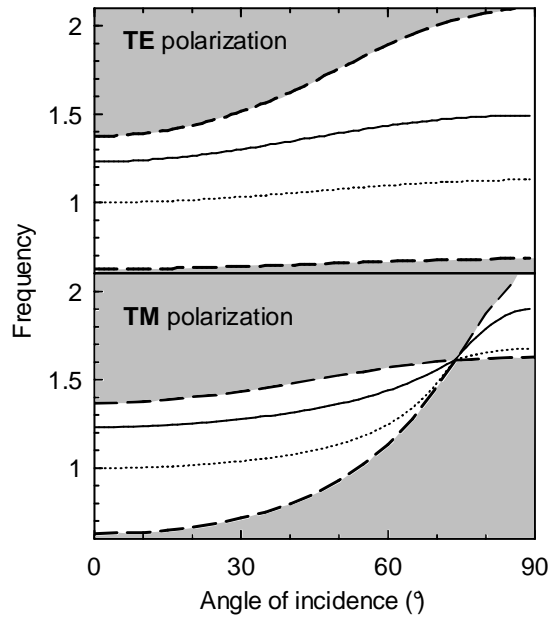

Figure 7.4: (a) Dimensionless frequency of defect modes and (b) their relative tunability by impedance $[(\mathrm{d}f/\mathrm{d}z_{\mathrm{D}}) \cdot z_{\mathrm{D}}/f]$ versus impedance of the defect. Long-dashed lines indicate band edges; Dashed-dotted curve, middle of the gap; dotted curve, asymptotic limits of defect levels when $z_{\mathrm{D}} \to 0$ ($m = 2$) or $z_{\mathrm{D}} \to \infty$ ($m = 3$). The calculations were performed with $n_{\mathrm{D}} d_{\mathrm{D}} = 1.824 l_{\mathrm{tot}}$ and $\theta = 0°$; other parameters are the same as in Fig. 7.3.

high impedance, the frequency of the m-th defect mode reaches asymptotically either f_c or mode $m - 1$ (for $f > f_c$) or $m + 1$ (for $f < f_c$) of a FP cavity without an additional phase shift. Both limits can be clearly seen in Fig. 7.3a when the optical thickness is kept constant while the impedance is varied. As shown in Fig. 7.4a, new defect modes arise in the bandgap with increasing impedance.

Tunability by rotation of the PC. Control of defect modes by rotating the PC may be easy to implement in some devices. However, the tunability is low for both polarizations at small angles of incidence, as can be seen from Fig. 7.5. TM polarization offers slightly better tunability at higher angles, but simultaneously with increasing angle the forbidden band gets narrower. The forbidden band disappears for the Brewster angle as there is no reflection on the interface between the layers L and F.

7.2 Spectroscopy of photonic crystals

In the vast majority of spectroscopic studies of PCs, only amplitude of transmittance or reflectance spectrum is measured. This is often sufficient as forbidden bands in PCs appear as frequency regions of suppressed transmittance or enhanced reflectance. However,


Figure 7.5: Dimensionless frequency of a defect mode as a function of angle of incidence θ on the PC. Dashed curves, band edges; dotted and solid curves, $n_D d_D = 0.735 l_{tot}$ and $n_D d_D = l_{tot}$, respectively. For both polarizations $z_D = 0.25$ and $n_A = 1$. Other parameters are the same as in Fig. 7.3.

reconstruction of the photonic band structure demands knowledge of the transmittance phase [184, 292, 293]. Further information is required for efficient modeling or testing PC circuits. For example, transmission properties of a multi-component PC circuit can be easily predicted on the basis of scattering matrices of individual components [294,295]. The scattering matrices of simple components with known internal structure can be calculated using numerical methods. However, it might be often difficult to determine the real internal structure or to carry out the calculations: In such a case, the scattering matrix can be still constructed from measured complex transmittance and reflectance spectra. As time-domain THz spectroscopy (TDTS) is able to provide both these spectra, it can yield an exhaustive information about PC components, making it possible to predict the properties of PC circuits built from them.

Here we investigate a simple PC structure consisting of two 1D PCs (Bragg mirrors) separated by an air layer with variable thickness (Fig. 7.6a). Such a structure can be regarded as a tunable FP cavity surrounded by Bragg mirrors, or as a PC with a twinning defect. In particular, we focus on formation of defect modes in this structure. We consider the PC to be composed of three individual components (building blocks): Two Bragg mirrors and a defect. Each of them can be separately characterized by the TDTS. From the measured complex transmittance and reflectance spectra of the Bragg mirrors we predict the frequencies of defect modes of the entire structure, without any reference to internal structure of the Bragg mirrors. For comparison, we construct and characterize the entire structure. Finally, we also demonstrate the determination of the photonic band-structure of a pure PC from complex transmittance spectra.

Theoretical description

For the theoretical description of the investigated PC structure, we take advantage of the transfer matrix formalism utilized in the previous section. This approach is appropriate as we are investigating 1D structures composed of alternating isotropic layers, and we deal with a single propagation mode. The transfer matrix $\mathbf{M}$ is thus a 2×2 matrix, and all the
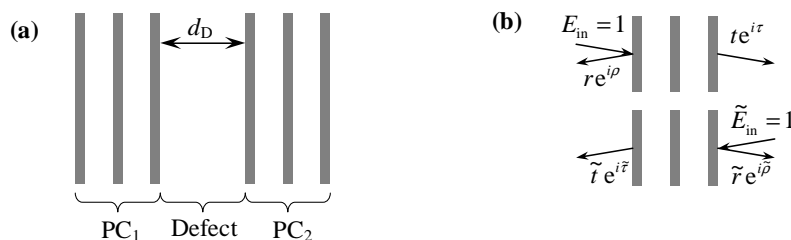
Figure 7.6: (a) Scheme of the investigated structure. (b) Definition of transmittance and reflectance spectra for measurements carried out on opposite sides of a building block.

fields are represented by a single scalar number, what makes the subsequent calculations as well as experiments particularly feasible. However, this approach remains valid also for any single-mode structure, like long PC waveguides [295].

Similarly as in the previous section, we assume that the constituting materials do not exhibit losses. In turn, the transfer matrix can be expressed in terms of complex transmittance and reflectance (Eq. (7.10)). In the derivation of Eq. (7.10), we took for granted that the incident wave impinges on the structure from the left-hand side, i.e., $E_{\mathrm{fwd}}^{\mathrm{L}} \equiv E_{\mathrm{in}}$ and $E_{\mathrm{bck}}^{\mathrm{R}} = 0$ (see Fig. 7.6b). However, the structure can be equivalently characterized by the complex transmittance $\tilde{t} \exp(\mathrm{i}\tilde{\tau})$ and reflectance $\tilde{r} \exp(\mathrm{i}\tilde{\varrho})$ measured when the incident wave impinges from the right-hand side ($E_{\mathrm{bck}}^{\mathrm{R}} = \tilde{E}_{\mathrm{in}}$ and $E_{\mathrm{fwd}}^{\mathrm{L}} = 0$). One can simply show that $\tilde{t} = t$, $\tilde{\tau} = \tau$, $\tilde{r} = r$ and $\tilde{\varrho} = 2\tau - \varrho + \pi$. The structure is thus completely characterized by a set of three spectral functions: t, τ, and ϱ ($t^2 + r^2 = 1$ due to the absence of losses).

The components of the PC structure (building blocks) can be simply measured only in vacuum or in air ($z = 1$). We thus need to express the transfer matrices in terms of reflectance and transmittance of components surrounded by vacuum (and not by the other parts of the structure). However, this is not a problem since one can easily show, that the transfer matrix of two such components (surrounded by the vacuum) put into optical contact is a pure product of transfer matrices corresponding to the individual components.

Now, we are ready to investigate defect modes in a structure composed of two PCs enclosing a single-layer defect (Fig. 7.6a). Depending on the optical thickness of the defect, the whole structure may exhibit a defect mode, i.e. a narrow range of frequencies in the forbidden band, for which the propagation through the structure is allowed. From the transfer matrix of the entire structure, one finds the following condition for the defect mode frequency in the limit of perfect PCs ($r_1 \to 1$ and $r_2 \to 1$):

$$\tilde{\varrho}_1 + \varrho_2 + 2\tau_{\mathrm{D}} = 2\pi m + 2 \arg[1 - r_{\mathrm{D}} \exp(\mathrm{i}\varrho_0)], \qquad (7.22)$$

where the subscripts 1, 2, and D refer to the PC$_1$, PC$_2$ and to the defect, respectively, m is an arbitrary integer, and

$$\varrho_0 = \varrho_{\mathrm{D}} + \tilde{\varrho}_1 = \varrho_2 + \tilde{\varrho}_{\mathrm{D}}. \qquad (7.23)$$

This last equality is automatically fulfilled at the defect mode frequencies. Eq. (7.22) represents in fact the resonance condition in a FP cavity: Constructive interference—or equivalently, the defect mode—appears if the total phase shift on a round-trip through the cavity (=phase shifts $\tilde{\varrho}_1$ and ϱ_2 due to the reflection on the Bragg mirrors PC$_1$ and PC$_2$ plus the phase shift owing to the propagation through the resonator—defect) equals to any multiple of 2π. The last term in Eq. (7.22) arises due to the fact that the resonator is formally enclosed between infinitesimally thin vacuum layers, e.g., $\tilde{\varrho}_1$ describes the reflectance phase for the incident wave coming from the vacuum and not from the defect medium. This term thus accounts for the impedance mismatch between the component and the vacuum. Note that this term disappears and τ_{D} reduces to $2\pi f d_{\mathrm{D}}/c$ when the defect

consists simply of a vacuum layer. Note also, that Eq. (7.22) is in fact a generalization of Eq. (7.16) ($\tau_\mathrm{D} = \omega n_\mathrm{D}/c$) for the case when the defect is surrounded by different structures from its left-hand and right-hand side.

Eq. (7.22) is not restricted to ideal periodic PCs: It can be applied to any structure exhibiting forbidden bands, like chirped structures, disordered systems or photonic quasicrystals [296, 297]. Conversely, Eq. (7.22) is not valid for frequencies belonging to allowed band of PC_1 or PC_2.

Experimental details

The Bragg mirrors (denoted as PC_1 and PC_2, Figs. 7.6a and 7.7a) were made of three $100\,\mu$m-thick commercially available high-resistivity silicon wafers ($\varrho > 1000\,\Omega \cdot$ cm, $\varnothing \sim 5$ cm) separated by two layers of air. These air layers were created by inserting small $350\,\mu$m-thick silicon spacers placed near the edges of the wafers. The structure was fixed by putting drops of glue on its edges. In the PC with the defect, these Bragg mirrors were separated by an air layer with thickness d_D varying from $50\,\mu$m to 1 mm. The exact thickness of the air layer was ensured by insertion of a silicon spacer with an appropriate thickness, and the entire structure was mechanically clamped together during measurements. Notice that the defect disappears for $d_\mathrm{D} = 350\,\mu$m: The resulting PC consisting of six silicon wafers does not have an impurity in its center for this particular value of d_D. This "pure" PC is used for band-structure reconstruction at the end of this section.

The THz experiments were made by use of setups described in sections 2.1 and 2.2. Long temporal scans (250 ps) were acquired for the study of the transmission functions of structures with defect in order to achieve frequency resolution about a few GHz (Eq. (1.1)). Better resolution can be hardly achieved. This is also the reason why we have utilized Bragg mirrors made only of three silicon layers: The defect spectral line would rapidly narrow with increasing number of periods.

Discussion

First of all, transmittance and reflectance spectra of the Bragg mirrors (PC_1 and PC_2) were measured using TDTS (Fig. 7.8). We can clearly observe the lowest five forbidden bands where the transmittance amplitude drops to few percents.

Though the internal structure of the Bragg mirrors is known from the fabrication protocol, the real structure is expected to be slightly different. In particular, the air layers are slightly thicker due to a penetration of the glue. In order to match the measured transmittance spectra, we had to adjust in all calculations the thicknesses of air layers to $370\,\mu$m for PC_1 and to $380\,\mu$m for PC_2.

Let us now analyze the structures where the Bragg mirrors PC_1 and PC_2 enclose the defect. An example of the transmittance spectrum with a $548\,\mu$m thick air-layer defect is plotted in Fig. 7.9. The defect modes can be identified as peaks in the spectrum at
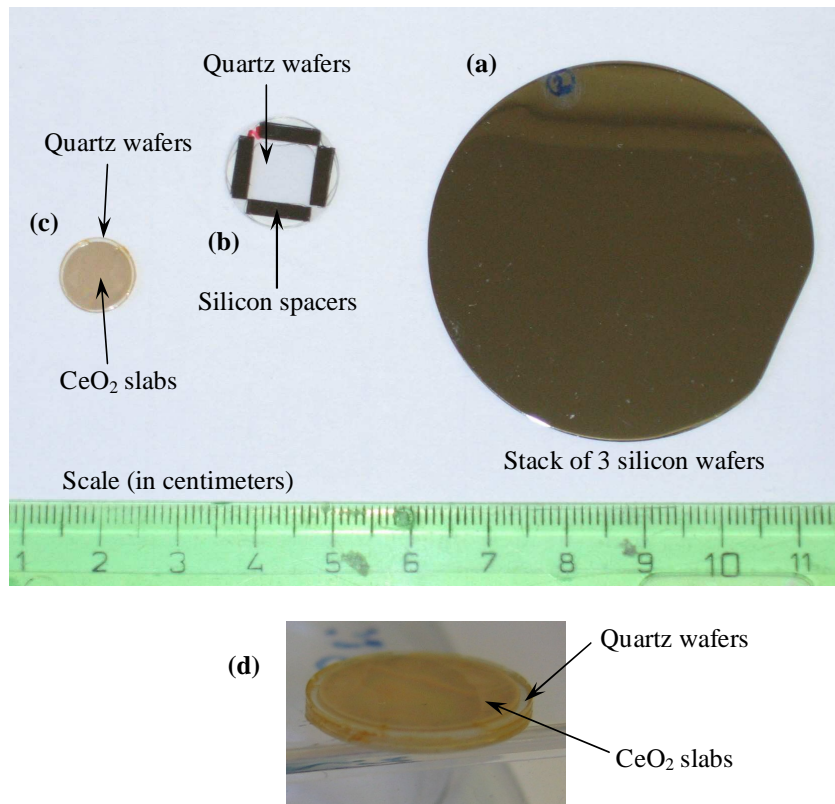
Figure 7.7: Photo of parts of PCs fabricated in the framework of this thesis. (a) Stack of 3 silicon wafers. (b) The Bragg mirror consisting of alternating layers of quartz and air. The air layers are created by insertion of silicon spacers (the spacers are visible in the photo). (c), (d) A top view and an enlarged side view of the Bragg mirror consisting of alternating layers of quartz and CeO_2 ceramics. In (d), one can resolve the three quartz wafers interleaved with the two smaller CeO_2 discs (beige).

252 GHz in the first forbidden band and at 586 THz in the second lowest forbidden band. The experimental peak transmittance at the defect level frequency is almost one order of magnitude lower than predicted by theory (equals to 1). This is mainly due to the low-frequency resolution of the TDTS (~ 4 GHz for 250 ps scans) while the calculated full width at half maximum of the defect level is ~ 1 GHz.

Fig. 7.10 summarizes the dependence of the defect mode frequency on the defect thickness for the two lowest forbidden bands. The points correspond to the frequencies of defect modes identified in the measured transmittance spectra. Solid curves show the predictions obtained from numerical calculations based on the knowledge of the internal structure of the PC. For Bragg mirrors consisting of only three periods, we have verified that the difference between the exact numerical solutions of the problem and the solutions
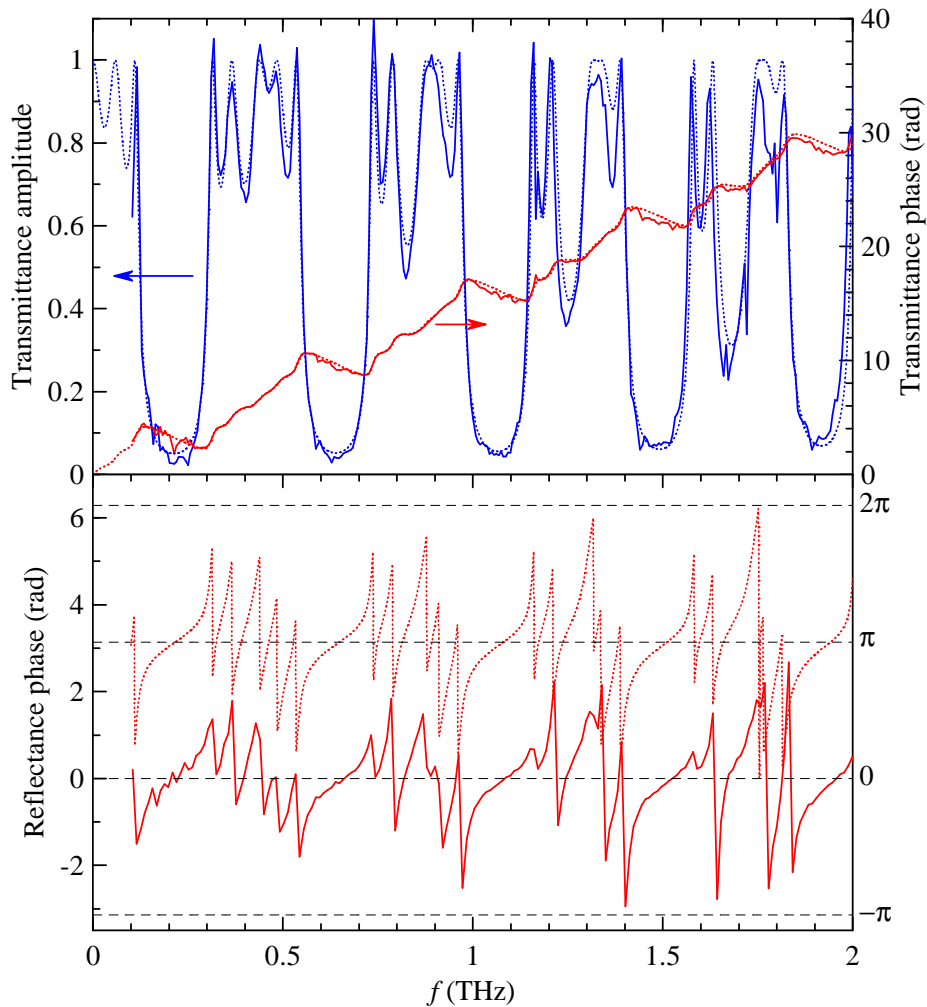
Figure 7.8: (a) Transmittance (amplitude and phase) and (b) reflectance (phase) spectra for one of the Bragg mirrors. The solid curves represent the measured data, whereas dotted curves correspond to theoretical calculations based on the knowledge of its internal structure. The solid curve in (b) is artificially shifted by $-\pi$ for graphical clarity.

of Eq. (7.22), for which we assume that $r_1 \to 1$ and $r_2 \to 1$, is negligibly small. Here again, the thickness of the defect layer has been slightly increased in the calculations (adjustment smaller than $50\,\mu$m compared to the nominal thickness of the spacers) in order to fit the experimental data. This can be simply understood in terms of the stress produced when the twins were clamped together. It is important to note that the thickness adjustment has been made just once for each defect thickness, leading to a very good fit of all the measured defect frequencies (e.g., three different frequencies for a $270\,\mu$m thick defect) with the prediction. Finally, the dashed curve indicates the prediction based on Eq. (7.22) and
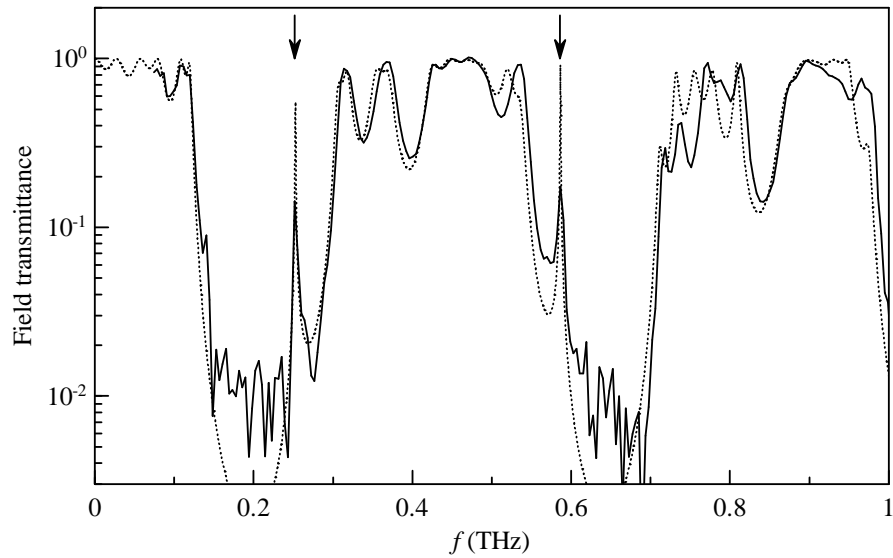
Figure 7.9: Transmittance spectrum of the PC with defect ($d_{\mathrm{D}} = 548\,\mu\mathrm{m}$). The dotted curve represents the theoretical calculations whereas the solid curve corresponds to experimental data. The arrows indicate the frequencies of defect modes.
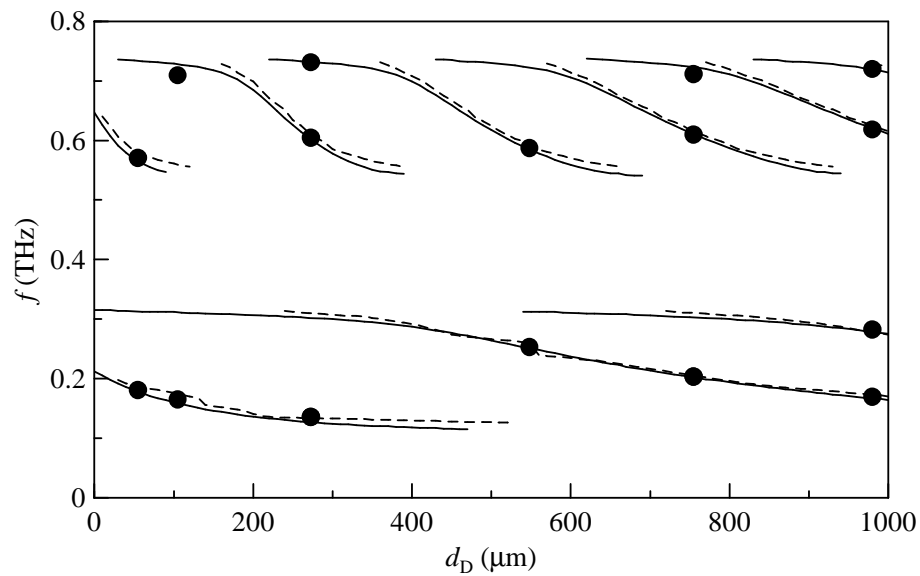
Figure 7.10: Frequency of defect modes versus defect layer thickness. Filled circles: measured data; solid curve: prediction based on the knowledge of the internal structure; dashed curves: prediction based on Eq. (7.22) and on measured reflectance phases.

on the experimentally obtained reflectance phases $\tilde{\varrho}_1$ and ϱ_2. It is necessary to emphasize that the setup for reflection measurements does not allow us to measure under strictly normal incidence (Sec. 2.2). However, measurements in our experimental conditions (with an incidence angle of 15° and in TM polarization) lead only to a minor systematic shift of the predicted frequencies as compared with the normal incidence. This shift corresponds to the difference between the solid and the dashed curves in Fig. 7.10. Larger differences are observed if the defect level lies near the edges of the forbidden band: The forbidden gap is in fact shifted to slightly higher frequencies with increasing incidence angle for TM polarization (Fig. 7.5).

The presence or absence of defect modes in the vicinity of the bandgap edges needs to be considered cautiously. As the transmittance of real PCs does not decrease steeply, the position of the edges is not well defined. In addition, the uncertainty of the position of band edges may be increased by possible small changes of the internal structure of the PCs owing to clamping. Hence the beginning and the ending of the lines predicting the frequency of defect modes (Fig. 7.10) is not well defined, and the defect modes identified in the measured transmittance spectra can be confused with the maxima outside the forbidden band.

Finally, we investigate the band structure of the PC without defect. The transmittance phase τ of a PC defines its effective refractive index n_{eff}, and thus it directly provides its dispersion relation, or equivalently, its band structure [184]:

$$k(\omega) = \frac{\omega n_{\text{eff}}}{c} = \frac{\tau(\omega)}{d}, \tag{7.24}$$

where d is the thickness of the investigated structure and k belongs to the first Brillouin zone. We used this expression for reconstruction of the band structure of the PC obtained by stacking Bragg mirrors PC_1 and PC_2 separated by a spacer 350 μm thick (such a PC does not contain the defect). In the graph in Fig. 7.11, we can observe two subsidiary forbidden bands around 415 and 840 GHz. These narrow forbidden bands originate from the small mismatch between the optical thicknesses of silicon wafers (341 μm) and air (370–380 μm). However, they could not be unambiguously resolved for Bragg mirrors consisting of three periods only (Fig. 7.8) due to small transmittance suppression.

7.3   Thermally tunable photonic crystals

The aim of this section is to design, fabricate and characterize PCs with defect modes tunable by temperature. The investigated structure is a 1D PC with a twinning defect, which was theoretically investigated in Sec. 7.1.

First, we summarize the guidelines for a design of a widely tunable structure. Maximum tunability is achieved if the optical thickness of the defect can be changed by the amount comparable to the central wavelength of the first forbidden band. However, at the same
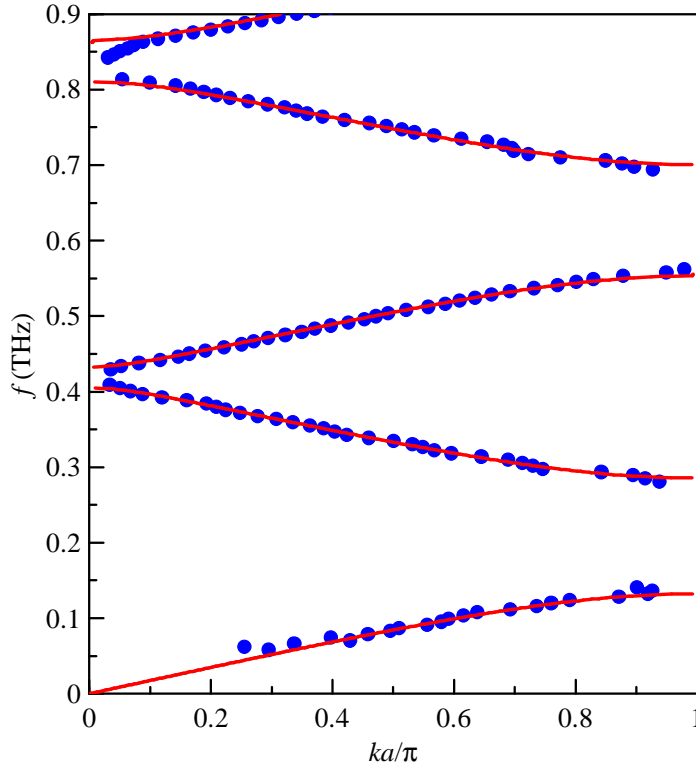
Figure 7.11: Dispersion relation of the studied PC without the defect. The circles are experimentally determined values for the stack PC_1+PC_2 separated by a $350\,\mu m$-thick spacer (i.e., a six-layer PC). The lines are theoretical predictions for an ideal (infinite) PC. Lattice period a of the PC is $475\,\mu m$.

time the value of the optical thickness of the defect must be kept small enough to prevent more than one defect mode from appearing in the forbidden band. The selected defect material thus should exhibit a large change of dielectric properties with temperature. The losses in the material should be as low as possible to simultaneously achieve a good peak transmittance and a high quality factor. Promising candidates with these properties are incipient ferroelectric crystals with a perovskite structure such as $KTaO_3$, $SrTiO_3$ or $CaTiO_3$; their dielectric properties can be varied over a large range by changing their temperature [298].

Here we use $KTaO_3$ and $SrTiO_3$ single crystals which satisfy the requirements stated above quite well. We measured their permittivity and loss tangent by use of TDTS. The results are shown in Fig. 7.12. The change of permittivity in the temperature range from 75 to $300\,K$ reaches nearly a factor of 4 and 7 for $KTaO_3$ and $SrTiO_3$ crystals, respectively, whereas the loss tangent remains lower than ~ 0.03 in this temperature range for both crystals.
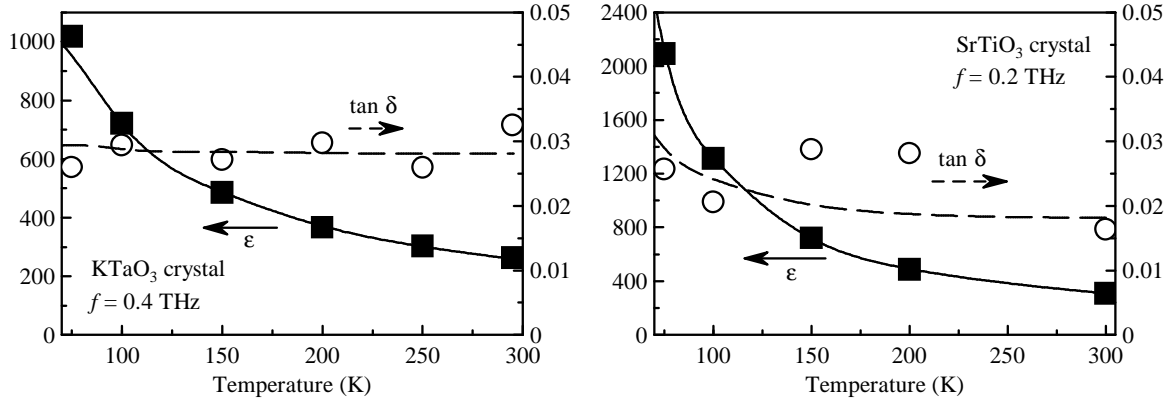
Figure 7.12: Temperature dependence of the permittivity (ε) and the loss tangent ($\tan\delta$) of KTaO$_3$ crystal (left panel) and SrTiO$_3$ crystal (right panel). The data were measured using TDTS at 0.4 THz (KTaO$_3$ crystal) and 0.2 THz (SrTiO$_3$ crystal).

The design of the structure enclosing the defect is also important for the performance of the filter. (i) The higher the reflectivity of the Bragg mirrors is, the narrower becomes the defect mode and the higher are the effective losses in the defect [299]. Consequently, Bragg mirrors with moderately high reflectivity constitute a good compromise between the high peak transmission and the width of the filter passband. (ii) The defect mode can be tuned only inside a forbidden band, i.e., wide forbidden band is essential to allow a wide tunability. In Bragg mirrors composed of two types of alternating layer (with refractive indices n_L and n_H; $n_L < n_H$), the width of the first forbidden band is maximal when the optical thicknesses of the layers are equal, i.e., $d_L n_L = d_H n_H$ [289]. (iii) The refractive index of incipient ferroelectrics is rather high ($n_D \gg n_L, n_H$). According to the discussion carried out in Sec. 7.1, the best tunability in such a case can be achieved when the defect is surrounded by n_L-layers (those with a lower refractive index).

We have fabricated and characterized two thermally tunable PCs, which differ primarily in the structure surrounding the defect. Different defect materials were used in the PCs, too: In the consecutive text, we will refer to the distinct PCs according to the material used for the defect.

Photonic crystal with the KTaO$_3$ defect

In the first structure that we have fabricated, air was used as the medium with the low refractive index (this is also the case of a vast majority of PCs operating in microwave and THz regions). For the medium with the high refractive index, we have used commercially available quartz wafers ($n_{\text{quartz}} = 2.10$). The defect was made of a thin KTaO$_3$ crystal. Such a crystal is very fragile, therefore it was necessary to clamp it between the quartz

wafers. As the defect is thus enclosed by a material with the high refractive index, the tunability of the structure is considerably limited (Sec. 7.1). (A different design of the PC which allows to lift this limitation will be presented in the next subsection).

The structure was constructed as follows. Each Bragg mirror (Fig. 7.7b) was fabricated using three $100\,\mu m$ thick wafers of quartz with a $15\,mm$ diameter. The individual wafers were separated by air layers, which were created by inserting $200\,\mu m$ thick silicon spacers placed near the edges of the quartz wafers. The Bragg mirrors were mechanically stabilized by drops of glue put on their edges. The $KTaO_3$ defect with a $7\,mm$ diameter, surrounded by a $50\,\mu m$ thick ring of a Mylar foil, was placed between the Bragg mirrors. Finally, the whole structure was fixed by miniature springs. The Mylar foil surrounding the defect is important for reducing the curvature of the PCs caused by the stress produced by the springs.
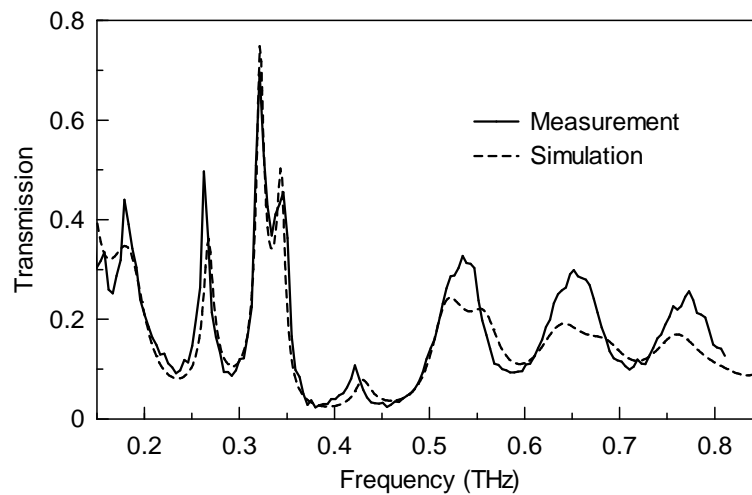
The transmittance of the PC was measured by means of TDTS in the second experimental setup described in detail in Sec. 2.1. Temporal scans of $150\,ps$ duration were acquired, yielding a frequency resolution of about $7\,GHz$, sufficient for the characterization of our PC. The transmittance spectra were measured in the temperature range from 120 to $290\,K$ with a step of $5\,K$. An ultralight copper holder has been used to achieve a rapid and homogeneous thermalization of the PC. The holder contains two heating elements and temperature sensors. The temperature adjustment is obtained with a differential-integral-proportional regulation and the obtained accuracy on the regulated temperature is estimated to be better than one-tenth of kelvin. The thermal time constant of the holder-PC set is of the order of a few tens of second leading to a 2–$3\,min$ regulation time necessary to achieve the next $5\,K$ temperature step.

The measured temperature-dependent transmittance spectra are summarized in Fig. 7.13a. Only the frequency region from 0.15 to $0.85\,THz$ is displayed: the apparatus is not sensitive enough at lower frequencies, mainly due to the presence of a $6\,mm$ diameter diaphragm in front of the PC. On the other hand, the higher-frequency components are strongly attenuated due to high absorption in the $KTaO_3$ crystal. Fig. 7.13b shows the results of a numerical simulation performed using the TMM discussed in Sec. 7.1. Both measured and numerically simulated transmission curves for $280\,K$ are shown in Fig. 7.14. In order to match the simulated data and the experimental results, we have considered $16\,\mu m$ thick air layers on both sides of the defect. This air gap probably originates from the curvature of the PCs created during their fabrication. The remaining differences between the measured and simulated spectra are only very minor: the small amplitude mismatch arises mainly due to the uncertainty of the defect losses entering the numerical simulation.

In Figs. 7.13 and 7.14, we can see the first forbidden band between 0.20 and $0.50\,THz$, where the intensity transmission is reduced by a factor exceeding 1000 in the upper part of the forbidden band. This forbidden band is significantly wider than that of an equivalent PC without the defect (0.28–$0.44\,THz$). This can be understood having in mind that the optical width of the defect is comparable to the optical length of the rest of the PC, i.e., the band structure is notably affected by the insertion of the defect.

(a) Measurement

(b) Simulation
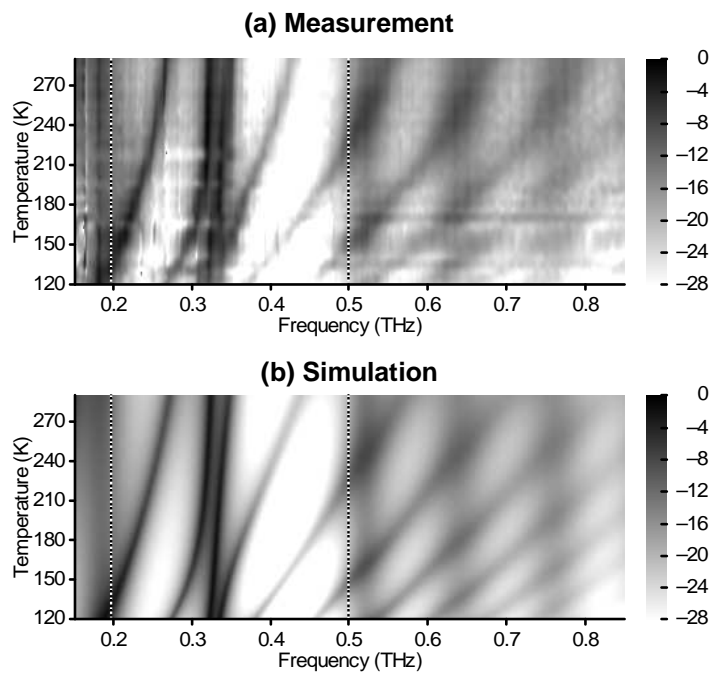
Figure 7.13: Transmittance (in decibels) of the PC with the KTaO$_3$ defect: (a) Experimentally determined data and (b) numerically simulated data. The two vertical lines indicate the edges of the first forbidden band.

Figure 7.14: Amplitude transmittance of the PC with the KTaO$_3$ defect at the temperature of 280 K. The measured data are indicated by a solid line while the numerical simulation is represented by a dashed line.

In the first forbidden band, there are five branches corresponding to distinct defect modes (Fig. 7.13). Except the defect mode near 340 GHz, the four other defect modes present a significant tunability. The lowest branch is of major interest due to its high peak transmission (about −6 dB). Its frequency varies from 267 GHz at 290 K down to 220 GHz at 170 K, i.e., its relative tunability reaches 20 %.

The pair of defect modes appearing near the center of the forbidden band exhibits a lack of tunability in a large temperature range, in accord with the behavior described in Sec. 7.1. This property reduces the tunability of the structure to less than a half of the forbidden band.

Photonic crystal with the SrTiO$_3$ defect

In order to significantly improve the tunability of the PC, the medium with the lower refractive index has to be adjacent to the defect layer. However, as the defect layers made of incipient ferroelectrics are very thin as a rule, they are also fragile and can be only hardly inserted between air layers created by spacers.

To overcome this problem, we used crystalline quartz wafers ($n_L = 2.10$) as the medium with the low refractive index. For the medium with the high refractive index, we employed a high-permittivity ceramic (undoped CeO$_2$, $n_H = 4.81$). The undoped CeO$_2$ ceramics has low losses in the THz range, and its permittivity exhibits only a very small temperature dependence [300]. The ratio of refractive indices is 2.3, which is even slightly higher than for the structure composed of a sequence of crystalline quartz and air layers examined above. The enhanced contrast n_H/n_L results in a wider forbidden band. It is also a remarkable feature that the resulting PC is compact, and thus less susceptible to a potential mechanical damage.

The fabrication procedure was similar as for the preceding PC. Each Bragg mirror Fig. 7.7c,d was assembled from three crystalline quartz wafers (thickness 230 μm) interleaved with two layers of CeO$_2$ ceramic (thickness 100 μm). The Bragg mirrors were fixed by drops of glue at the edges. The defect was made of a 41 μm thick SrTiO$_3$ single crystal. The entire structure was enclosed between two metallic apertures and tightened with small screws.

The transmittance of the sample was measured with a coherent source spectrometer (page 26 and Ref. [10]) in the frequency range 67–260 GHz and for temperatures from 75 to 295 K. The measured room-temperature transmittance of the structure is shown in Fig. 7.15a along with the result of a numerical simulation based on TMM and on an analytical fit of the dielectric properties of SrTiO$_3$ shown in Fig. 7.12. The lowest forbidden band spreads from 90 to 220 GHz; one can also identify a single defect mode at ∼ 185 GHz. Fig. 7.15b illustrates the frequency tuning of the defect mode with temperature for three different temperatures. Finally, in Fig. 7.16, the defect mode frequency is plotted versus temperature over the whole temperature range 100–300 K. The defect mode can be tuned from 185 GHz at room temperature down to 100 GHz at 100 K. The relative tunability,

calculated as the tuning range over the central frequency, reaches an outstanding value of 60 %. At the same time, the peak transmission always exceeds $-9\,\mathrm{dB}$ and the full width at half-maximum of the defect mode varies from 2.0 to 4.5 GHz. The small systematic shift between the measured and numerically calculated frequencies of the defect mode (Figs. 7.15a and 7.16) is attributed to the uncertainty of the structural parameters of the PC.
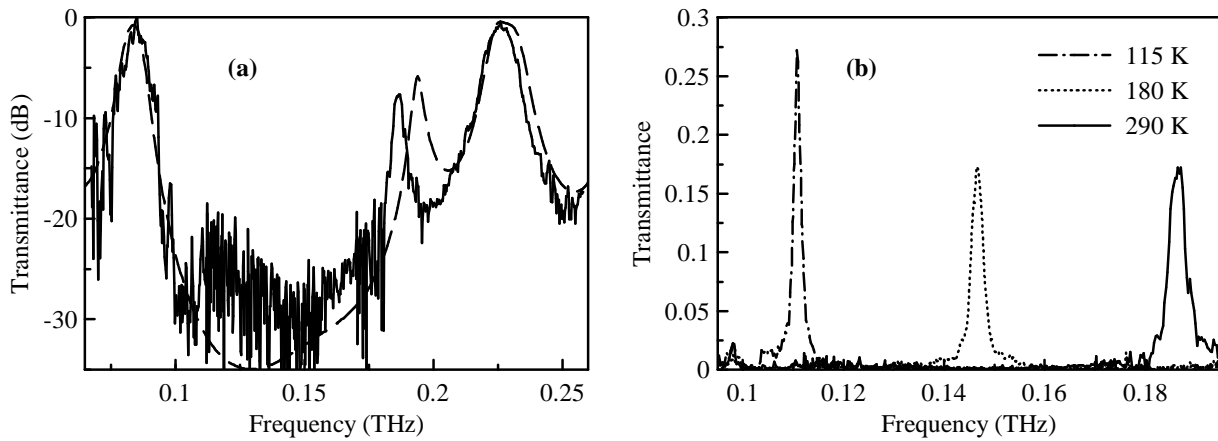
Figure 7.15: Power transmittance of the investigated structure. (a) Room temperature: solid curve, experiment; dashed curve, numerical simulation. (b) Typical spectra experimentally obtained in the tuning range.
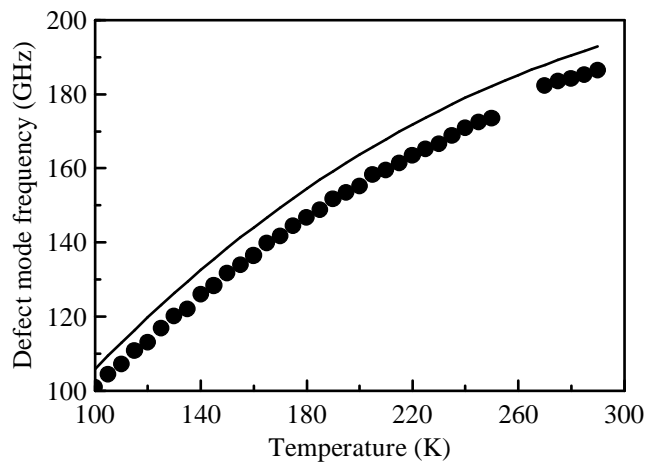
Figure 7.16: Tuning curve of the defect mode. Filled circles, measured defect frequency; solid curve, results of a numerical simulation.

7.4 Outlook

The demonstrated tuning range in our $SrTiO_3$-based PC can possibly be further extended if a slightly modified structure is used. The factor limiting our actual tuning range is the width of the forbidden band, which can be enhanced in multilayered structures by an increase in the ratio of refractive indices n_H/n_L [289]. For instance, plastics including TPX or Mylar can serve as n_L materials [10]. Then, in the temperature range 85–400 K it should be possible to achieve a tunability of 80 % (90–210 GHz).

The investigated PCs were designed to operate in the sub-THz range. Just by applying the scaling laws [189], one can construct analogous structures with appropriately scaled layer thicknesses for the gigahertz range. The real properties of such a structure may be effectively modified by a possible dielectric dispersion of the constituent materials. However, either quartz, silicon or CeO_2 do not show a dispersion of permittivity or important losses in the gigahertz and sub-THz ranges [10, 300]. In the case of $SrTiO_3$ and $KTaO_3$ the loss tangent scales nearly linearly with frequency, whereas their permittivity remains practically constant [301]. Consequently, the relative tuning range remains unaffected for structures designed for lower frequencies, whereas the peak transmission is expected to increase considerably. For example, scaling the PC with the $SrTiO_3$ defect by a factor of 10 would lead to a tuning range of 10.0–18.5 GHz with a peak transmission reaching -1.5 dB. Scaling it by only a factor of 3 would lead to a peak transmission greater than -4.6 dB.

Though the thermal control of PCs may be useful for certain applications not suffering from the low operating speed and low versatility, an electric or optical control of PCs has to be used to achieve a fast response of devices like modulators. This work makes a significant step toward such control as the influence of the applied electric field on the dielectric properties of ferroelectric crystals is quite similar to that of temperature [302].

In the following paragraphs, we will discuss the possibility of the electric control of the PC with the $SrTiO_3$ defect described in page 111. As the dielectric properties of quartz and CeO_2 ceramics are not altered neither by temperature, nor by the applied electric field, it is sufficient to find a model for the properties of $SrTiO_3$ in the applied electric field.

The static permittivity ($\varepsilon(f = 0)$) of ferroelectrics in electric field can be well described by the Landau's theory of ferroelectric transitions [303]:

$$\varepsilon_0\varepsilon(f = 0, T, E) = \frac{1}{\alpha + 3\beta P^2}, \tag{7.25}$$

where the coefficients α and β are the expansion coefficients of the free energy in terms of the macroscopic electric polarization P. The polarization P is related to the electric field E via

$$E = \alpha P + \beta P^3. \tag{7.26}$$

According to the common practice, we assume that the coefficient β is temperature independent. To account for the fact that the incipient ferroelectrics remain paraelectric to

the lowest temperatures, we use the Vendik's model for the coefficient α [304]:

$$\alpha(T) = \frac{T_{\mathrm{V}}}{C\varepsilon_0} \left(\sqrt{\frac{1}{16} + \frac{T^2}{T_{\mathrm{V}}^2}} - \frac{T_0}{T_{\mathrm{V}}} \right). \tag{7.27}$$

The values of the model parameters β, C, T_0 and T_{V} are summarized in Ref. [303] for $\mathrm{Ba}_x\mathrm{Sr}_{1-x}\mathrm{TiO}_3$ and KTaO_3 crystals. Here we concentrate on the SrTiO_3, for which $\beta = 6.89 \times 10^9\,\mathrm{J} \cdot \mathrm{C}^{-4} \cdot \mathrm{m}^{-5}$, $C = 8.6 \times 10^4$, $T_0 = 42\,\mathrm{K}$ and $T_{\mathrm{V}} = 175\,\mathrm{K}$. Following these parameters, we can calculate the real part of the permittivity as a function of the applied electric field and temperature (Fig. 7.17).

In order to simulate the optical properties of our structure, we need to know the complex permittivity of SrTiO_3 in the sub-THz spectral region. As we are working at frequencies well below the first optical phonon (which is at $\sim 1.7\,\mathrm{THz}$ in SrTiO_3 cooled to $T = 100\,\mathrm{K}$), we can with a fully sufficient degree of precision assume that the real part of permittivity at sub-THz frequencies matches the static one [305]. On the other hand, we neglect the imaginary part of the permittivity as its dependence on the applied electric field has not been investigated, up to our knowledge.

The results of simulations based on these assumptions and on Eqs. (7.25)–(7.27) are plotted in Fig. 7.18 for two temperatures. From the point of view of potential applications, it is desirable to operate the structure at room temperature. In such a case, a crystal with thickness $d_{\mathrm{D}} \sim 55\,\mu\mathrm{m}$ has to be used to obtain a single defect mode approximately in the center of the forbidden band; the corresponding relative tunability being about $2\,\%$. The tunability can be improved by cooling down the structure. Note that the permittivity of the SrTiO_3 crystal becomes higher, requiring to use a thinner crystal. For temperature $150\,\mathrm{K}$ and defect thickness $\sim 40\,\mu\mathrm{m}$, the relative tunability reaches $17\,\%$.
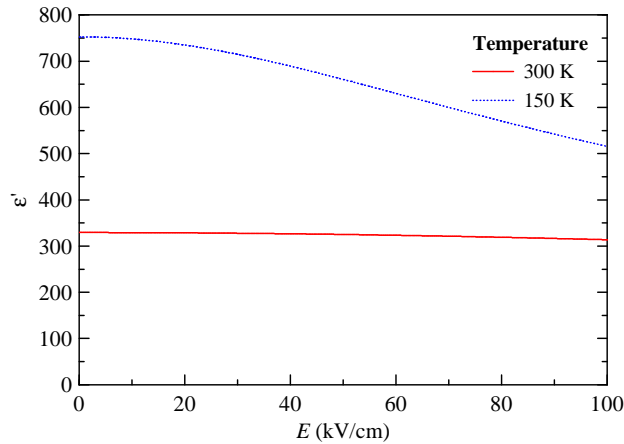
Figure 7.17: Model for the real part of static permittivity of a SrTiO_3 crystal as a function of the applied electric field.
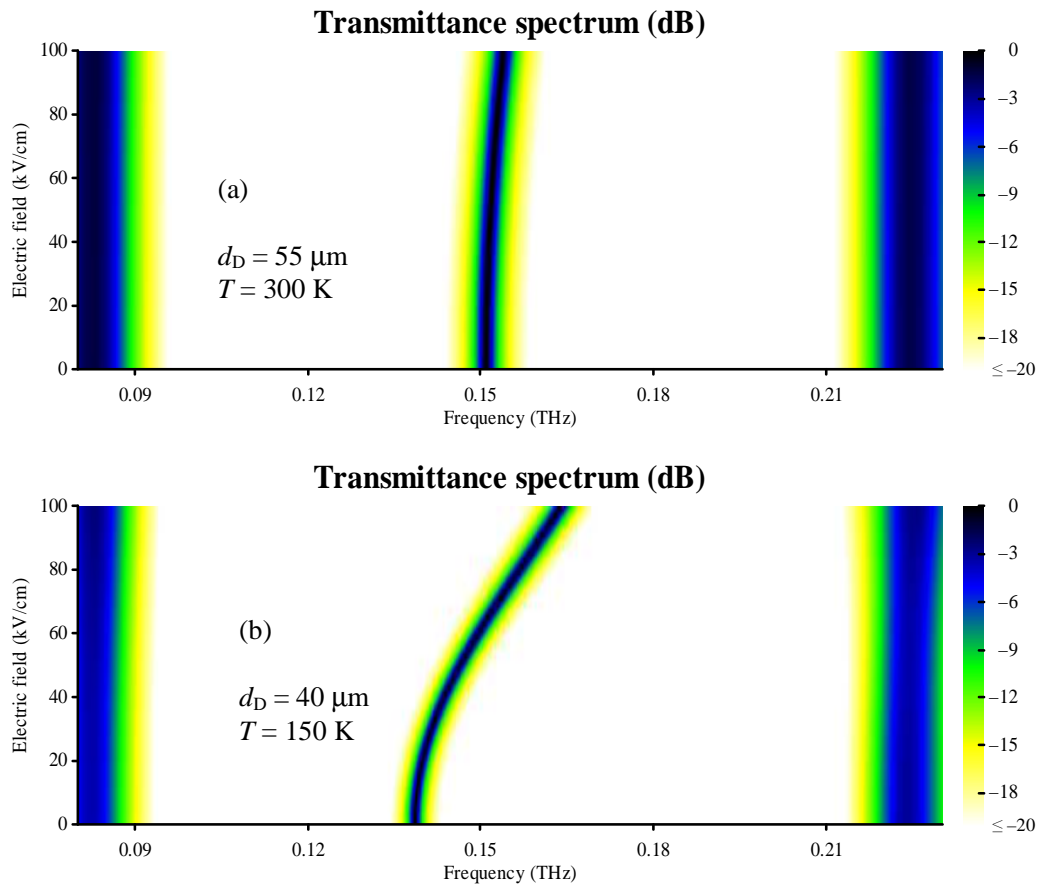
Figure 7.18: Numerical simulation of transmittance spectra of the electrically tunable PC with SrTiO₃ defect. The simulation was performed for temperatures 300 K (a) and 150 K (b). In both cases, such a thickness of the defect layer was chosen to obtain a single defect mode in the center of the forbidden band (around 150 GHz).

Conclusion

Two wide fields of optics have been combined in this thesis: Time-domain terahertz spectroscopy, and photonic crystals. The work thus naturally contains bibliographical research on these two subjects (chapters 1, 2, 4, and 5). Its main original contribution then consists in several results, most of them having been published or accepted for publication in international peer-reviewed journals (Refs. [285, 288, 306–308]):

1. We have proposed and demonstrated three approaches for simultaneous determination of the dielectric and magnetic functions from the transmittance and reflectance spectra measured by time-domain terahertz spectroscopy (Chap. 3). All these methods take advantage of the phase sensitivity and of the possibility of temporal windowing of time-domain terahertz spectroscopy. They have several characteristics in common, especially the possibility of an accurate determination of the complex refractive index and a less accurate determination of the complex wave impedance. We have also shown that these methods can be applied to characterization of both classical materials and metamaterials exhibiting complex behavior of dielectric and magnetic functions.

2. A periodically modulated dielectric waveguide (diffraction grating) has been studied theoretically using a modal method and a transfer matrix method (Chap. 6). The transfer matrix method served primarily for simulations of transmittance and reflectance spectra, and enabled a direct comparison of theoretical calculations and recently published experimental results. Additionally, it provided an indirect access to the band structure of guided modes of the waveguide. A direct calculation of the band structure has been performed using a modal approach: This allowed us to identify true guided modes and leaky modes as well as to describe resonant modes which are analogical to modes of a Fabry-Pérot resonator.

3. Systematic exploration of photonic structures is mostly dependent on the existence and development of numerical methods for calculations of their properties, notably of their transmittance and reflectance spectra and of their band structure. A part of this work is devoted to a detailed description of the transfer matrix method for simulating optical properties of one, two and three dimensional periodic structures (Chap. 5). A code of a numerical program based on this method has been written in the frame of this work. Using this code, we have calculated the spectra of a metamaterial described in Sec. 3.4 and the spectra of the diffraction grating investigated in Chap. 6.

4. We have investigated both experimentally and theoretically one-dimensional photonic crystals with a twinning defect, with a special regard to the design of a photonic crystal with a widely tunable defect mode which can act as a tunable spectral filter in the terahertz range (Chap. 7). In particular, we have analyzed the relation

between the structural parameters of the photonic crystal and frequency of the defect mode. We have formulated a set of guidelines for the design of the structure and for the choice of the defect material. Based on these criteria, we have designed, fabricated and characterized a structure with a relative tunability of its defect mode reaching 60 %.

References

[1] D. H. Auston, K. P. Cheung, and P. R. Smith. Picosecond photoconducting Hertzian dipoles. *Appl. Phys. Lett.* **45**, 284 (1984).

[2] E. Yablonovitch. Inhibited spontaneous emission in solid-state physics and electronics. *Phys. Rev. Lett.* **58**, 2059 (1987).

[3] V. G. Veselago. The electrodynamics of substances with simultaneously negative values of ϵ and μ. *Sov. Phys. Usp.* **10**, 509 (1968).

[4] J. B. Pendry, A. J. Holden, D. J. Robbins, and W. J. Stewart. Magnetism from conductors and enhanced nonlinear phenomena. *IEEE Trans. Microwave Theory Tech.* **47**, 2075 (1999).

[5] H. Eisele and G. I. Haddad. Two-terminal millimeter-wave sources. *IEEE Trans. Microwave Theory Tech.* **46**, 739 (1998).

[6] R. J. Trew. High-frequency solid-state electronic devices. *IEEE Trans. Electron Devices* **52**, 638 (2005).

[7] M. F. Kimmitt. In *Conference Digest of the 2004 Joint 29th International Conference on Infrared and Millimeter Waves and 12th International Conference on Terahertz Electronics*, 69–70 (2004).

[8] C. Fattinger and D. Grischkowsky. Terahertz beams. *Appl. Phys. Lett.* **54**, 490 (1989).

[9] D. Grischkowsky, S. Keiding, M. van Exter, and C. Fattinger. Far-infrared time-domain spectroscopy with terahertz beams of dielectrics and semiconductors. *J. Opt. Soc. Am. B* **7**, 2006 (1990).

[10] G. Grüner. *Millimeter and Submillimeter Wave Spectroscopy of Solids*. Springer-Verlag, Berlin, Heidelberg (1998).

[11] D. M. Mittleman, S. Hunsche, L. Boivin, and M. C. Nuss. T-ray tomography. *Opt. Lett.* **22**, 904 (1997).

[12] C. Zandonella. T-ray specs. *Nature* **424**, 721 (2003).

[13] C. A. Schmuttenmaer. Exploring dynamics in the far-infrared with terahertz spectroscopy. *Chem. Rev.* **104**, 1759 (2004).

[14] Y. Pastol, G. Arjavalingam, J.-M. Halbout, and G. V. Kopcsay. Coherent broadband microwave spectroscopy using picosecond optoelectronic antennas. *Appl. Phys. Lett.* **54**, 307 (1989).

[15] A. Leitenstorfer, S. Hunsche, J. Shah, M. C. Nuss, and W. H. Knox. Detectors and sources for ultrabroadband electro-optic sampling: Experiment and theory. *Appl. Phys. Lett.* **74**, 1516 (1999).

[16] R. Huber, C. Kübler, S. Tübel, A. Leitenstorfer, Q. T. Vu, H. Haug, F. Köhler, and M.-C. Amann. Femtosecond formation of coupled phonon-plasmon modes in InP: Ultrabroadband THz experiment and quantum kinetic theory. *Phys. Rev. Lett.* **94**, 02 7401 (2005).

[17] P. R. Smith, D. H. Auston, and M. C. Nuss. Subpicosecond photoconducting dipole antennas. *IEEE J. Quantum Electron.* **24**, 255 (1988).

[18] M. van Exter, C. Fattinger, and D. Grischkowsky. High brightness terahertz beams with an ultrafast detector. *Appl. Phys. Lett.* **55**, 337 (1989).

[19] M. van Exter and D. Grischkowsky. Optical and electronic properties of doped silicon from 0.1 to 2 THz. *Appl. Phys. Lett.* **56**, 1694 (1990).

[20] J. T. Darrow, B. B. Hu, X.-C. Zhang, and D. H. Auston. Subpicosecond electromagnetic pulses from large-aperture photoconducting antennas. *Opt. Lett.* **15**, 323 (1990).

[21] B. B. Hu, J. T. Darrow, X.-C. Zhang, D. H. Auston, and P. R. Smith. Optically steerable photoconducting antennas. *Appl. Phys. Lett.* **56**, 886 (1990).

[22] J. T. Darrow, X.-C. Zhang, and D. H. Auston. Power scaling of large-aperture photoconducting antennas. *Appl. Phys. Lett.* **58**, 25 (1991).

[23] J. T. Darrow, X.-C. Zhang, D. H. Auston, and J. D. Morse. Saturation properties of large-aperture photoconducting antennas. *IEEE J. Quantum Electron.* **28**, 1607 (1992).

[24] P. K. Benicewicz and A. J. Taylor. Scaling of terahertz radiation from large-aperture biased InP photoconductors. *Opt. Lett.* **18**, 1332 (1993).

[25] P. U. Jepsen, R. H. Jacobsen, and S. R. Keiding. Generation and detection of terahertz pulses from biased semiconductor antennas. *J. Opt. Soc. Am. B* **13**, 2424 (1996).

[26] K. Liu, A. Krotkus, K. Bertulis, J. Xu, and X.-C. Zhang. Terahertz radiation from *n*-type GaAs with Be-doped low-temperature-grown GaAs surface layers. *J. Appl. Phys.* **94**, 3651 (2003).

[27] M. Reid and R. Fedosejevs. Quantitative comparison of terahertz emission from (100) InAs surfaces and a GaAs large-aperture photoconductive switch at high fluences. *Appl. Opt.* **44**, 149 (2005).

[28] X.-C. Zhang, B. B. Hu, J. T. Darrow, and D. H. Auston. Generation of femtosecond electromagnetic pulses from semiconductor surfaces. *Appl. Phys. Lett.* **56**, 1011 (1990).

[29] X.-C. Zhang and D. H. Auston. Optoelectronic measurement of semiconductor surfaces and interfaces with femtosecond optics. *J. Appl. Phys.* **71**, 326 (1992).

[30] S. Izumida, S. Ono, Z. Liu, H. Ohtake, and N. Sarukura. Spectrum control of THz radiation from InAs in a magnetic field by duration and frequency chirp of the excitation pulses. *Appl. Phys. Lett.* **75**, 451 (1999).

[31] R. Adomavičius, A. Urbanowicz, G. Molis, A. Krotkus, and E. Šatkovskis. Terahertz emission from *p*-lnAs due to the instantaneous polarization. *Appl. Phys. Lett.* **85**, 2463 (2004).

[32] J. N. Heyman, P. Neocleous, D. Hebert, P. A. Crowell, T. Müller, and K. Unterrainer. Terahertz emission from GaAs and InAs in a magnetic field. *Phys. Rev. B* **64**, 08 5202 (2001).

[33] A. Corchia, R. McLaughlin, M. B. Johnston, D. M. Whittaker, D. D. Arnone, E. H. Linfield, A. G. Davies, and M. Pepper. Effects of magnetic field and optical fluence on terahertz emission in gallium arsenide. *Phys. Rev. B* **64**, 20 5204 (2002).

[34] S.-G. Park, M. R. Melloch, and A. M. Weiner. Comparison of terahertz waveforms measured by electro-optic and photoconductive sampling. *Appl. Phys. Lett.* **73**, 3184 (1998).

[35] F. G. Sun, G. A. Wagoner, and X.-C. Zhang. Measurement of free-space terahertz pulses via long-lifetime photoconductors. *Appl. Phys. Lett.* **67**, 1656 (1995).

[36] S. Kono, M. Tani, P. Gu, and K. Sakai. Detection of up to 20 THz with a low-temperature-grown GaAs photoconductive antenna gated with 15 fs light pulses. *Appl. Phys. Lett.* **77**, 4104 (2000).

[37] M. Tani, K. Sakai, and H. Mimura. Ultrafast photoconductive detectors based on semi-insulating GaAs and InP. *Jpn. J. Appl. Phys.; Part 2* **36**, L1175 (1997).

[38] J.-L. Coutaz. Semiconductor materials for ultrafast photoswitches. *Acta Phys. Pol. A* **102**, 495 (2002).

[39] M. Bass, P. A. Franken, J. F. Ward, and G. Weinreich. Optical rectification. *Phys. Rev. Lett.* **9**, 446 (1962).

[40] A. Nahata, A. S. Weling, and T. F. Heinz. A wideband coherent terahertz spectroscopy system using optical rectification and electro-optic sampling. *Appl. Phys. Lett.* **69**, 2321 (1996).

[41] L. Xu, X. C. Zhang, and D. H. Auston. Terahertz beam generation by femtosecond optical pulses in electrooptic materials. *Appl. Phys. Lett.* **61**, 1784 (1992).

[42] K. Reimann, R. P. Smith, A. M. Weiner, T. Elsaesser, and M. Woerner. Direct field-resolved detection of terahertz transients with amplitudes of megavolts per centimeter. *Opt. Lett.* **28**, 471 (2003).

[43] X.-C. Zhang, Y. Jin, and X. F. Ma. Coherent measurement of THz optical rectification from electro-optic crystals. *Appl. Phys. Lett.* **61**, 2764 (1992).

[44] X.-C. Zhang, Y. Jin, K. Yang, and L. J. Schowalter. Resonant nonlinear susceptibility near the GaAs band gap. *Phys. Rev. Lett.* **69**, 2303 (1992).

[45] A. Rice, Y. Jin, X. F. Ma, , X.-C. Zhang, D. Bliss, J. Larkin, and M. Alexander. Terahertz optical rectification from ⟨110⟩ zinc-blende crystals. *Appl. Phys. Lett.* **64**, 1324 (1994).

[46] X.-C. Zhang, X. F. Ma, Y. Jin, T.-M. Lu, E. P. Boden, P. D. Phelps, K. R. Stewart, and C. P. Yakymyshyn. Terahertz optical rectification from a nonlinear organic crystal. *Appl. Phys. Lett.* **61**, 3080 (1992).

[47] H. Hashimoto, H. Takahashi, T. Yamada, K. Kuroyanagi, and T. Kobayashi. Characteristics of the terahertz radiation from single crystals of *N*-substituted 2-methyl-4-nitroaniline. *J. Phys.: Cond. Matt.* **13**, 529 (2001).

[48] D. H. Auston, K. P. Cheung, J. A. Valdmanis, and D. A. Kleinman. Cherenkov radiation from femtosecond optical pulses in electro-optic media. *Phys. Rev. Lett.* **53**, 1555 (1984).

[49] F. C. A. Pockels. *Abhand. d. Ges. d. Wiss. zu Göttingen, Math. Phys. Klasse* **39**, 1 (1893).

[50] Q. Wu and X.-C. Zhang. 7 terahertz broadband GaP electro-optic sensor. *Appl. Phys. Lett.* **70**, 1784 (1997).

[51] P. Y. Han, , M. Tani, F. Pan, and X.-C. Zhang. Use of the organic crystal DAST for terahertz beam applications. *Opt. Lett.* **25**, 675 (2000).

[52] P. U. Jepsen, C. Winnewisser, M. Schall, V. Schyja, S. R. Keiding, and H. Helm. Detection of THz pulses by phase retardation in lithium tantalate. *Phys. Rev. E* **53**, 3052 (1996).

[53] C. Winnewisser, P. U. Jepsen, M. Schall, V. Schyja, and H. Helm. Electro-optic detection of THz radiation in LiTaO$_3$, LiNbO$_3$ and ZnTe. *Appl. Phys. Lett.* **70**, 3069 (1997).

[54] Z. Jiang, F. G. Sun, Q. Chen, and X.-C. Zhang. Electro-optic sampling near zero optical transmission point. *Appl. Phys. Lett.* **74**, 1191 (1999).

[55] Z. G. Lu, P. Campbell, and X.-C. Zhang. Free-space electro-optic sampling with a high-repetition-rate regenerative amplified laser. *Appl. Phys. Lett.* **71**, 593 (1997).

[56] Z. Jiang and X.-C. Zhang. Electro-optic measurement of THz field pulses with a chirped optical beam. *Appl. Phys. Lett.* **72**, 1945 (1998).

[57] S. L. Chuang, S. Schmitt-Rink, B. I. Greene, P. N. Saeta, and A. F. J. Levi. Optical rectification at semiconductor surfaces. *Phys. Rev. Lett.* **68**, 102 (1992).

[58] A. Y. Elezzabi and M. R. Freeman. Ultrafast magneto-optic sampling of picosecond current pulses. *Appl. Phys. Lett.* **68**, 3546 (1996).

[59] J. A. Riordan, F. G. Sun, Z. G. Lu, and X.-C. Zhang. Free-space transient magneto-optic sampling. *Appl. Phys. Lett.* **71**, 1452 (1997).

[60] F. Kadlec, P. Kužel, and J.-L. Coutaz. Optical rectification at metal surfaces. *Opt. Lett.* **29**, 2674 (2004).

[61] D. J. Hilton, R. D. Averitt, C. A. Meserole, G. L. Fisher, D. J. Funk, J. D. Thompson, and A. J. Taylor. Terahertz emission via ultrashort-pulse excitation of magnetic metal films. *Opt. Lett.* **29**, 1805 (2004).

[62] F. Kadlec, P. Kužel, and J.-L. Coutaz. Study of terahertz radiation generated by optical rectification on thin gold films. *Opt. Lett.* **30**, 1402 (2005).

[63] P. Y. Han, M. Tani, M. Usami, S. Kono, R. Kersting, and X.-C. Zhang. A direct comparison between terahertz time-domain spectroscopy and far-infrared Fourier transform spectroscopy. *J. Appl. Phys.* **89**, 2357 (2001).

[64] A. Pashkin. *Terahertz spectroscopy of ferroelectrics and related materials*. Ph.D. thesis, Faculty of Mathematics and Physics, Charles University in Prague (2004).

[65] P. Goy, M. Gross, S. Caroopen, and L. Noel. In O. Portugall and J. Leotin, eds., *Proceedings of the 26th International Conference on Infrared and Millimeter Waves IRMMW 2001*, 4.46–4.48 (2001).

[66] AB Millimetre. *MVNA-8-350 vector network analyzer*. URL: http://www.abmillimetre.com.

[67] P. Goy, M. Gross, S. Caroopen, and L. Noel. In *28th International Conference on Infrared and Millimeter Waves IRMMW 2003* (2003).

[68] N. Zamdmer, Q. Hu, K. A. McIntosh, S. Verghese, and A. Förster. On-chip frequency-domain submillimeter-wave transceiver. *Appl. Phys. Lett.* **75**, 3877 (1999).

[69] A. Borak. Toward bridging the terahertz gap with silicon-based lasers. *Science* **308**, 638 (2005).

[70] K. A. McIntosh, E. R. Brown, K. B. Nichols, O. B. McMahon, W. F. DiNatale, and T. M. Lyszczarz. Terahertz photomixing with diode lasers in low-temperature-grown GaAs. *Appl. Phys. Lett.* **67**, 3844 (1995).

[71] S. Verghese, K. A. McIntosh, and E. R. Brown. Optical and terahertz power limits in the low-temperature-grown GaAs photomixers. *Appl. Phys. Lett.* **71**, 2743 (1997).

[72] A. S. Pine, R. D. Suenram, E. R. Brown, and K. A. McIntosh. A terahertz photomixing spectrometer: application to SO_2 self broadening. *J. Mol. Spectr.* **175**, 37 (1996).

[73] S. Matsuura, M. Tani, H. Abe, K. Sakai, H. Ozeki, and S. Saito. High-resolution terahertz spectroscopy by a compact radiation source based on photomixing with diode lasers in a photoconductive antenna. *J. Mol. Spectr.* **187**, 97 (1998).

[74] G. Mouret, S. Matton, R. Bocquet, F. Hindle, E. Peytavit, J. Lampin, and D. Lippens. Far-infrared cw difference-frequency generation using vertically integrated and planar low temperature grown GaAs photomixers: application to H_2S rotational spectrum up to 3 THz. *Appl. Phys. B* **79**, 725 (2004).

[75] P. Gu, F. Chang, M. Tani, K. Sakai, and C. L. Pan. Generation of coherent cw-terahertz radiation using tunable dual-wavelength external cavity laser diode. *Jpn. J. Appl. Phys.; Part 2* **38**, L1246 (1999).

[76] J. Faist, F. Capasso, D. L. Sivco, C. Sirtori, A. L. Hutchinson, and A. Y. Cho. Quantum cascade laser. *Science* **264**, 553 (1994).

[77] R. Köhler, A. Tredicucci, F. Beltram, H. E. Beere, E. H. Linfield, A. G. Davies, D. A. Ritchie, R. C. Iotti, and F. Rossi. Terahertz semiconductor-heterostructure laser. *Nature* **417**, 156 (2002).

[78] D. C. Larrabee, G. A. Khodaparast, F. K. Tittel, J. Kono, G. Scalari, L. Ajili, J. Faist, H. Beere, G. Davies, E. Linfield, D. Ritchie, Y. Nakajima, M. Nakai, S. Sasa, M. Inoue, S. Chung, and M. B. Santos. Application of terahertz quantum-cascade lasers to semiconductor cyclotron resonance. *Opt. Lett.* **29**, 122 (2004).

[79] 1. Physikalisches Institut, Universität Stuttgart. *Millimeter and submillimeter wave spectroscopy.*
URL: `http://s2.pi1.physik.uni-stuttgart.de/Forschung/Submm_e.html`.

[80] R. D. Averitt, G. Rodriguez, J. L. W. Siders, S. A. Trugman, and A. J. Taylor. Conductivity artifacts in optical-pump THz-probe measurements of $YBa_2Cu_3O_7$. *J. Opt. Soc. Am. B* **17**, 327 (2000).

[81] M. C. Beard and C. A. Schmuttenmaer. Using the finite-difference time-domain pulse propagation method to simulate time-resolved THz experiments. *J. Chem. Phys.* **114**, 2903 (2001).

[82] H. Němec, F. Kadlec, and P. Kužel. Methodology of an optical pump-terahertz probe experiment: An analytical frequency-domain approach. *J. Chem. Phys.* **117**, 8454 (2002).

[83] S. S. Prabhu, S. E. Ralph, M. R. Melloch, and E. S. Harmon. Carrier dynamics of low-temperature-grown GaAs observed via THz spectroscopy. *Appl. Phys. Lett.* **70**, 2419 (1997).

[84] M. C. Beard, G. M. Turner, and C. A. Schmuttenmaer. Transient photoconductivity in GaAs as measured by time-resolved terahertz spectroscopy. *Phys. Rev. B* **62**, 15 764 (2000).

[85] C. Messner, H. Kostner, and R. A. Höpfel. Time-resolved THz spectroscopy of proton-bombarded InP. *J. Opt. Soc. Am. B* **18**, 1369 (2001).

[86] M. C. Beard, G. M. Turner, and C. A. Schmuttenmaer. Subpicosecond carrier dynamics in low-temperature grown GaAs as measured by time-resolved terahertz spectroscopy. *J. Appl. Phys.* **90**, 5915 (2001).

[87] K. P. H. Lui and F. A. Hegmann. Ultrafast carrier relaxation in radiation-damaged silicon on sapphire studied by optical-pump–terahertz-probe experiments. *Appl. Phys. Lett.* **78**, 3478 (2001).

[88] M. Schall and P. U. Jepsen. Above-band gap two-photon absorption and its influence on ultrafast carrier dynamics in ZnTe and CdTe. *Appl. Phys. Lett.* **80**, 4771 (2002).

[89] H. Němec, F. Kadlec, C. Kadlec, P. Kužel, and P. Jungwirth. Ultrafast far-infrared dynamics probed by terahertz pulses: A frequency domain approach. II. Applications. *J. Chem. Phys.* **122**, 10 4504 (2005).

[90] F. A. Hegmann, R. R. Tykwinski, K. P. H. Lui, J. E. Bullock, and J. E. Anthony. Picosecond transient photoconductivity in functionalized pentacene molecular crystals probed by terahertz pulse spectroscopy. *Phys. Rev. Lett.* **89**, 22 7403 (2002).

[91] E. Hendry, M. Koeberg, J. M. Schins, H. K. Nienhuys, V. Sundström, L. D. A. Siebbeles, and M. Bonn. Interchain effects in the ultrafast photophysics of a semiconducting polymer: THz time-domain spectroscopy of thin films and isolated chains in solution. *Phys. Rev. B* **71**, 12 5201 (2005).

[92] R. D. Averitt, G. Rodriguez, A. I. Lobad, J. L. W. Siders, S. A. Trugman, and A. J. Taylor. Nonequilibrium superconductivity and quasiparticle dynamics in $YBa_2Cu_3O_{7-\delta}$. *Phys. Rev. B* **63**, 14 0502 (2001).

[93] H. Wald, P. Seidel, and M. Tonouchi. Pump-and-probe terahertz method to investigate $YBa_2Cu_3O_{7-\delta}$ thin films. *Phys. C* **367**, 308 (2002).

[94] R. Huber, F. Tauser, A. Brodschelm, M. Bichler, G. Abstreiter, and A. Leitenstorfer. How many-particle interactions develop after ultrafast excitation of an electron–hole plasma. *Nature* **414**, 286 (2001).

[95] R. A. Kaindl, D. Hägele, M. A. Carnahan, R. Lövenich, and D. S. Chemla. Exciton dynamics studied via internal THz transitions. *Phys. Stat. Sol. B* **238**, 451 (2003).

[96] R. A. Kaindl, M. A. Carnahan, D. Hägele, R. Lövenich, and D. S. Chemla. Ultrafast terahertz probes of transient conducting and insulating phases in an electron–hole gas. *Nature* **423**, 734 (2003).

[97] F. Kadlec, H. Němec, and P. Kužel. Optical two-photon absorption in GaAs measured by optical-pump terahertz-probe spectroscopy. *Phys. Rev. B* **70**, 12 5205 (2004).

[98] R. McElroy and K. Wynne. Ultrafast dipole solvation measured in the far infrared. *Phys. Rev. Lett.* **79**, 3078 (1997).

[99] G. Haran, W.-D. Sun, K. Wynne, and R. M. Hochstrasser. Femtosecond far-infrared pump–probe spectroscopy: a new tool for studying low-frequency vibrational dynamics in molecular condensed phases. *Chem. Phys. Lett.* **274**, 365 (1997).

[100] M. C. Beard, G. M. Turner, and C. A. Schmuttenmaer. *American Chemical Society Symposium Series*, chap. 4. Low frequency, collective solvent dynamics probed with time-resolved THz spectroscopy, 44–58. American Chemical Society, Washington DC (2002).

[101] F. Kadlec, C. Kadlec, P. Kužel, P. Slavicek, and P. Jungwirth. Optical pump–terahertz probe spectroscopy of dyes in solutions: Probing the dynamics of liquid solvent or solid precipitate? *J. Chem. Phys.* **120**, 912 (2004).

[102] H. Němec, A. Pashkin, P. Kužel, M. Khazan, S. Schnüll, and I. Wilke. Carrier dynamics in low-temperature grown GaAs studied by terahertz emission spectroscopy. *J. Appl. Phys.* **90**, 1303 (2001).

[103] B. B. Hu, A. S. Weling, D. H. Auston, A. V. Kuznetsov, and C. J. Stanton. DC-electric-field dependence of THz radiation induced by femtosecond optical-excitation of bulk GaAs. *Phys. Rev. B* **49**, 2234 (1994).

[104] B. B. Hu, E. A. de Souza, W. H. Knox, J. E. Cunningham, M. C. Nuss, A. V. Kuznetsov, and S. L. Chuang. Identifying the distinct phases of carrier transport in semiconductors with 10 fs resolution. *Phys. Rev. Lett.* **74**, 1689 (1995).

[105] A. Leitenstorfer, S. Hunsche, J. Shah, M. C. Nuss, and W. H. Knox. Femtosecond charge transport in polar semiconductors. *Phys. Rev. Lett.* **82**, 5140 (1999).

[106] A. Leitenstorfer, S. Hunsche, J. Shah, M. C. Nuss, and W. H. Knox. Femtosecond high-field transport in compound semiconductors. *Phys. Rev. B* **61**, 16 643 (2000).

[107] P. C. M. Planken, M. C. Nuss, I. Brener, and K. W. Goossen. Terahertz emission in single quantum wells after coherent excitation of light hole and heavy hole excitons. *Phys. Rev. Lett.* **69**, 3800 (1992).

[108] C. Waschke, H. G. Roskos, R. Schwedler, K. Leo, H. Kurz, and K. Köhler. Coherent submillimetre-wave emission from Bloch oscillations in a semiconductor superlattice. *Phys. Rev. Lett.* **70**, 3319 (1993).

[109] C. Jaekel, H. G. Roskos, and H. Kurz. Emission of picosecond electromagnetic pulses from optically excited superconducting bridges. *Phys. Rev. B* **54**, R6889 (1996).

[110] M. Hangyo, S. Tomozawa, Y. Murakami, M. Tonouchi, M. Tani, Z. Wang, K. Sakai, and S. Nakashima. Terahertz radiation from superconducting $YBa_2Cu_3O_{7-\delta}$ delta thin films excited by femtosecond optical pulses. *Appl. Phys. Lett.* **69**, 2122 (1996).

[111] N. Kida and M. Tonouchi. Reversible and bistable terahertz radiation from magnetoresistive $Pr_{0.7}Ca_{0.3}MnO_3$ thin films. *Appl. Phys. Lett.* **82**, 3412 (2003).

[112] M. C. Beard, G. M. Turner, and C. A. Schmuttenmaer. Measurement of electromagnetic radiation emitted during rapid intramolecular electron transfer. *J. Am. Chem. Soc.* **122**, 11 541 (2000).

[113] D. Clery. Terahertz on a chip. *Science* **297**, 763 (2002).

[114] Y. C. Shen, T. Lo, P. F. Taday, B. E. Cole, W. R. Tribe, and M. C. Kemp. Detection and identification of explosives using terahertz pulsed spectroscopic imaging. *Appl. Phys. Lett.* **86**, 24 1116 (2005).

[115] R. M. Woodward, V. P. Wallace, D. D. Arnone, E. H. Linfield, and M. Pepper. Terahertz pulsed imaging of skin cancer in the time and frequency domain. *J. Biol. Phys.* **29**, 257 (2003).

[116] E. Pickwell, B. E. Cole, A. J. Fitzgerald, M. Pepper, and V. P. Wallace. *In vivo* study of human skin using pulsed terahertz radiation. *Phys. Med. Biol.* **49**, 1595 (2004).

[117] P. H. Siegel. Terahertz technology in biology and medicine. *IEEE Trans. Microwave Theory Tech.* **52**, 2438 (2004).

[118] B. B. Hu and M. C. Nuss. Imaging with terahertz waves. *Opt. Lett.* **20**, 1716 (1995).

[119] D. M. Mittleman, R. H. Jacobsen, and M. C. Nuss. T-Ray imaging. *IEEE J. Selected Topics in Quantum Electron.* **2**, 679 (1996).

[120] Q. Wu, T. D. Hewitt, and X.-C. Zhang. Two-dimensional electro-optic imaging of THz beams. *Appl. Phys. Lett.* **69**, 1026 (1996).

[121] S. Wang and X.-C. Zhang. Tomographic imaging with a terahertz binary lens. *Appl. Phys. Lett.* **82**, 1821 (2003).

[122] B. Ferguson, S. Wang, D. Gray, D. Abbot, and X.-C. Zhang. T-ray computed tomography. *Opt. Lett.* **27**, 1312 (2002).

[123] J. Pearce, H. Choi, and D. M. Mittleman. Terahertz wide aperture reflection tomography. *Opt. Lett.* **30**, 1653 (2005).

[124] O. Mitrofanov, I. Brener, R. Harel, J. D. Wynn, L. N. Pfeiffer, K. W. West, and J. Federici. Terahertz near-field microscopy based on a collection mode detector. *Appl. Phys. Lett.* **77**, 3496 (2000).

[125] N. C. J. van der Valk and P. C. M. Planken. Electro-optic detection of subwavelength terahertz spot sizes in the near field of a metal tip. *Appl. Phys. Lett.* **81**, 1558 (2002).

[126] H.-T. Chen, R. Kersting, and G. C. Cho. Terahertz imaging with nanometer resolution. *Appl. Phys. Lett.* **83**, 3009 (2003).

[127] N. Klein, P. Lahl, U. Poppe, F. Kadlec, and P. Kužel. A metal-dielectric antenna for terahertz near-field imaging. *J. Appl. Phys.* **98**, 01 4910 (2005).

[128] L. Duvillaret, F. Garet, and J.-L. Coutaz. Highly precise determination of optical constants and sample thickness in terahertz time-domain spectroscopy. *Appl. Opt.* **38**, 409 (1999).

[129] L. Duvillaret, F. Garet, and J.-L. Coutaz. A reliable method for extraction of material parameters in terahertz time-domain spectroscopy. *IEEE J. Selected Topics in Quantum Electron.* **2**, 739 (1996).

[130] P. Kužel and J. Petzelt. Time-resolved terahertz transmission spectroscopy of dielectrics. *Ferroelectrics* **239**, 949 (2000).

[131] A. Pashkin, E. Buixaderas, P. Kužel, M.-H. Liang, C.-T. Hu, and I.-N. Lin. THz transmission spectroscopy applied to dielectrics and microwave ceramics. *Ferroelectrics* **254**, 113 (2001).

[132] D. Grischkowsky and S. Keiding. THz time-domain spectroscopy of high T_c substrates. *Appl. Phys. Lett.* **57**, 1055 (1990).

[133] T.-I. Jeon and D. Grischkowsky. Nature of conduction in doped silicon. *Phys. Rev. Lett.* **78**, 1106 (1997).

[134] T.-I. Jeon and D. Grischkowsky. Observation of a Cole-Davidson type complex conductivity in the limit of very low carrier densities in doped silicon. *Appl. Phys. Lett.* **72**, 2259 (1998).

[135] H. J. Bakker, S. Hunsche, and H. Kurz. Investigation of anharmonic lattice-vibrations with coherent phonon polaritons. *Phys. Rev. B* **50**, 914 (1994).

[136] F. Kadlec, S. Kamba, P. Kužel, C. Kadlec, J. Kroupa, and J. Petzelt. High-temperature phase transitions in $SrBi_2Ta_2O_9$ film: a study by THz spectroscopy. *J. Phys.: Cond. Matt.* **16**, 6763 (2004).

[137] S. Kamba, J. Petzelt, E. Buixaderas, D. Haubrich, P. Vaněk, P. Kužel, I. N. Jawahar, M. T. Sebastian, and P. Mohanan. High frequency dielectric properties of $A_5B_4O_{15}$ microwave ceramics. *J. Appl. Phys.* **89**, 3900 (2001).

[138] J. T. Kindt and C. A. Schmuttenmaer. Far-infrared dielectric properties of polar liquids probed by femtosecond terahertz pulse spectroscopy. *J. Phys. Chem.* **100**, 10 373 (1996).

[139] J. E. Pedersen and S. R. Keiding. THz time-domain spectroscopy of nonpolar liquids. *IEEE J. Quantum Electron.* **28**, 2518 (1992).

[140] B. N. Flanders, R. A. Cheville, D. Grischkowsky, and N. F. Scherer. Pulsed terahertz transmission spectroscopy of liquid $CHCl_3$, CCl_4, and their mixtures. *J. Phys. Chem.* **100**, 11 824 (1996).

[141] T. M. Nymand, C. Rønne, and S. R. Keiding. The temperature dependent dielectric function of liquid benzene: Interpretation of THz spectroscopy data by molecular dynamics simulation. *J. Chem. Phys.* **114**, 5246 (2001).

[142] M. C. Nuss, K. W. Goossen, J. P. Gordon, P. M. Mankiewich, M. L. O'Malley, and M. Bhushan. Terahertz time-domain measurement of the conductivity and superconducting band gap in niobium. *J. Appl. Phys.* **70**, 2238 (1991).

[143] M. C. Nuss, P. M. Mankiewich, M. L. O'Malley, and E. H. Westerwick. Dynamic conductivity and "coherence peak" in $YBa_2Cu_3O_7$ superconductors. *Phys. Rev. Lett.* **66**, 3305 (1991).

[144] S. Spielman, B. Parks, J. Orenstein, D. T. Nemeth, F. Ludwig, J. Clarke, P. Merchant, and D. J. Lew. Observation of the quasiparticle Hall effect in superconducting $YBa_2Cu_3O_{7-\delta}$. *Phys. Rev. Lett.* **73**, 1537 (1994).

[145] R. A. Cheville and D. Grischkowsky. Far-infrared terahertz time-domain spectroscopy of flames. *Opt. Lett.* **20**, 1646 (1995).

[146] M. Brucherseifer, M. Nagel, P. H. Bolivar, H. Kurz, A. Bosserhoff, and R. Büttner. Label-free probing of the binding state of DNA by time-domain terahertz sensing. *Appl. Phys. Lett.* **77**, 4049 (2000).

[147] J. Petzelt, P. Kužel, I. Rychetský, A. Pashkin, and T. Ostapchuk. Dielectric response of soft modes in ferroelectric thin films. *Ferroelectrics* **288**, 169 (2003).

[148] S. Nashima, O. Morikawa, K. Takata, and M. Hangyo. Measurement of optical properties of highly doped silicon by terahertz time domain reflection spectroscopy. *Appl. Phys. Lett.* **79**, 3923 (2001).

[149] A. Pashkin, M. Kempa, H. Němec, F. Kadlec, and P. Kužel. Phase-sensitive time-domain terahertz reflection spectroscopy. *Rev. Sci. Instrum.* **74**, 4711 (2003).

[150] L. Thrane, R. H. Jacobsen, P. U. Jepsen, and S. R. Keiding. THz reflection spectroscopy of liquid water. *Chem. Phys. Lett.* **240**, 330 (1995).

[151] C. Rønne, L. Thrane, P.-O. Åstrand, A. Wallqvist, K. V. Mikkelsen, and S. R. Keiding. Investigation of the temperature dependence of in liquid water by THz reflection spectroscopy dynamics simulation. *J. Chem. Phys.* **107**, 5319 (1997).

[152] C. Rønne, P.-O. Åstrand, and S. R. Keiding. THz spectroscopy of liquid H_2O and D_2O. *Phys. Rev. Lett.* **82**, 2888 (1999).

[153] C. Rønne and S. R. Keiding. Low frequency spectroscopy of liquid water using THz-time domain spectroscopy. *J. Mol. Liquids* **101**, 199 (2002).

[154] S. C. Howells and L. A. Schlie. Transient terahertz reflection spectroscopy of undoped InSb from 0.1 to 1.1 THz. *Appl. Phys. Lett.* **69**, 550 (1996).

[155] T.-I. Jeon and D. Grischkowsky. Characterization of optically dense, doped semiconductors by reflection THz time domain spectroscopy. *Appl. Phys. Lett.* **72**, 3032 (1998).

[156] T. Nagashima and M. Hangyo. Measurement of complex optical constants of a highly doped Si wafer using terahertz ellipsometry. *Appl. Phys. Lett.* **79**, 3917 (2001).

[157] D. Hashimshony, I. Geltner, G. Cohen, Y. Avitzour, A. Zigler, and C. Smith. Characterization of the electrical properties and thickness of thin epitaxial semiconductor layers by THz reflection spectroscopy. *J. Appl. Phys.* **90**, 5778 (2001).

[158] P. Kužel, A. Pashkin, M. Kempa, F. Kadlec, S. Kamba, and J. Petzelt. Time-domain terahertz spectroscopy of $SrBi_2Ta_2O_9$. *Ferroelectrics* **300**, 125 (2004).

[159] A. M. Balbashov, G. V. Kozlov, A. A. Mukhin, and A. S. Prokhorov. *High frequency processes in magnetic materials*, chap. Submillimeter spectroscopy of antiferromagnetic dielectrics, 56–98. World Scientific, Singapore (1995).

[160] A. A. Mukhin, A. Y. Pronin, A. S. Prokhorov, G. V. Kozlov, V. Železný, and J. Petzelt. Submillimeter and far IR spectroscopy of magneto- and electrodipolar rare-earth modes in the orthoferrite $TmFeO_3$. *Phys. Lett. A* **153**, 499 (1991).

[161] R. W. Sanders, R. M. Belanger, M. Motokawa, V. Jaccarino, and S. M. Rezende. Magnetic polariton, impurity mode enhancement, and superradiance effects in FeF_2. *Phys. Rev. B* **23**, 1190 (1981).

[162] K. M. Häussler, J. Brandmüller, L. Merten, H. Finsterhölzl, and A. Lehmeyer. Observation of dispersion on magnetic polaritons. *Phys. Stat. Sol. B* **117**, 225 (1983).

[163] A. Mukhin, B. Gorshunov, M. Dressel, C. Sangregorio, and D. Gatteschi. Optical spectroscopy of crystal-field transitions in the molecular magnet Fe_8. *Phys. Rev. B* **63**, 21 4411 (2001).

[164] K. N. Kocharyan, M. N. Afsar, and I. I. Tkachov. New method for measurement of complex magnetic permeability in the millimeter-wave range, part II: hexaferrites. *IEEE Trans. Magn.* **35**, 2104 (1999).

[165] K. N. Kocharyan, M. N. Afsar, and I. I. Tkachov. Millimeter-wave magnetooptics: new method for characterization of ferrites in the millimeter-wave range. *IEEE Trans. Microwave Theory Tech.* **47**, 2636 (1999).

[166] S. W. McKnight, L. Carin, C. Vittoria, S. F. Wahid, K. Agi, and D. Kralj. Picosecond-pulse and millimetre-wave spectroscopy of barium ferrite. *IEEE Trans. Magn.* **32**, 372 (1996).

[167] J. B. Pendry. Negative refraction makes a perfect lens. *Phys. Rev. Lett.* **85**, 3966 (2000).

[168] R. A. Shelby, D. R. Smith, and S. Schultz. Experimental verification of a negative index of refraction. *Science* **292**, 77 (2001).

[169] D. R. Smith, J. B. Pendry, and M. C. K. Wiltshire. Metamaterials and negative refractive index. *Science* **305**, 788 (2004).

[170] T. J. Yen, W. J. Padilla, N. Fang, D. C. Vier, D. R. Smith, J. B. Pendry, D. N. Basov, and X. Zhang. Terahertz magnetic response from artificial materials. *Science* **303**, 1494 (2004).

[171] S. Linden, C. Enkrich, M. Wegener, J. Zhou, T. Koschny, and C. M. Soukoulis. Magnetic response of metamaterials at 100 terahertz. *Science* **306**, 1351 (2004).

[172] H. O. Moser, B. D. F. Casse, O. Wilhelmi, and B. T. Saw. Terahertz response of a microfabricated rod–split-ring-resonator electromagnetic metamaterial. *Phys. Rev. Lett.* **94**, 06 3901 (2005).

[173] D. R. Smith, S. Schultz, P. Markoš, and C. M. Soukoulis. Determination of effective permittivity and permeability of metamaterials from reflection and transmission coefficients. *Phys. Rev. B* **65**, 19 5104 (2002).

[174] R. E. Denton, R. D. Campbell, and S. G. Tomlin. The determination of the optical constants of thin films from measurements of reflectance and transmittance at normal incidence. *J. Phys. D* **5**, 852 (1972).

[175] L. Duvillaret, F. Garet, and J.-L. Coutaz. Influence of noise on the characterization of materials by terahertz time-domain spectroscopy. *J. Opt. Soc. Am. B* **17**, 452 (2000).

[176] G. Gallot, J. Zhang, R. W. McGowan, T.-I. Jeon, and D. Grischkowsky. Measurements of the THz absorption and dispersion of ZnTe and their relevance to the electro-optic detection of THz radiation. *Appl. Phys. Lett.* **74**, 3450 (1999).

[177] S. O'Brien and J. B. Pendry. Photonic band-gap effects and magnetic activity in dielectric composites. *J. Phys.: Cond. Matt.* **14**, 4035 (2002).

[178] S. John. Strong localization of photons in certain disordered dielectric superlattices. *Phys. Rev. Lett.* **58**, 2486 (1987).

[179] J. D. Joannopoulos, R. D. Meade, and J. N. Winn. *Molding the Flight of the Light*. Princeton University Press, Princeton, New Jersey (1995).

[180] E. Yablonovitch and T. J. Gmitter. Photonic band structure: The face-centered-cubic case. *Phys. Rev. Lett.* **63**, 1950 (1989).

[181] K. M. Ho, C. T. Chan, and C. M. Soukolis. Existence of a photonic gap in periodic dielectric structures. *Phys. Rev. Lett.* **65**, 3152 (1990).

[182] E. Yablonovitch. Photonic band-gap structures. *J. Opt. Soc. Am. B* **10**, 283 (1993).

[183] S. L. McCall, P. M. Platzman, R. Dalichaouch, D. Smith, and S. Schultz. Microwave propagation in two-dimensional dielectric lattices. *Phys. Rev. Lett.* **67**, 2017 (1991).

[184] W. M. Robertson, G. Arjavalingam, R. D. Meade, K. D. Brommer, A. M. Rappe, and J. D. Joannopoulos. Measurement of photonic band structure in a two-dimensional periodic dielectric array. *Phys. Rev. Lett.* **68**, 2023 (1992).

[185] E. Yablonovitch, T. J. Gmitter, R. D. Meade, A. M. Rappe, K. D. Brommer, and J. D. Joannopoulos. Donor and acceptor modes in photonic band structures. *Phys. Rev. Lett.* **67**, 3380 (1991).

[186] R. D. Meade, K. D. Brommer, A. M. Rappe, and J. D. Joannopoulos. Photonic bound states in periodic dielectric materials. *Phys. Rev. B* **44**, 13 772 (1991).

[187] D. R. Smith, R. Dalichaouch, N. Kroll, S. Schultz, S. L. McCall, and P. M. Platzman. Photonic band structure and defects in one and two dimensions. *J. Opt. Soc. Am. B* **10**, 314 (1993).

[188] C. M. Bowden and A. M. Zheltikov. Nonlinear Optics of Photonic Crystals (2002). Special issue on nonlinear photonic crystals.

[189] K. Sakoda. *Optical properties of photonic crystals*. Springer, Berlin (2001).

[190] L. C. Andreani. Photonic bands and radiation losses in photonic crystal waveguides. *Phys. Stat. Sol. B* **234**, 139 (2002).

[191] M. Born and E. Wolf. *Principles of Optics*, chap. Propagation, modulation, and oscillation in dielectric waveguides. Waveguide modes—a general discussion, 479–487. Cambridge University Press, Cambridge, 7th edn. (1999).

[192] J. D. Joannopoulos, P. R. Villeneuve, and S. Fan. Photonic crystals: putting a new twist on light. *Nature* **386**, 143 (1997).

[193] J. S. Foresi, P. R. Villeneuve, J. Ferrera, E. R. Thoen, G. Steinmeyer, S. Fan, J. D. Joannopoulos, L. C. Kimerling, H. I. Smith, and E. P. Ippen. Photonic-bandgap microcavities in optical waveguides. *Nature* **390**, 143 (1997).

[194] O. Painter, R. K. Lee, A. Scherer, A. Yariv, J. D. O'Brien, P. D. Dapkus, and I. Kim. Two-dimensional photonic band-gap defect mode laser. *Science* **284**, 1819 (1999).

[195] B. Maune, M. Lončar, J. Witzens, M. Hochberg, T. Baehr-Jones, D. Psaltis, A. Scherer, and Y. Qiu. Liquid-crystal electric tuning of a photonic crystal laser. *Appl. Phys. Lett.* **85**, 360 (2004).

[196] S. Ogawa, M. Imada, S. Yoshimoto, M. Okano, and S. Noda. Control of light emission by 3D photonic crystals. *Science* **305**, 227 (2004).

[197] B. Temelkuran, M. Bayindir, E. Özbay, R. Biswas, M. M. Sigalas, G. Tuttle, and K. Ho. Photonic crystal-based resonant antenna with a very high directivity. *J. Appl. Phys.* **87**, 603 (2000).

[198] E. Özbay, B. Temelkuran, and M. Bayindir. Microwave applications of photonic crystals. *Prog. in Electromag. Res.* **41**, 185 (2003).

[199] S. John and M. Florescu. Photonic bandgap materials: towards an all-optical micro-transistor. *J. Opt. A* **3**, 103 (2001).

[200] T. D. Drysdale, I. S. Gregory, C. Baker, E. H. Linfield, W. R. Tribe, and D. R. S. Cumming. Transmittance of a tunable filter at terahertz frequencies. *Appl. Phys. Lett.* **85**, 5173 (2004).

[201] R. P. Stanley, R. Houdré, U. Oesterle, and M. Ilegems. Imputiry modes in one-dimensional periodic-systems: The transition from photonic band gaps to microcavities. *Phys. Rev. A* **48**, 2246 (1993).

[202] Y. Akahane, T. Asano, B.-S. Song, and S. Noda. High-Q photonic nanocavity in a two-dimensional photonic crystal. *Nature* **425**, 944 (2003).

[203] K. M. Chen, A. W. Sparks, H.-C. Luan, D. R. Lim, K. Wada, and L. C. Kimerling. SiO_2/TiO_2 omnidirectional reflector and microcavity resonator via the sol-gel method. *Appl. Phys. Lett.* **75**, 3805 (1999).

[204] H.-Y. Lee and T. Yao. Design and evaluation of omnidirectional one-dimensional photonic crystals. *J. Appl. Phys.* **93**, 819 (2003).

[205] A. Mekis, J. C. Chen, I. Kurland, S. Fan, P. R. Villeneuve, and J. D. Joannopoulos. High transmission through sharp bends in photonic crystal waveguides. *Phys. Rev. Lett.* **77**, 3787 (1996).

[206] S.-Y. Lin, E. Chow, V. Hietala, P. R. Villeneuve, and J. D. Joannopoulos. Experimental demonstration of guiding and bending of electromagnetic waves in a photonic crystal. *Science* **282**, 274 (1998).

[207] A. Chutinan, S. John, and O. Toader. Diffractionless flow of light in all-optical microchips. *Phys. Rev. Lett.* **90**, 123901 (2003).

[208] R. F. Cregan, B. J. Mangan, J. C. Knight, T. A. Birks, P. S. J. Russell, P. J. Roberts, and D. C. Allan. Single-mode photonic band gap guidance of light in air. *Science* **285**, 1537 (1999).

[209] M. Schuster and N. Klein. Controlled excitation of electromagnetic band-gap line and point defect modes at microwave frequencies. *J. Appl. Phys.* **93**, 3182 (2003).

[210] H. Kosaka, T. Kawashima, A. Tomita, M. Notomi, T. Tamamura, T. Sato, and S. Kawakami. Superprism phenomena in photonic crystals. *Phys. Rev. B* **58**, R10096 (1998).

[211] K. B. Chung and S. W. Hong. Wavelength demultiplexers based on the superprism phenomena in photonic crystals. *Appl. Phys. Lett.* **81**, 1549 (2002).

[212] K. Oya, T. Nakazawa, S. Kittaka, K. Tsunetomo, K. Kintaka, J. Nishii, and K. Hirao. Ultrasmall demultiplexer by use of one-dimensional photonic crystal. *Opt. Lett.* **30**, 192 (2005).

[213] D. Eger, M. Oron, and M. Katz. Optical characterization of $KTiOPO_4$ periodically segmented waveguides for second-harmonic generation of blue light. *J. Appl. Phys.* **74**, 4298 (1993).

[214] E. Popov, M. Neviere, R. Reinisch, J.-L. Coutaz, and J. F. Roux. Grating-enhanced second-harmonic generation in polymer waveguides: role of losses. *Appl. Opt.* **34**, 3398 (1995).

[215] T. W. Mossberg, C. M. Greiner, and D. Iazikov. Holographic bragg reflectors, photonic bandgaps and photonic integrated circuits. *Opt. Photonics News* **15**, 26 (2004).

[216] Z. Weissman and A. Hardy. Modes of periodically segmented wave-guides. *J. Lightwave Tech.* **11**, 1831 (1993).

[217] E. Silberstein, P. Lalanne, J.-P. Hugonin, and Q. Cao. Use of grating theories in integrated optics. *J. Opt. Soc. Am. A* **18**, 2865 (2001).

[218] P. Vukusic, J. R. Sambles, C. R. Lawrence, and R. J. Wootton. Quantified interference and diffraction in single *Morpho* butterfly scales. *Proc. R. Soc. London B* **266**, 1403 (1999).

[219] P. Vukusic and J. R. Sambles. Photonic structures in biology. *Nature* **424**, 852 (2003).

[220] S. A. Ramakrishna. Physics of negative refractive index materials. *Rep. Prog. Phys.* **68**, 449 (2005).

[221] D. R. Smith, W. J. Padilla, D. C. Vier, S. C. Nemat-Nasser, and S. Schultz. Composite medium with simultaneously negative permeability and permittivity. *Phys. Rev. Lett.* **84**, 4184 (2000).

[222] A. Grbic and G. V. Eleftheriades. Experimental verification of backward-wave radiation from a negative refractive index metamaterial. *J. Appl. Phys.* **92**, 5930 (2002).

[223] G. W. 't Hooft. Comment on "Negative refraction makes a perfect lens". *Phys. Rev. Lett.* **87**, 24 9701 (2001).

[224] J. M. Williams. Some problems with negative refraction. *Phys. Rev. Lett.* **87**, 24 9703 (2001).

[225] N. Garcia and M. Nieto-Vesperinas. Left-handed materials do not make a perfect lens. *Phys. Rev. Lett.* **88**, 20 7403 (2002).

[226] A. L. Pokrovsky and A. L. Efros. Sign of refractive index and group velocity in left-handed media. *Solid State Commun.* **124**, 283 (2002).

[227] A. L. Pokrovsky and A. L. Efros. Electrodynamics of metallic photonic crystals and the problem of left-handed materials. *Phys. Rev. Lett.* **89**, 09 3901 (2002).

[228] S. Foteinopoulou, E. N. Economou, and C. M. Soukoulis. Refraction in media with a negative refractive index. *Phys. Rev. Lett.* **90**, 10 7402 (2003).

[229] J. B. Pendry. Comment on "Left-handed materials do not make a perfect lens". *Phys. Rev. Lett.* **91**, 09 9701 (2003).

[230] D. Maystre and S. Enoch. Perfect lenses made with left-handed materials: Alices mirror? *J. Opt. Soc. Am. A* **21**, 122 (2004).

[231] A. Grbic and G. V. Eleftheriades. Overcoming the diffraction limit with a planar left-handed transmission-line lens. *Phys. Rev. Lett.* **92**, 11 7403 (2004).

[232] N. Fang, H. Lee, C. Sun, and X. Zhang. Sub–diffraction-limited optical imaging with a silver superlens. *Science* **308**, 534 (2005).

[233] J. B. Pendry, A. J. Holden, W. J. Stewart, and I. Youngs. Extremely low frequency plasmons in metallic mesostructures. *Phys. Rev. Lett.* **76**, 4773 (1996).

[234] J. B. Pendry, A. J. Holden, D. J. Robbins, and W. J. Stewart. Low frequency plasmons in thin-wire structures. *J. Phys.: Cond. Matt.* **10**, 4785 (1998).

[235] D. R. Fredkin and A. Ron. Effectively left-handed (negative index) composite material. *Appl. Phys. Lett.* **81**, 1753 (2002).

[236] F. J. Rachford, D. L. Smith, P. F. Loschialpo, and D. W. Forester. Calculations and measurements of wire and/or split-ring negative index media. *Phys. Rev. E* **66**, 03 6613 (2002).

[237] P. Gay-Balmaz and O. J. F. Martin. Electromagnetic resonances in individual and coupled split-ring resonators. *J. Appl. Phys.* **92**, 2929 (2002).

[238] M. Bayindir, K. Aydin, E. Özbay, P. Markoš, and C. M. Soukoulis. Transmission properties of composite metamaterials in free space. *Appl. Phys. Lett.* **81**, 120 (2002).

[239] A. A. Houck, J. B. Brock, and I. L. Chuang. Experimental observations of a left-handed material that obeys Snell's law. *Phys. Rev. Lett.* **90**, 13 7401 (2003).

[240] C. G. Parazzoli, R. B. Greegor, K. Li, B. E. C. Koltenbah, and M. Tanielian. Experimental verification and simulation of negative index of refraction using Snell's law. *Phys. Rev. Lett.* **90**, 10 7401 (2003).

[241] K. Aydin, K. Guven, M. Kafesaki, L. Zhang, C. M. Soukoulis, and E. Özbay. Experimental observation of true left-handed transmission peaks in metamaterials. *Opt. Lett.* **29**, 2623 (2004).

[242] C. L. Holloway, E. F. Kuester, J. Baker-Jarvis, and P. Kabos. Photonic band-gap effects and magnetic activity in dielectric composites. *IEEE Trans. Antennas Propag.* **51**, 2596 (2003).

[243] V. Yannopapas and A. Moroz. Negative refractive index metamaterials from inherently non-magnetic materials for deep infrared to terahertz frequency ranges. *J. Phys.: Cond. Matt.* **17**, 3717 (2005).

[244] C. Luo, S. G. Johnson, J. D. Joannopoulos, and J. B. Pendry. All-angle negative refraction without negative refractive index. *Phys. Rev. B* **65**, 20 1104 (2002).

[245] C. Luo, S. G. Johnson, and J. D. Joannopoulos. All-angle negative refraction in a three-dimensionally periodic photonic crystal. *Appl. Phys. Lett.* **82**, 2352 (2002).

[246] S. Foteinopoulou and C. M. Soukoulis. Negative refraction and left-handed behavior in two-dimensional photonic crystals. *Phys. Rev. B* **67**, 23 5107 (2003).

[247] E. Cubukcu, K. Aydin, E. Özbay, S. Foteinopoulou, and C. M. Soukoulis. Negative refraction by photonic crystals. *Nature* **423**, 604 (2003).

[248] R. D. Meade, K. D. Brommer, A. M. Rappe, J. D. Joannopoulos, and O. L. Alerhand. Accurate theoretical analysis of photonic band-gap materials. *Phys. Rev. B* **48**, 8434 (1993).

[249] W. H. Press, S. A. Teukolsky, W. T. Vetterling, and B. P. Flannery. *Numerical Recipes in C*, chap. 11 Eigensystems, 456–495. Cambridge University Press, Cambridge, New York, Port Chester, Melbourne, Sydney (1997).

[250] J. B. Pendry and A. MacKinnon. Calculation of photon dispersion relations. *Phys. Rev. Lett.* **69**, 2772 (1992).

[251] J. B. Pendry. Photonic band structures. *J. Mod. Opt.* **41**, 209 (1994).

[252] P. M. Bell, J. B. Pendry, L. M. Moreno, and A. J. Ward. A program for calculating photonic band structures and transmission coefficients of complex structures. *Comput. Phys. Commun.* **85**, 306 (1995).

[253] M. Born and E. Wolf. *Principles of Optics*, chap. 1.6, 54–74. Cambridge University Press, Cambridge, 7th edn. (1999).

[254] N. H. Liu. Defect modes of stratified dielectric media. *Phys. Rev. B* **55**, 4097 (1997).

[255] G. Torosyan, C. Rau, B. Pradarutti, and R. Beigang. Generation and propagation of surface plasmons in periodic metallic structures. *Appl. Phys. Lett.* **85**, 3372 (2004).

[256] W. L. Barnes, A. Dereux, and T. W. Ebbesen. Surface plasmon subwavelength optics. *Nature* **424**, 824 (2003).

[257] H. Ditlbacher, J. R. Krenn, G. Schider, A. Leitner, and F. R. Aussenegg. Two-dimensional optics with surface plasmon polaritons. *Appl. Phys. Lett.* **81**, 1762 (2002).

[258] S. T. Peng, T. Tamir, and H. L. Bertoni. Theory of periodic dielectric waveguides. *IEEE Trans. Microwave Theory Tech.* **23**, 123 (1975).

[259] L. Li and J. J. Burke. Linear propagation characteristics of periodically segmented waveguides. *Opt. Lett.* **17**, 1195 (1992).

[260] D. D. Stancil. Kronig–Penney model for periodically segmented waveguides. *Appl. Opt.* **35**, 4767 (1996).

[261] J. D. Swalen, J. G. G. II, M. R. Philpott, A. Brillante, I. Pockrand, and R. Santo. Plasmon surface polariton dispersion by direct optical observation. *Am. J. Phys.* **48**, 669 (1980).

[262] S. C. Kitson, W. L. Barnes, G. W. Bradberry, and J. R. Sambles. Surface profile dependence of surface plasmon band gaps on metallic gratings. *J. Appl. Phys.* **79**, 7383 (1996).

[263] J.-L. Coutaz, F. Garet, E. Bonnet, A. V. Tishchenko, O. Parriaux, and M. Nazarov. Grating diffraction effects in the THz domain. *Acta Phys. Pol. A* **107**, 26 (2005).

[264] S. M. Norton, T. Erdogan, and G. M. Morris. Coupled-mode theory of resonant-grating filters. *J. Opt. Soc. Am. A* **14**, 629 (1997).

[265] C. Genet, M. P. van Exter, and J. P. Woerdman. Fano-type interpretation of red shifts and red tails in hole array transmission spectra. *Opt. Commun.* **225**, 331 (2003).

[266] K. Rektorys. *Survey of applicable mathematics*, chap. 17. Ordinary differential equations. Kluwer Academic Publishers, 2nd edn. (1969).

[267] W. H. Press, S. A. Teukolsky, W. T. Vetterling, and B. P. Flannery. *Numerical Recipes in C*, chap. 10.4 Downhill simplex method in multidimensions, 408–412. Cambridge University Press, Cambridge, New York, Port Chester, Melbourne, Sydney (1997).

[268] S. Fan, P. R. Villeneuve, J. D. Joannopoulos, and E. F. Schubert. In *Proceedings of SPIE*, vol. 3002, 67–73 (1997).

[269] X. Wang, K. Kempa, Z. F. Ren, and B. Kimball. Rapid photon flux switching in two-dimensional photonic crystals. *Appl. Phys. Lett.* **84**, 1817 (2004).

[270] D. A. Mazurenko, R. Kerst, J. I. Dijkhuis, A. V. Akimov, V. G. Golubev, D. A. Kurdyukov, A. B. Pevtsov, and A. Svlkin. Ultrafast optical switching in three-dimensional photonic crystals. *Phys. Rev. Lett.* **91**, 21 3903 (2003).

[271] A. Chelnokov, S. Rowson, J. M. Lourtioz, L. Duvillaret, and J. L. Coutaz. Light controllable defect modes in three-dimensional photonic crystal. *Electron. Lett.* **34**, 1965 (1998).

[272] S. W. Leonard, H. M. van Driel, J. Schilling, and R. B. Wehrspohn. Ultrafast band-edge tuning of a two-dimensional silicon photonic crystal via free-carrier injection. *Phys. Rev. B* **66**, 16 1102 (2002).

[273] B. Li, J. Zhou, L. Li, X. J. Wang, X. H. Liu, and J. Zi. Ferroelectric inverse opals with electrically tunable photonic band gap. *Appl. Phys. Lett.* **83**, 4704 (2003).

[274] A. S. Sánchez and P. Halevi. Simulation of tuning of one-dimensional photonic crystals in the presence of free electrons and holes. *J. Appl. Phys.* **94**, 797 (2003).

[275] T. D. Drysdale, R. J. Blaikie, and D. R. S. Cumming. Calculated and measured transmittance of a tunable metallic photonic crystal filter for terahertz frequencies. *Appl. Phys. Lett.* **83**, 5362 (2003).

[276] P. Halevi and F. Ramos-Mendieta. Tunable photonic crystals with semiconducting constituents. *Phys. Rev. Lett.* **85**, 1875 (2000).

[277] Y. Lai, W. Zhang, L. Zhang, J. A. R. Williams, and I. Bennion. Optically tunable fiber grating transmission filters. *Opt. Lett.* **28**, 2446 (2003).

[278] R. Ozaki, T. Matsui, M. Ozaki, and K. Yoshino. Electrically color-tunable defect mode lasing in one-dimsional photonic-band-gap system containing liquid crystal. *Appl. Phys. Lett.* **82**, 3593 (2003).

[279] B. Wild, R. Ferrini, R. Houdré, M. Mulot, S. Anand, and C. J. M. Smith. Temperature tuning of the optical properties of planar photonic crystal microcavities. *Appl. Phys. Lett.* **84**, 846 (2004).

[280] R. Ozaki, Y. Matsuhisa, M. Ozaki, and K. Yoshino. Electrically tunable lasing based on defect mode in one-dimensional photonic crystal with conducting polymer and liquid crystal defect layer. *Appl. Phys. Lett.* **84**, 1844 (2004).

[281] H. Miyazaki, Y. Jimba, C. Y. Kim, and T. Watanabe. Defects and photonic wells in one-dimensional photonic lattices. *J. Phys. Soc. Jpn.* **65**, 3842 (1996).

[282] Y. C. Tsai, K. W. K. Shung, and S. C. Gou. Impurity modes in one-dimensional photonic crystals—analytic approach. *J. Mod. Opt.* **45**, 2147 (1998).

[283] A. Figotin and V. Gorentsveig. Localized electromagnetic waves in a layered periodic dielectric medium with a defect. *Phys. Rev. B* **58**, 180 (1998).

[284] E. Pistono, P. Ferrari, L. Duvillaret, J. M. Duchamp, and R. G. Harrison. Hybrid narrow-band tunable bandpass filter based on varactor loaded electromagnetic-bandgap coplanar waveguides. *IEEE Trans. Microwave Theory Tech.* **53**, 2506 (2005).

[285] H. Němec, L. Duvillaret, F. Quemeneur, and P. Kužel. Defect modes caused by twinning in one-dimensional photonic crystals. *J. Opt. Soc. Am. B* **21**, 548 (2004).

[286] E. Özbay and B. Temelkuran. Reflection properties and defect formation in photonic crystals. *Appl. Phys. Lett.* **69**, 743 (1996).

[287] T. Aoki, M. W. Takeda, J. W. Haus, Z. Yuan, M. Tani, K. Sakai, N. Kawai, and K. Inoue. Terahertz time-domain study of a pseudo-simple-cubic photonic lattice. *Phys. Rev. B* **64**, 04 5106 (2001).

[288] H. Němec, P. Kužel, F. Garet, and L. Duvillaret. Time-domain terahertz study of defect formation in one-dimensional photonic crystals. *Appl. Opt.* **43**, 1965 (2004).

[289] J. N. Winn, Y. Fink, S. Fan, and J. D. Joannopoulos. Omnidirectional reflection from a one-dimensional photonic crystal. *Opt. Lett.* **23**, 1573 (1998).

[290] T. Hattori, N. Tsurumachi, and H. Nakatsuka. Analysis of optical nonlinearity by defect states in one-dimensional photonic crystals. *J. Opt. Soc. Am. B* **14**, 348 (1997).

[291] B. Shi, Z. M. Jiang, X. F. Zhou, and X. Wang. A two-dimensional nonlinear photonic crystal for strong second harmonic generation. *J. Appl. Phys.* **91**, 6769 (2002).

[292] S. Y. Lin, G. Arjavalingam, and W. M. Robertson. Investigation of absolute photonic band-gaps in 2-dimensional dielectric structures. *J. Mod. Opt.* **41**, 385 (1994).

[293] W. M. Robertson, G. Arjavalingam, R. D. Meade, K. D. Brommer, A. M. Rappe, and J. D. Joannopoulos. Measurement of the photon dispersion relation in two-dimensional ordered dielectric arrays. *J. Opt. Soc. Am. B* **10**, 322 (1993).

[294] S. F. Mingaleev and Y. S. Kivshar. Effective equations for photonic-crystal wave-guides and circuits. *Opt. Lett.* **27**, 231 (2002).

[295] S. F. Mingaleev and K. Busch. Scattering matrix approach to large-scale photonic crystal circuits. *Opt. Lett.* **28**, 619 (2003).

[296] T. Hattori, N. Tsurumachi, S. Kawato, and H. Nakatsuka. Photonic dispersion relation in one-dimensional quasicrystal. *Phys. Rev. B* **50**, 4220 (1994).

[297] A. A. Asatryan, P. A. Robinson, L. C. Botten, R. C. McPhedran, N. A. Nicorovic, and C. M. de Sterke. Effects of disorder on wave propagation in two-dimensional photonic crystals. *Phys. Rev. E* **60**, 6118 (1999).

[298] C. Ang, A. S. Bhalla, and L. E. Cross. Dielectric behavior of paraelectric $KTaO_3$, $CaTiO_3$, and $(Ln_{1/2}Na_{1/2})TiO_3$ under a dc electric field. *Phys. Rev. B* **64**, 18 4104 (2001).

[299] A. Yariv. *Optical Electronics*. Saunders College Publishing, Fort Worth (1991).

[300] N. I. Santha, M. T. Sebastian, P. Mohanan, N. M. Alford, K. Sarma, R. C. Pullar, S. Kamba, A. Pashkin, P. Samukhina, and J. Petzelt. Effect of doping on the dielectric properties of cerium oxide in the microwave and far-infrared frequency range. *J. Am. Ceram. Soc.* **87**, 1233 (2004).

[301] J. Petzelt, T. Ostapchuk, S. Kamba, I. Rychetský, M. Savinov, A. Volkov, B. Gorshunov, A. Pronin, S. Hoffmann, R. Waser, and J. Lindner. High-frequency dielectric response of SrTiO$_3$ crystals, ceramics and thin films. *Ferroelectrics* **239**, 987 (2000).

[302] H.-M. Christen, J. Mannhart, E. J. Williams, and C. Gerber. Dielectric properties of sputtered SrTiO$_3$ films. *Phys. Rev. B* **49**, 12 095 (1994).

[303] A. K. Tagantsev, V. Sherman, K. F. Aatafiev, J. Venkatesh, and N. Setter. Ferroelectric materials for microwave tunable applications. *J. Electroceram.* **11**, 5 (2003).

[304] O. G. Vendik, L. T. Ter-Martirosyan, and S. P. Zubko. Microwave losses in incipient ferroelectrics as functions of the temperature and the biasing field. *J. Appl. Phys.* **84**, 993 (1998).

[305] J. Petzelt, T. Ostapchuk, I. Gregora, I. Rychetský, S. Hoffmann-Eifert, A. V. Pronin, Y. Yuzyuk, B. P. Gorshunov, S. Kamba, V. Bovtun, J. Pokorný, M. Savinov, V. Porokhonskyy, D. Rafaja, P. Vaněk, A. Almeida, M. R. Chaves, A. A. Volkov, M. Dressel, and R. Waser. Dielectric, infrared, and Raman response of undoped SrTiO$_3$ ceramics: Evidence of polar grain boundaries. *Phys. Rev. B* **64**, 18 4111 (2001).

[306] H. Němec, L. Duvillaret, F. Garet, P. Kužel, P. Xavier, J. Richard, and D. Rauly. Thermally tunable filter for terahertz range based on a one-dimensional photonic crystal with a defect. *J. Appl. Phys.* **91**, 4072 (2004).

[307] H. Němec, P. Kužel, L. Duvillaret, A. Pashkin, M. Dressel, and M. T. Sebastian. Highly tunable photonic crystal filter for the terahertz range. *Opt. Lett.* **30**, 549 (2005).

[308] H. Němec, F. Kadlec, P. Kužel, L. Duvillaret, and J.-L. Coutaz. Independent determination of the complex refractive index and wave impedance by time-domain terahertz spectroscopy (2006). Accepted in Opt. Commun.